Development of a Digital Twin for Demo Cooling System

Prepared by:

Amandla Mvimbi

Prepared for:

Primary Supervisor: Professor Edward Boje

Co-supervisor: Dr James Keaveney

31st January 2025

Submitted to the Department of Electrical Engineering at the University of Cape Town in partial fulfilment of the academic requirements for the degree of Master of Science in Electrical Engineering.

Plagiarism Declaration

I know the meaning of plagiarism and declare that all the work in the document, save for that which is properly acknowledged, is my own. This thesis/dissertation has been submitted to the Turnitin module (or equivalent similarity and originality checking software) and I confirm that my supervisor has seen my report and any concerns revealed by such have been resolved with my supervisor.

Name: Amandla Mvimbi

Signature: Signed by candidate

Terms of Reference

The deliverables of this undertaking include:

1. Develop a digital twin of Demo 2PACL Cooling system prototype
2. Use digital twin to conduct robust control system design
3. Dynamically test stepper logic with digital twin
4. Study the system dynamic behaviour

Acknowledgements

This dissertation and the journey it concludes could not have been possible without the generous support that I have so graciously received over the past two years. I would like to take a moment to express my sincere gratitude to those who helped make this journey a success.

I wish to begin by expressing my sincere gratitude to The Mastercard Foundation for generously supporting my studies at The University of Cape Town. The holistic support of the program has been an immense source of motivation throughout my journey. I would also like to thank The University of Cape Town Electrical Engineering Department for this wonderful opportunity.

To my primary supervisor – Professor Edward Boje, thank you for your wisdom and patience. Our weekly meetings, which you so kindly made yourself available for, were always insightful. The project could not have been possible without your guidance – which is full of incisiveness. I would also like to thank my co-supervisor – Dr James Keaveney, for facilitating the collaboration between CERN and UCT and for his continued support throughout my journey, which has been nothing short of invaluable. To my CERN supervisor, Dr Viren Bhanot, thank you for your mentorship and astute guidance, especially with simulations, and for meticulously proofreading this report so cheerfully. I have been challenged and have grown under your supervision, and I could not ask for better supervisors.

Upon my arrival at CERN, I was hosted by the Fluidic Systems (FS) Department. I want to thank all members of the department for the warm welcome and for supporting me in more ways than I could count. And for their meticulous work on the design, building and commissioning of the Demo, which was used to validate the simulations. In particular, I wish to express my gratitude to Lukasz Zwalinski and Paolo Petagna for their support, administratively and otherwise, and to Bart Verlaat for always availing himself to explain many non-trivial concepts so clearly and concisely, and for the support with the timber retrieval script for the bulk export of Demo data.

I also wish to thank the control team in the FS Department at CERN, specifically Loic Davoine and Dani Teixeira, for assisting with access to the Demo controls and monitoring, as well as support with all the Demo logic and controls-related issues. I also wish to thank Benjamin Bradu from the Cryogenics (CRG) Section and Brad Schofield from the Industrial Controls and Safety Systems Section (ICS) for their kind assistance and willingness to help. To my fellow students at UCT, thank you for all those virtual meetings, and to fellow students and peers at CERN, thank you for all the coffees, hikes, and adventures shared. In particular, thanks to Luca Contiero for all the insightful coffee break chats, Youri Penders for assistance with the bulk export of Demo data from Timber, and Yann Herpin for the support during the course of the project.

I would like to express my deepest gratitude to my family for their unwavering support throughout the years. To my mom and dad, thank you for all the sacrifices you made so gracefully. And to my sister and friend, Jay, I appreciate you for always being there for me through it all.

Abstract

CO_2 - based mechanically pumped fluid systems, known as Two-phase Accumulator Controlled Loop (2PACL) systems, have continued to enjoy extensive research and exploration at CERN. The system offers operational specifications that arise as a results of the High Luminosity upgrade. These include the need to operate at a colder temperature of -45˚C at the detector and -53˚C at the pump inlet and substantially higher varying loads. Furthermore, for redundancy, the systems now need to have multiple plants in parallel. To address challenges pertaining to scaling, the systems now have novel design elements such as the addition of the surface storage, flow-through mode for the accumulator, Back Pressure Regulator, new more intricate logic.

This project considers simulations that have been developed for mechanically pumped fluid systems and then develops a full-scale model for the novel 2PACL systems developed at CERN, including the new of intricate logic and functionality. The literature survey revealed that there are no simulations to conduct a system-level study or a study of this new logic. No simulations are available for the new systems with parallel architecture and new logic associated with it for smooth handover. The project further explores how the critical control loops in the new systems may benefit from a procedural control design that considers plant uncertainty and sampling effects.

Simulations conducted with the model are then validated against the measurements from corresponding experiments in Demo – CERN's 2PACL prototype, which cover startup, setpoint change, load change, and the swap and re-takeover test. The results are used to validate the model fidelity – both the discrete logic and trajectory behaviour.

Contents

List of Figures

List of Abbreviations

LHC – Large Hadron Collider

2PACL – Two-Phase Accumulator Controlled Loop

T2PACL –Traditional 2PACL

S2PACL – Surface 2PACL

S2PACL_StB - S2PACL Standby

ALICE – A Large Ion Collision Experiment

ATLAS – A Toroidal LHC Apparatus

CMS – Compact Muon Solenoid

VELO – Vertex Locator

CO_2 – Carbon Dioxide

HIL – Hardware-In-a-Loop

ITk – Inner Tracker

LHCb – Large Hadron Collider beauty

SRC – Split Range Controller

OPC UA – OPC Unified Architecture

Deck – OPC UA Deck

PROCOS – Process and Control Simulator

TL – Transfer Lines

dP – Pressure Drop

PLC – Programmable Logic Controller

REFPROP – Reference Fluid Thermodynamic and Transport Properties Database

BPR – Back Pressure Regulator

P&ID – Piping and Instrumentation Diagram

PID – Proportional, Integral and Derivative controllers

List of Symbols

Symbol	Description	Units
H	Enthalpy	[kJ]
P	Pressure	[bar]
U	Internal energy	[kJ]
V	Volume	[m^3]
Z	Atomic Number	[-]
dP	Differential Pressure	[bar]
m	Mass	[kg]
q	Energy input	[kW]
s	The complex Laplace variable which equals $\sigma + j\omega$	[rad/s]
u	Specific Internal energy	[kJ/kg]
w	The complex digital-domain variable which $\sigma + j\omega$	[rad/s]
x	Vapor Quality	[-]
α	The corner frequency	[rad/s]
β	Volume expansivity	[K^{-1}]
ρ	Density	[kg/m^3]
$\dot{m}_0$	Nominal Mass Flow rate	[kg/s]
$\dot{m}_{in}$	Mass Flow rate into a component	[kg/s]
$\dot{m}_{out}$	Mass Flow rate out of a component	[kg/s]
$\hat{h}$	Mass fraction weighted Specific Enthalpy	[kJ/kg]
h_{in}	Specific Enthalpy of mass flowing into a component	[kJ/kg]
h_l	Specific Enthalpy of liquid fraction	[kJ/kg]
h_{out}	Specific Enthalpy of mass flowing out of a component	[kJ/kg]
h_v	Specific Enthalpy of vapour fraction	[kJ/kg]
T_{CO2}	Accumulator Saturation Temperature	[˚C]
T_{R744}	R744 Chiller Temperature	[˚C]
T_d	Heat exchanger transport delay	[s]
X_0	Radiation Length	[g/cm^2]
c_{pl}	Isobaric Heat Capacity of liquid fraction	[K^{-1}]
v_l	Specific volume of liquid fraction	[m^3/kg]
v_v	Specific volume of vapour fraction	[m^3/kg]
β_l	Volume expansivity of liquid fraction	[K^{-1}]
β_v	Volume expansivity of vapour fraction	[K^{-1}]
h	Averaged Specific Enthalpy of component	[kJ/kg]

Keywords

1. Modelling
2. Simulation
3. Digital Twin
4. Two-phase
5. Robust Control
6. 2PACL
7. Subcooling
8. Stepper
9. Sensitivity
10. Complementary Sensitivity

1. Introduction

The universe is full of magical things patiently waiting for our wits to grow sharper.

– *Eden Phillpotts*

This dissertation describes the development of a digital twin for the state-of-the-art 2-Phase Accumulator Controlled Loop (2PACL) cooling systems, which regulate the temperature of silicon particle detectors during experiment runs at CERN. The project aimed to model Demo – CERN's 2PACL prototype for the next generation of detector – in EcosimPro; then, this virtual plant was used to test robust controller design, test dynamic stepper logic, and finally to study the system behaviour during steady state, setpoint changes, and load changes. System redundancy during plant failure was also studied. The development of the digital twin as a proof-of-concept for a 2PACL system is essential because:

- The new systems are complicated and need to be studied.
- Iteration of various controller schemes can be carried out.
- The simulation may eventually be used for operator training.
- The model can be used to test operation outside the nominal range.

The abovementioned benefits will allow the high luminosity experiment to run, yielding more events per unit time. This chapter will give a background to the research, outline its requirements and outcomes, and define this project's scope.

1.1 Background to the study

CERN

Founded in 1954, the European Organization for Nuclear Research (CERN) is the world's largest particle physics research facility of its kind. CERN's campus lies astride the French-Swiss border. Central to the organisation's research are its particle accelerators. These accelerate particles to 99.99999991% of the speed of light [1], which are then allowed to collide at predetermined collision points that coincide with the detectors. The particles break down further into constituents – which include fundamental particles such as quarks, leptons and bosons. These fly outwards from the collision point and permeate different detectors in the assembly. In this way, the outcome of this event is registered by the detectors[1]. Figure 1 below is the Large Hadron Collider (LHC) tunnel in which the particles are accelerated before colliding at the ATLAS, CMS, LHCb, and ALICE collision points.

[1] The word *detector* refers to both the entire assembly at the collision point, such as the ATLAS detector in Figure 2, and the individual layers within it, like the Inner Tracker and Muon Spectrometer. In this report, *detector* will be used interchangeably for both.

Figure 1: Large Hadron Collider Aerial (CERN) View[2]

Particle Accelerators

The 27-kilometer LHC tunnel houses a ring of superconducting magnets and two tubes along the tunnel's length, which are kept at ultrahigh vacuum. Two high-energy particle beams are made to travel at near the speed of light in opposite directions before being allowed to collide at the collision points. A strong magnetic field from the superconducting magnets guides and focuses the beams. For focusing, strong quadrupole magnets are used to focus the beam to increase the chance of collision. Collision of the beams happens exclusively at the collision points along the tunnel, namely – ATLAS, LHCb, CMS, and ALICE.

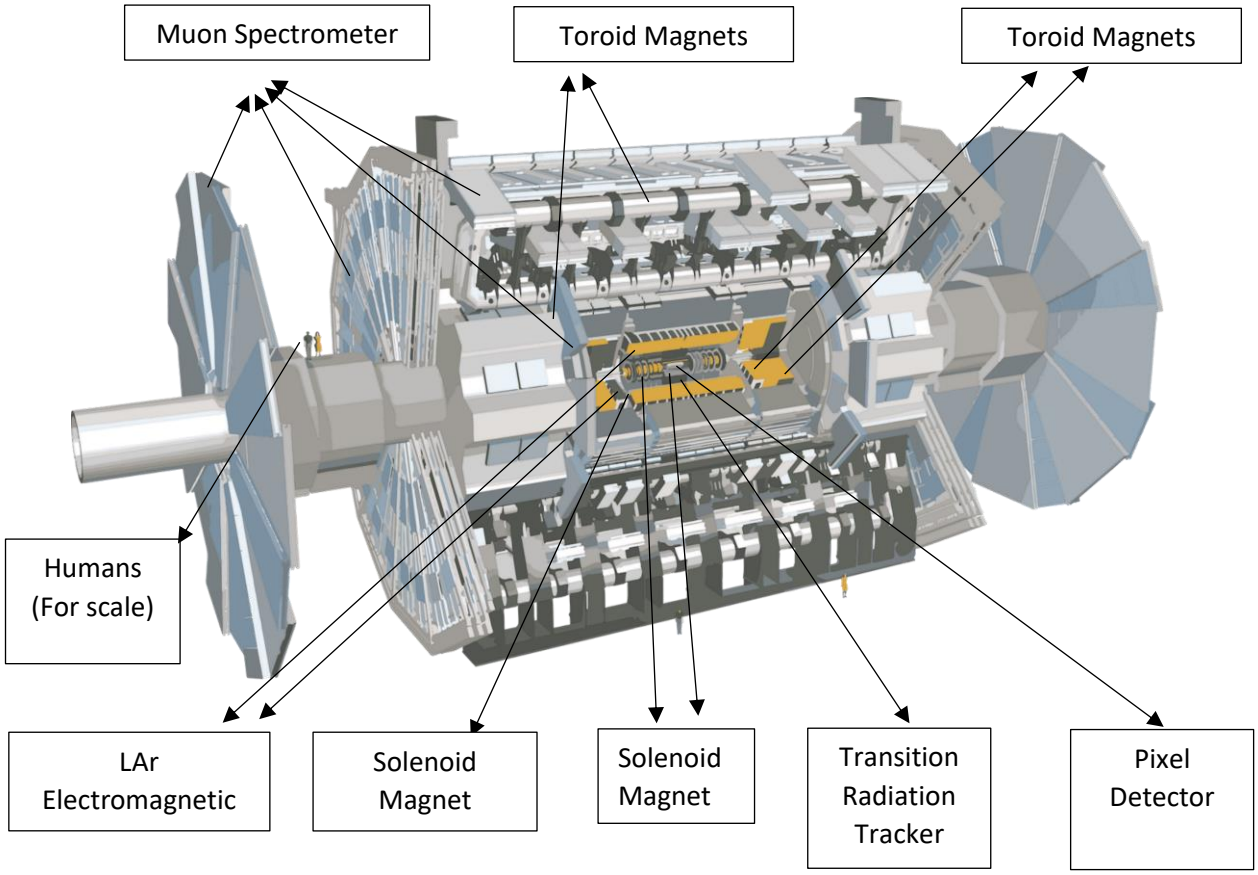

Figure 2: ATLAS Detector[3]

1.1.1 Detector Cooling

Detectors need to be cooled because they generated significant thermal energy – with a power output of 310kW from ATLAS and 550kW from CMS - during experiment runs, and this needs to be dissipated by means of an active cooling system, furthermore, keeping the detectors cold at subzero temperatures mitigates the negative effects of radiation on the detectors [4, 5]. Figure 3 illustrates how the pixel detectors are cooled, the electronics are mounted on the top plate of the support module shown below. Heat is then absorbed into the working fluid (CO_2) through the highly conductive composite foam and thermal paste and then into the evaporator tube.

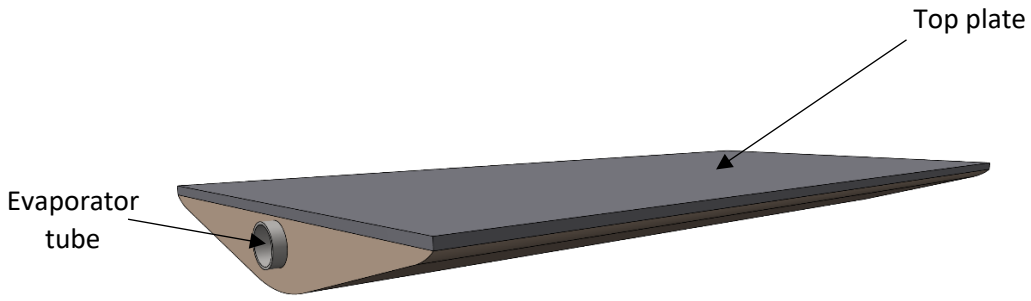

Figure 3: Pixel Detector [Designed with Shapr3D]

1.1.2 Benefits of Two-Phase Cooling

A two-phase fluid is one that exists as a mixture of two distinct phases – in the context of the project at hand, the mixture of interest will be the liquid-vapour mixture. In two-phase cooling, two-phase mixture of the refrigerant is used to cool the load. Two-phase fluids often assume different flow behaviour as the external and internal conditions are changed. Different regimes and the vapour qualities under which they typically occur are depicted by Figure 4 below. It shows that a complete liquid flow occurs at zero vapour quality. This is followed by a mixture of tiny vapour bubbles in a predominantly liquid fluid called bubbly flow. As more liquid evaporates and the vapour quality increases, the flow changes to plug flow – in this regime, large vapour bubbles flow enclosed by liquid around them. This is then followed by slug flow, where the bubbles are wide enough to touch the walls of the tube. As the quality increases further, wavy flow ensues, in which the liquid flows on one side of the tube with a thin film that intermittently dries up on the top surface of the tube. The penultimate regime is annular flow, where mist flow occurs in the centre and is surrounded by a thin liquid film. The final regime is dry-out, where most of the mixture has boiled into gas, and the remaining liquid flows entirely as a mist, and the walls are dry.

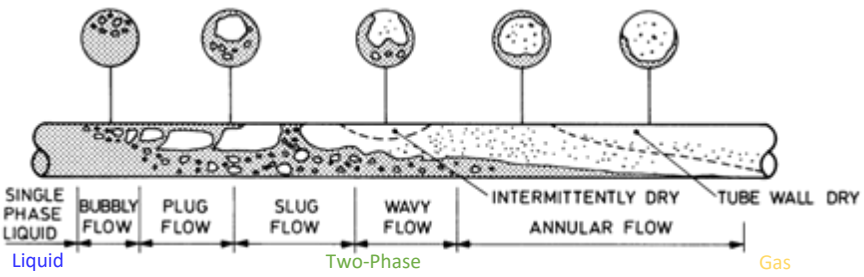

Figure 4: Flow Regimes[6]

It is worth noting that the regime in which flow exists depends on the vapour quality and the mass flux. Figure 5 is a map which gives a broad idea of the flow conditions under which various flow patterns are observed. Secondly, these boundaries are empirically defined and, therefore, shift with the refrigerant used, the flow channel orientation and internal surface roughness of the tube, pressure, and several other parameters [7]. This makes the prediction of the heat transfer coefficient especially challenging, as there is always an error margin [8-10].

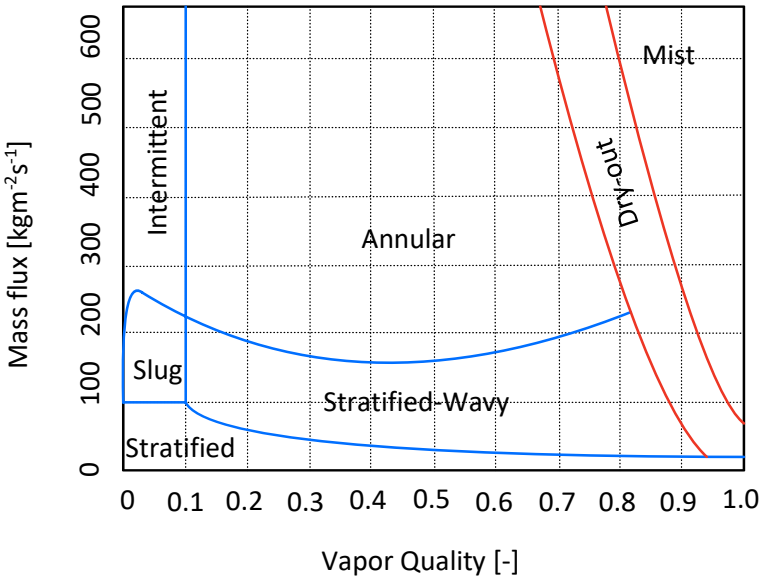

Figure 5: The Flow Regime Prediction Map[8-12]

The flow regime, nonetheless, remains vital because it has significant implications on the heat uptake in the detector and, therefore, the cooling efficiency of the 2PACL system. This is because the heat transfer coefficient (HTC) generally increases with vapour quality until approximately $x = 0.8$ when dry-out occurs [10, 11, 13]. The coefficient then falls abruptly to the much smaller value for single-phase gas. When dry-out occurs, the difference between the detector temperature and the temperature of CO_2 refrigerant flowing through the *evaporator tubes* increases such that the detector temperature no longer follows the setpoint as shown in Figure 6 – the return line saturation temperature. As a consequence, the temperature control is compromised and the detectors may crack if a thermal runaway ensues. The figure shows that a high temperature difference between the working fluid and the detector occurs at liquid flow ($x = 0$), which is undesirable. As the fluid enters as a saturated liquid (x > 0), this difference decreases due to increased heat transfer. However, if dry-out occurs, the temperature difference increases again. The target operation for the 2PACL is with vapor quality between 0 and 0.8 with sufficient margin to clear the dry-out region. In Demo, the target vapour quality is 0.33 which gives a good margin before dry-out.

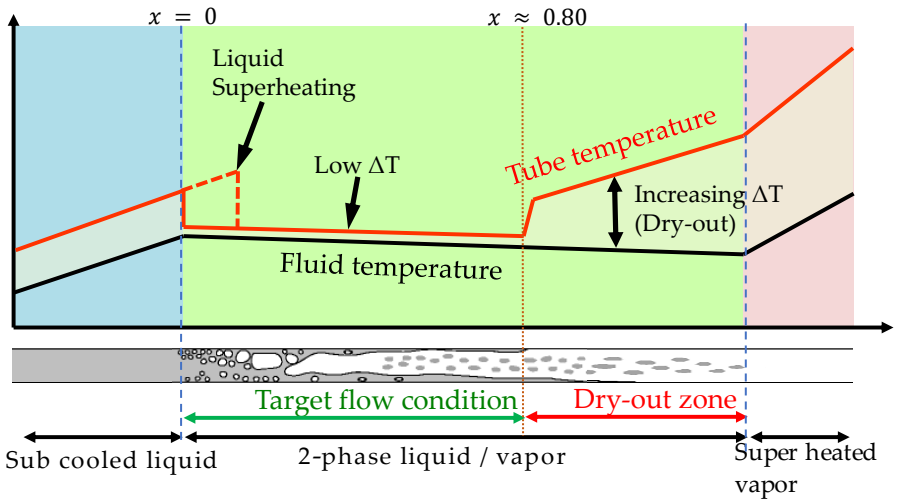

Figure 6: Flow regime and temperature control[14]

In summary, Figure 6 illustrates that two-phase cooling is preferable because of improved HTC and heat uptake, accurate, simplified temperature controllability and reduced thermal gradients. More importantly, the temperature of the detector can be controlled accurately over long distances over a wide range of loads.

1.1.3 CO_2 as a refrigerant

CO_2 has emerged as an apt refrigerant for detector cooling because it has high latent heat and low viscosity, shown in Figure 7, which enhance heat uptake and minimize pressure drops, allowing for smaller tubing. This reduces thermal inertia and improves the *material budget* in the detector assembly. Material budget speaks to minimising the amount of matter a particle interacts with as it travels from the collision point to the detector, it is often expressed in terms of *radiation length* (X_0), which is a measure of how far a particle can travel in the material before losing 37% of its energy (a factor of $1/e$) [15]. The loss of energy results from the emission of photons during the interaction with matter – a phenomenon known as *Bremsstrahlung radiation* [15]. The radiation length equation is as follows:

$$X_0 = \frac{\frac{716.4g}{cm^2}}{Z(Z+1)\ln\left(\frac{287}{Z}\right)} \quad (1)$$

Where Z is the material's atomic number.

For composite materials, the radiation length can be determined thus [15];

$$\frac{M_0}{X_0} = \sum \frac{M_i}{X_i} \quad (2)$$

Where M_i ,X_i ,M_0 and X_0 are the mass of individual components, and radiation lengths of individual components, the combined mass of the components and the combined radiation length, respectively. Equations 1 and 2 show that a reduction in the material in the detector is favourable because it means an increase in radiation length, which allows particles to reach detectors without significant energy losses as they interact with the material that supports and cools the detector assembly. This can be achieved by using less mass in the experiment section, which is why smaller tubes are advantageous [16, 17]. CO_2 also has a relatively low Global

Warming Potential (GWP), of several thousand times less than its chlorofluorocarbon (CFC) counterparts [18]. CERN's use of CO_2 aligns with the Kigali Amendment by reducing CFC usage.

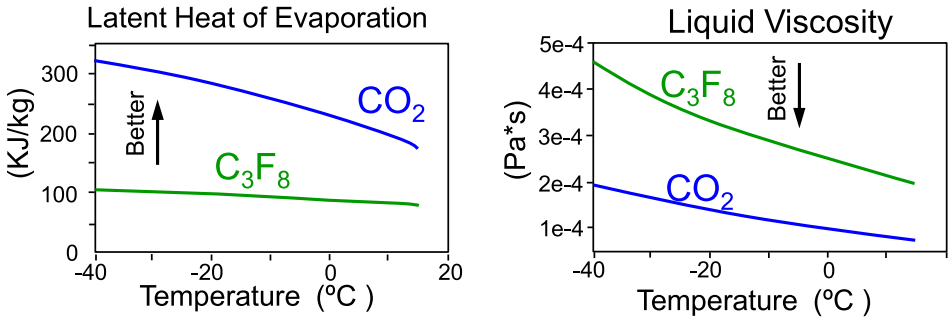

Figure 7: Latent heat of Evaporation and Liquid Viscosity of CO2 vs Temperature[19]

There are various ways to represent the conditions under which a substance changes through different states. The two common diagrams are the Pressure-Temperature (P-T) and the Pressure-Enthalpy(P-h) diagrams shown in Figure 8 and Figure 9 respectively.

The P-T Diagram

The P-T diagram for CO_2 is depicted in Figure 8 below. It shows the states in which CO_2 exists as the temperature and/or pressure changes, namely– solid, liquid, gas, and supercritical fluid (SCF). The interface between distinct colours marks the temperature-pressure pairs under which a change of phase occurs. On the other hand, the solid boundaries represent multi-phase states with a clearly visible separation between coexisting phases. The SCF is not considered a distinct phase as it shows no clear separation boundary from the other three phases. The dashed boundaries and a colour gradient are used in the diagram to represent this idea. Finally, aside from two-phase mixtures that exist along solid lines, there exists a triple point (-56.56˚C at 5.17 bar) where the three distinct phases of a substance – solid, liquid, and gas – coexist stably. This point lies at the intersection of the three solid boundaries. In the context of the 2PACL system, the diagram shows that the lower bound of the system pressure-temperature operational range is the triple-point of CO_2 because here, a mixture of dry-ice, liquid CO_2 and gaseous CO_2 will begin circulating in the system. This can cause pipe blockage which will lead to rapid overpressure. On the opposite end of the spectrum, at high pressure and temperature, the system is inherently bounded by the critical point (30.98˚C at 73.77 bar). In the SCF region, the coupling between the pressure and temperature is lost completely, and the 2PACL cooling system would fail.

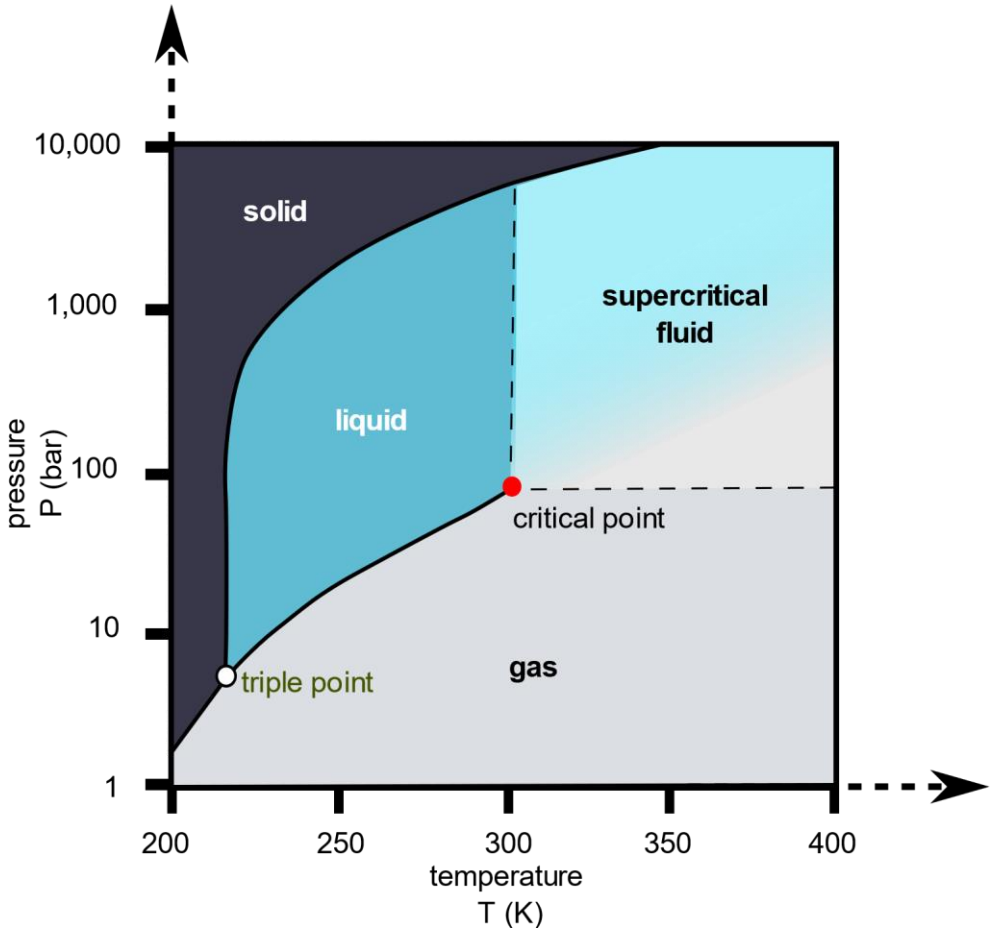

Figure 8: P-T diagram of CO_2.[20]

The P-h Diagram

An equally important diagram for visualising the operation of the system is the P-h diagram. This information-packed diagram is incredibly convenient because, given any pair of properties of a pure substance, such as pressure, temperature, specific enthalpy, vapour quality, density or entropy, the rest of the thermodynamic properties of the substance, including its phase, can be read off the plot shown by Figure 9. The diagram depicts a significant phenomenon central to the operation of the 2PACL system: that is, when in a two-phase state, the temperature and pressure of a substance, in this case, CO_2, are coupled so that changing one directly alters the other. This is demonstrated by the horizontal isotherms in the two-phase area, highlighting that an isenthalpic change parallel to the pressure axis cuts the isotherm lines perpendicularly. This behaviour is at the core of the 2PACL Systems because the detector temperature can be controlled using just the return line pressure.

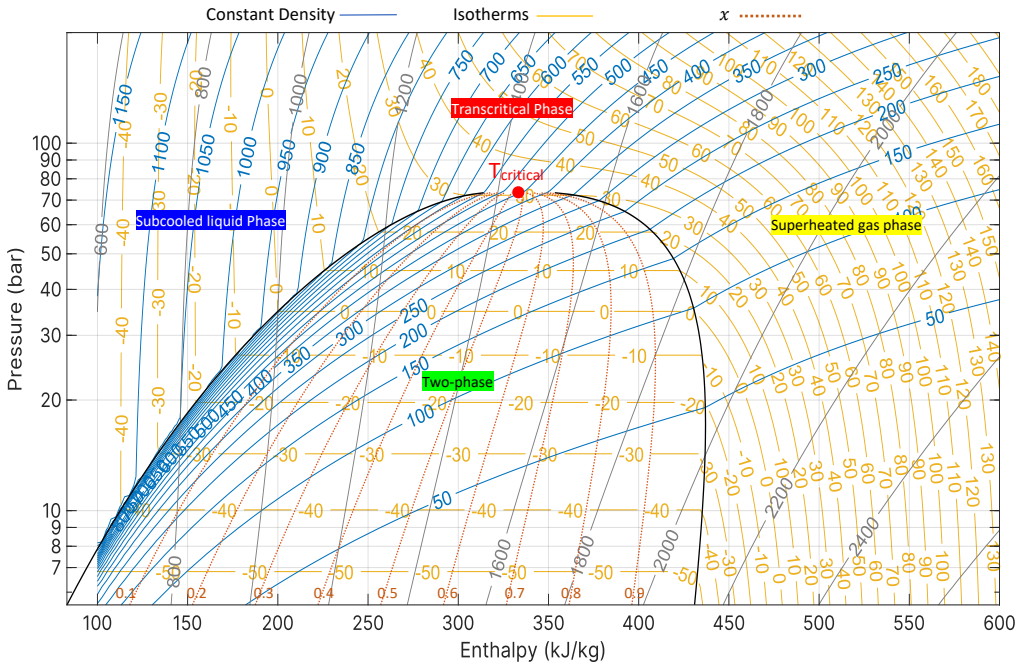

Figure 9: CO_2 P-h Diagram [Generated in MATLAB]

Jointly, the P-T and P-h diagrams provide valuable insight into the operation of the 2PACL systems. First, an arbitrarily large pressure setpoint cannot be requested because the system will enter the supercritical region where the pressure is no longer proportional to temperature. Likewise, the lower bound is the solid phase which is undesirable. Operating beyond either bounds would mean temperature control is compromised, and the detector temperature is in open-loop, which can enable a thermal runaway. The triple point and the dry ice region must be avoided, as the pump can only work with subcooled liquid CO_2. Hence, the operation is limited to the line segment between the triple and critical points in Figure 8.

1.1.4 The 2PACL Cooling System as a Solution

The 2PACL system consists of two loops as shown in Figure 10. The first loop, referred to as the *Primary*, is responsible for condensing and subcooling the returning CO_2 to ensure a supply of subcooled liquid CO_2 to the pump. This is crucial as the pump can pump liquid, and any bubble formation could lead to loss of flow because positive displacement pumps are meant to circulate near-incompressible fluids. Additionally, a stable mass flow rate for the detectors is critical and can only be achieved if the pump has a stable supply of liquid. The other loop, called the 2PACL loop, is the 2PACL circuit connected to an accumulator, which always contains a two-phase mixture of liquid and vapour CO_2. The accumulator features a heater and cooling coil to control system pressure through heating or cooling actions. Heating increases pressure by vaporizing CO_2 while cooling condenses vapour, decreasing pressure. This allows pressure control via a split-range controller, ensuring the accumulator pressure controls the detector exit temperatures since the piping and transfer lines are designed to have minimal pressure drop [21]. Overall, maintaining a two-phase mixture in both the detector and return

line is crucial for effective temperature control and enhanced heat transfer capacity within the system. In summary, the 2PACL uses two-phase cooling to cool the detectors, which enables the system to benefit from the advantages of two-phase cooling outlined in 1.1.2.

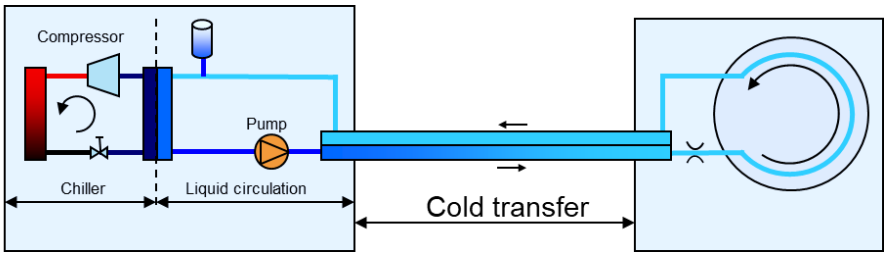

Figure 10: The loops of the 2PACL system[22]

1.2 History of 2PACL

From a mechanically pumped CO_2 loop system that was developed at the National Institute for Subatomic Physics (NIKHEF) to cool the AMS-02 -Tracker Control System (TTCS), the 2PACL system was born. This followed adaptations that had to be made to cool the LHCb-VELO detector and this 2PACL system was named the Velo Thermal Control System (VTCS) [21]. Because of the scale required, changes had to be made to the original system. These included the replacement of the cold radiator with a conventional refrigeration system; which would allow for accurate control over large distances (~50 m) without active components in the experimental carven where radiation is high [21]. This architecture separates active components, such as the chiller and accumulator pump heads, from passive components, like expansion capillaries and experiment-side tubing. In this way, active components can be housed in the radiation-shielded service cavern, which is accessible for human intervention. The passive components, on the other hand, which are less prone to failure on demand, are housed in the experimental cavern because they will need relatively lower intervention. Because of this, LHCb became the only detector without active components in the experimental cavern – in contrast to CMS and ATLAS which had moving parts in the radiation and magnetic field intensive area. Figure 13 shows how the first overhaul redesign of the first mechanically pumped CO2 loop system – which yielded the first 2PACL system, enabled the much-needed ability to separate the active and passive components.

Historically, two types of accumulators have been explored for pressure control; Pressure-Controlled Accumulator (PCA) and Heater-Controlled Accumulator shown in Figure 11 [23, 24]. The PCA adjusts system pressure by inflating or deflating a bellow using an external pressure source. This effectively alters the available volume in the system, thereby increasing or decreasing the pressure. In contrast, the heater-based accumulator controls pressure by heating or cooling the two-phase mixture, which evaporates or condenses the refrigerant to adjust the pressure. While the bellow accumulator responds faster, the heater-based accumulator is preferred due to its robustness and low maintenance because it has no moving parts.

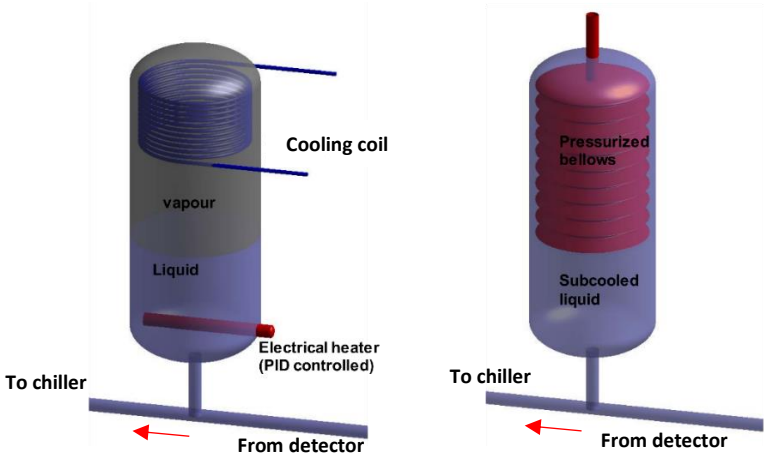

Figure 11: Heater Accumulator (Left), Bellow Accumulator (Right)[23, 24]

1.2.1 Phase-2 Upgrade of the Large Hadron Collider

CERN is upgrading its two biggest detectors – ATLAS and CMS – which form part of the Large Hadron Collider (LHC). This upgrade is for the High Luminosity Program that is set to commence in 2026 [12, 25, 26] and will substantially increase the radiation in the beam chamber [27]. Radiation degrades the delicate detector hardware. Furthermore, the Inner Tracker (ITk) will be replaced with the new state-of-the-art Pixel Detectors [28]. These new silicon electronics will have a higher thermal power output during experiment runs, creating noise in high-precision particle physics experiments and pose a risk of a thermal runaway for silicon electronics. Additionally, the detectors are designed to be kept at subzero temperatures during both operation and maintenance. During operation, this minimises leakage current, which varies exponentially with temperature. On the other hand, keeping the temperature of detectors low during maintenance prevents *reverse annealin*g of the silicon electronics – which is when defects in the lattice structure caused by radiation propagate [29].

1.2.2 Silicon Tracking Detectors

As part of the high luminosity upgrade, CERN is installing next generation state-of-the-art solid state silicon detectors in CMS and ATLAS. These detectors will be subjected to significantly high radiation of fluences reaching $2 \times 10^{16} n_{eq}/cm^2$ in the innermost pixel layers. The new detectors offer improved radiation hardness and improved precision and speed with better time resolution [30]. With this upgrade comes a set of new challenges, which include that the detectors must be operated at colder temperatures (-53°C at the pump inlet and -45°C at the detector outlet) while handling higher, varying thermal loads [16]. Additionally, because thermal gradients subject delicate silicon electronics to thermal stresses, which can cause cracking [12], the temperature of the detectors must be controlled accurately. The cooling system to be installed as part of the upgrade must use a refrigerant that is radiation hard to meet these requirements while considering the engineering and environmental constraints, including maintaining a low *material budget*, ensuring high redundancy, upholding operational stability,

and being eco-friendly. The abovementioned challenges have made the research and development to improve the existing 2PACL scheme crucial for CERN, and a model is needed to study these new systems.

1.2.3 Digital Twins

A digital twin is a *model* that accurately captures a physical system's dynamics or process. By using real-world data and *simulation*, digital twins can provide insights into the performance, operation and possible failure modes of the real system. A model is the product of the process of extracting knowledge from a physical system, organising this knowledge and representing it unambiguously – often referred to as modelling [31]. In this case, the unambiguous representation will be using a mathematical model. A simulation refers to performing experiments on the model to gain insight into and make predictions on how the actual system would behave if the same experiment were done on it [31]. The fidelity of a model dwells in how well it captures the discrete and continuous time behaviour of the real system – known as discrete events and trajectory behaviour, respectively. An example of the discrete behaviour is how an ON/OFF valve behaves during run time, while trajectory behaviour can be how pressures evolve over time.

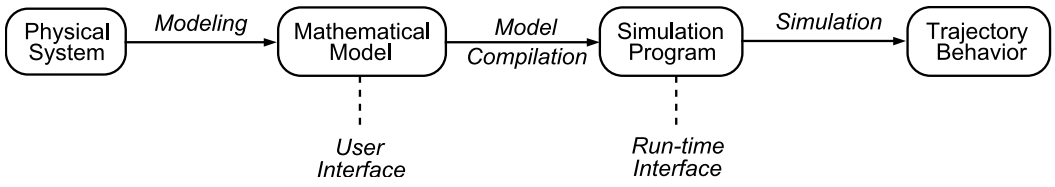

Figure 12: Digital-twin development pipeline[31]

1.3 Objective

1.3.1 Problem Statement

CERN has developed new cooling systems to address the new challenges arising from the high luminosity upgrade in 1.2.1 and 1.2.2. These state-of-the-art systems are much more complicated than any of the past variants of the 2PACL and are driven by much more elaborate PLC logic. There are no simulations in literature that conduct a system-level study including the study of this new logic. Furthermore, all the novel design features described later in 3.2 have never been simulated and studied. The new 2PACL system now includes multiple plants running in parallel with the need for smooth hand-over from one plant to the other, resulting in a need for a redesigned architecture and refined logic. These new systems feature critical control loops that need to be analysed and compensated procedurally.

1.3.2 Aim of Study

This project endeavoured to examine the literature on the evolution of detector cooling technologies at CERN as well as simulations for Mechanically Pumped Fluid Loop cooling systems thoroughly and then develop a digital twin of the state-of-the-art Demo 2PACL prototype using EcosimPro software. Next, a robust control design will be conducted using the full-scale model. This design includes drawing performance specifications, model design, and testing. Once robust controllers had been designed, a dynamic stepper logic validation will be carried out. Finally, the virtual plant will be used to gain insight into how the system behaves during steady-state operation, setpoint changes, load changes, and backup plant takeover in case of failure, and the simulation data was validated against Demo measurements. In other words, the outcome of this project is to develop and validate a proof-of-concept digital twin of Demo.

The outcomes of this research are as follows;

1. A high-fidelity EcosimPro model of the Main Plant, the Backup Plant, the transfer lines, and a dummy load was developed.
2. Performance specifications and design a robust control scheme that controls the detector temperature over the entire operation range were drawn up.
3. The stepper logic for the Main Plant, the Backup Plant, and the Accumulator were validated under dynamic conditions.
4. The digital twin was used to study system behaviour for steady state, setpoint changes, load changes, and backup functionality

1.4 Scope & Limitations

This project's scope centred on developing the digital twin for CERN's Demo 2PACL cooling system prototype using EcosimPro. The robust control design and characterisation were conducted with MATLAB. The models developed in the process are attached in the appendices A1 through A3. As for the project limitations, the project does not dwell on the component modelling as these have been documented very well during development by CERN and Empresario Agrupados Internacional S.A [32, 33]. Instead, the fundamental governing equations that form the foundation for all components are briefly discussed. Then, emphasis is placed on modelling the system. Due to time and computational limitations, only the 2PACL loop was modelled fully, while only part of the chiller close to the interface with the pump heads was modelled. The behaviour upstream of this has been imposed as boundary conditions consistent with the operation mechanism of the multistage compression cycle – which is the operation mechanism of the primary. This decision reduced model complexity as the chiller side circulates a mixture of oil and R744, which would have been more complicated to model. However, the loop of interest in this case is the 2PACL loop, as vapour compression cycles have been well studied and documented [34, 35]. Hence, this does not compromise any of the deliverables.

1.5 Plan of Development

Chapter 2, the genesis of this dissertation, explores the literature on the thermodynamics of the two-phase state and expounds on the flow behaviour of fluids in different states and external parameters. It then links these to the operation of 2PACL cooling systems. Next, the candidacy of CO_2 as the emerging refrigerant of choice is briefly unpacked. The 2PACL system in the context of detector cooling systems is discussed, including its operation mechanism and evolution. Then, the high luminosity upgrade and the challenges that come with it are discussed. Chapter 3 then proceeds to provides a detailed exhibition of Demo 2PACL cooling prototype at CERN, for which a full-scale model was developed. This chapter then ends by highlighting the gap in the literature that this work aims to bridge. Chapter 4 commences by giving a detailed description of the modelling philosophy employed to streamline the development. This chapter briefly discusses the fundamental relationships that describe how mass and energy are conserved. This is followed by the description of the EcosimPro Demo library created for the model and its dependencies, which pave the way for system modelling. Here, the system non-linearities and the robust control theory design techniques used to mitigate them are discussed. Lastly, the model solver is discussed, including some strategies for improving modelling and simulation speed. Using the temperature control loop – (accumulator and BPR), this chapter then demonstrates how the system can benefit from robust control design in Chapter 5. Next, data acquisition and post-processing are discussed and results are presented and analysed in Chapter 6, then conclusions are drawn and recommendations for future exploration are made in Chapter 7.

2.Literature Review

"We are made of star-stuff. We are a way for the universe to know itself."
— *Carl Sagan*

When it comes to the domains of thermodynamics, fluid dynamics and the architecture and operation mechanism of the 2PACL system, the existing literature in this context largely assumes a mechanical engineering background when discussing various principles. This presented a unique challenge because these had to be well understood and recontextualised within the framework of electrical engineering – specifically control systems and instrumentation. This effort to employ an interdisciplinary approach is necessary to bridge the gap between the two disciplines and holistically treat the problem.

2.1 Traditional 2PACL Systems

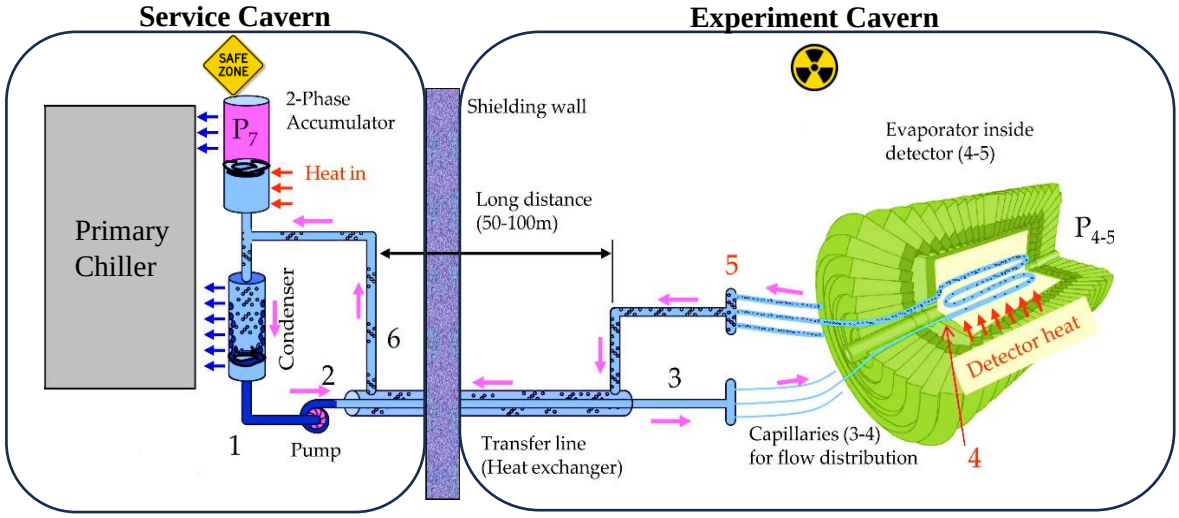

Figure 13: Service and Experimental Caverns[36]

The operation of the traditional 2PACL introduced in 1.1.4 is described with the aid of Figure 13 and the operation P-h diagram of the 2PACL at -30˚C in Figure 14 below. The CO_2 starts in **state point 1**, where it has been subcooled by the primary chiller. The subcooled liquid is pumped by a membrane positive-displacement pump, which pressurises the liquid CO_2 to **state point 2**. The CO_2 then enters the coaxial heat exchanger, which also serves as a transfer line where it absorbs thermal energy from the warmer return two-phase mixture. This results in the enthalpy gain, which takes it to **state point 3**. This exchanger exploits the vast surface area in the transfer lines for additional heat exchange and fundamentally reduces the loading on the external heat exchanger and the accumulator. Furthermore, this exchange of energy guarantees that the CO_2 becomes saturated when it expands as it goes through the capillaries. The expansion, which is almost fully isenthalpic, takes the CO_2 to **state point 4**. This saturated

liquid starts boiling once it enters the detector cooling channels in **state point 4** and gains substantial enthalpy, which moves the operation to **state point 5** at the detector exit. The boiling two-phase mixture exits the detector and loses some enthalpy to the cold saturated liquid from the pump in the coaxial heat exchanger, which gets it to **state point 6**. It goes back through the accumulator in **state point 7** to the external heat exchanger, where it is condensed and subcooled back to **state point 1**. It is finally sent back to the pump inlet. This cycle repeats throughout the operation.

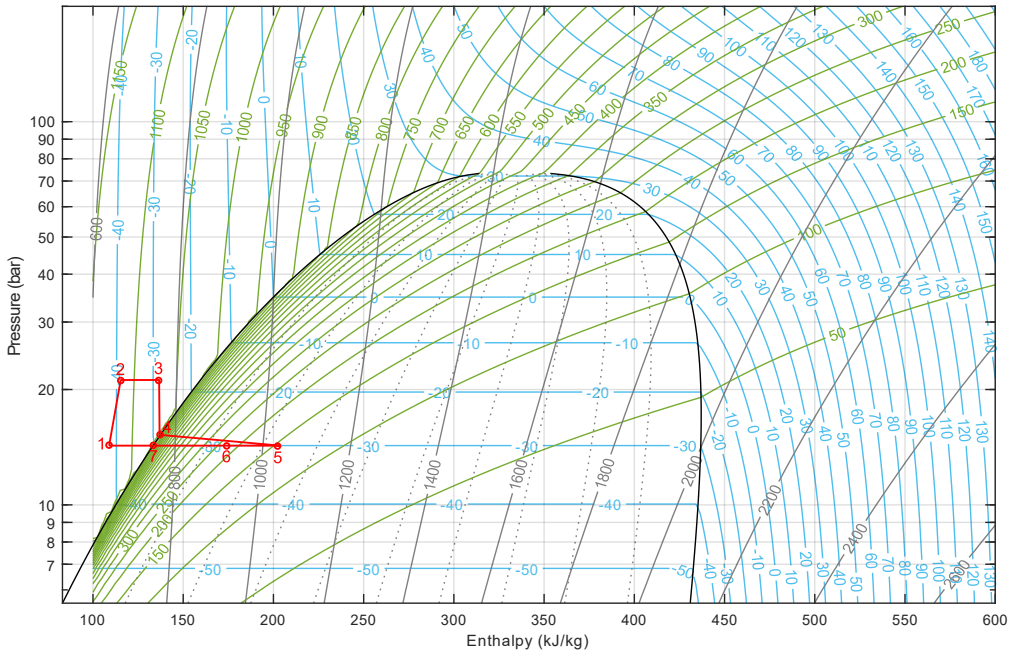

Figure 14: Traditional 2PACL Operation P-h Plot [Generated in MATLAB]

In summary, 2PACL system offer the following benefits:

- Improved heat transfer capabilities [6, 28, 36].
- Improved Material budget [6, 28, 36].
- Increased thermal stability, is radiation hard and non-magnetic [28].
- No need for localised control and controllability over large distances [6, 28].

2.2 Modelling and Simulation of MPFLs

The dynamic modelling of transients of MPFLs is still under-explored. Van Gerner and Braaksma carried out early work on the topic for a small-scale MPFL experimental set-up and conducted load changes (up to 331W) to study the mass flow transient in and out of the accumulator. The simulations which implemented the MacCormack predictor-corrector scheme for enthalpy were conducted in MATLAB, and there was an agreement between the simulation and the experimental measurements [37].

Building on the work of Van Gerner for a master's thesis, Bolder's work places emphasis on improving the mean absolute error (MAE) of the results from the model while also exploring the performance of different correlation from pressure drop, heat transfer and void fraction. Although the model encountered errors during reverse flow simulation, this study provided valuable insights by comparing various correlations with measurement data [24].

Bhanot uses EcosimPro instead for a transient simulation of CO_2 Research Apparatus (CORA), a medium-scale MPFL at CERN. His work uses the *upwind scheme* and can handle reverse flow, flow splitting and merging. In addition, the model implements the *staggered grid* where pressure and enthalpy are calculated in the volume cell, and the mass flow rate is calculated in a flow cell. The volume and flow cells are offset by half a cell width. The staggered grid effectively decouples the momentum equation from the energy and mass balance equations and improves the solver speed. The study placed emphasis on the system startup, load changes and setpoint changes. There was agreement between the simulation and experimental measurement [38, 39]

2.3 Digital Twins

A lot of research has gone onto the development of digital twins of various systems. One of the early works outside the scope of the Fluidic Systems Section on digital twins in EcosimPro is by Bradu [40, 41]. Bradu's comprises a digital twin for the cryogenic plants in the cryogenic department (TE-CRG) at CERN, which has been used for optimisation and more while saving energy. The model was represented by Differential Algebraic Equations in EcosimPro. CRYOLIB and PLC libraries, which now form dependencies of the DEMO library, were developed to facilitate the building of this model – elaborated later in 4.1. By comparing measurements with simulation data, Bradu found that the model captures the dynamic behaviour of the cryogenic plants well enough to gain insight into the systems. Since then, in the cryogenic department at CERN (TE-CRG). The model fidelity has continuously been improved and is now being used in a virtual commissioning setup – where a simulation is connected to real control hardware. This is used for operator training, failure scenarios simulations, operator reaction assessments and more [42].

In the Beams department at CERN, Schofield from the Industrial Communications and Safety Systems Section (ICS) developed a simulation of waste heat recovery and Heating, Ventilation, Air Condition systems in EcosimPro which are used to commission the control hardware [43, 44]. By using a virtual commissioning setup in [44], Schofield et al. were able to test the control implemented in a PLC without causing disturbances to the real systems, in effect maximising the availability. In the case of the digital twin for the waste heat recovery system, the virtual plant was used to gain insight into optimisation of energy usage. The results suggested that by use of the advanced non-linear MPC scheme studied, up to 20% energy saving could be achieved compared to conventional heuristic solutions.

The domain of digital twins, however, reaches far and wide and finds application in a broad spectrum of fields beyond CERN. An EcosimPro-based digital twin for the beet pulp dyer

simulator developed by Merino et. al [45]. The simulator was built with the purpose of creating an operator training platform. Data from the simulator yielded results that were consistent with the imposed boundary conditions based on the understanding of the process. Li et al. model a battery management system to estimate the state of the batteries and for fault diagnosis[46]. This machine learning based Back Propagation Neural Networks (BPNN) and Whale Optimisation Algorithm (WOA) accurately predicted and diagnosed faults with a success rate of over 95% [46]. In the domain of nuclear fusion energy research, Kwong et al. developed a digital twin for the Tokamak Fusion Reactor. The virtual platform comprises a Virtual Tokamak Control Centre (VCC) user interface through which the use may interact with the CAD model and complex fusion plasma simulations [47]. Complex simulations such as the Monte Carlo particle simulation of the Neutral Beam Injection (NBI) are simulated.

2.4 Motivation

The 2PACL cooling systems have enjoyed a lot of research, which has yielded advancements in the state-of-the-art. However, along with the much-desired 10-factor improvement in luminosity, the LHC upgrade brings about several new engineering challenges that must be addressed. Chief among these is the substantial increase in radiation and thermal load due to the increased luminosity and new silicon electronics, respectively. The implications are that the cooling system should be able to handle highly varying loads and operate at colder temperatures of -53˚C at the pump inlet and -45˚C at the detector to minimise radiation damage to the components and noise. Secondly, the system should exhibit a wide control range for the detector temperature of -45˚C to 15˚C degrees. Additionally, the system needs increased heat uptake, which increased mass flow rates can achieve; however, this would come at the cost of increased pressure drops.

The new system now has design changes, which include the addition of surface storage, flow-through mode and BPR operation, which need to be simulated and studied. Bhanot's work comprehensively covers the simulation of the startup, load changes and setpoint changes for CORA. However, there is a need for simulations for the startup of Demo because of its much larger scale, more intricate logic and the other design and operational novelties incorporated to address the challenges brought about by the High Luminosity upgrade - see 3.2 below. Furthermore, the new operation, which has several plants in parallel, needs to be further studied. The system's structured plant uncertainty and nonlinearities demand careful controller design, and a study on this was conducted, highlighting the need for sensitivity and robust stability analyses, which are underrepresented in the literature. Above all, there is need for validation of the model for this complex new design. This project aimed to develop a digital twin of Demo, use this virtual plant to conduct robust controller design and conduct system-level studies. Simulations in this regard were pivotal as none existed for these new systems, which will derive benefits similar to those accrued in other fields and industries highlighted above, such as modelling complicated dynamics without need for expensive, energy consuming hardware.

3.The Test Facility

The mind is not a vessel to be filled, but a fire to be kindled.

— *Plutarch*

3.1 Overview

Demo is the full-scale prototype built at CERN to explore the design, construction and operation of the final 2PACL systems, which, similar to Demo, will operate in the manner described in 3.3 below [16].The prototype comprises an R-744 primary chiller. The primary chiller is a multi-stage vapour compression cycle system that circulates a mixture of oil and CO_2. Demo was built with a target load capacity of 100 kW; however, the system is capable of rejecting 80 kW of thermal load at a setpoint of -45 ˚C due to undersized chiller. The main plant with three LEWA LGD3 positive displacement membrane pump heads, each fitted with a 6 kW motor. With these pumps, Demo can deliver a nominal flow of 1.5 kg/s on demand. The next main component in Demo is the 456 litres accumulator – which is approximately 60% of the entire system volume. 148-litre transfer lines connect the plant to the dummy loads, which emulate the detector load. Approximately 40 litres of this volume is the return while the rest the feed. The final two main components are the surface storage simulator and a backup plant with a single LEWA pump head for testing redundancy, also shown in Figure 15 below.

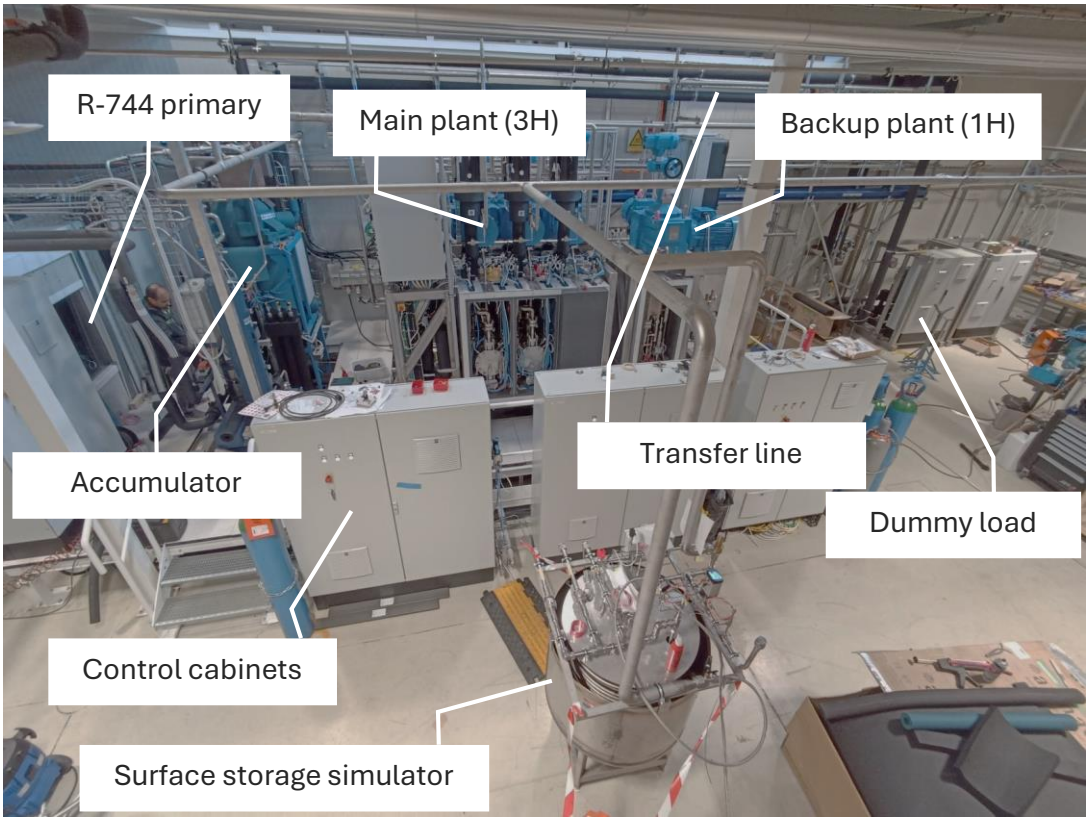

Figure 15: Demo Prototype overview[14, 32, 48]

3.2 System Novelties

Since its conception at NIKHEF and adaptation into the traditional 2PACL system described in 2.1 for Velo, CERN has actively developed the 2PACL system to meet its unique yet tight engineering constraints and scale. Chief among the novelties explored with this system is the addition of surface storage. The second is the Flowthrough Mode for the accumulator, which is activated by a three-way valve (k). Both new design improvements are depicted in Figure 16 below. The surface storage is necessitated by the high mass flux surge that happens when the detector load increases [32]. The surge happens because of the sudden expansion of the CO_2 in the detector; the vapour front pushes the liquid downstream, which rushes into the accumulator because the pump imposes a fixed mass flow rate. Preliminary investigations show that there is not a big enough accumulator to handle these surges under certain circumstances, such as during power-on – hence, excess CO_2 needs to be pumped up to surface storage. Alternatively, pre-evaporation is done using a warm nose, which is outside the scope of this dissertation. In this way, this mitigates the space constraint in the cavern. Furthermore, this is also to align with regulations on the quantity of CO_2 that can be stored underground and also helps solve the issue of inadequate space for large accumulators underground.

Flowthrough mode, on the other hand, improves the control of the pump inlet subcooling because, in this mode, the returning CO_2 two-phase mixture from the detector flows via the

accumulator to the external heat exchanger for subcooling. In this mode, the accumulator serves as a phase separator so that only saturated liquid goes to the external heat exchangers at the pump inlet. In this case, the work of this heat exchanger is exclusively to subcool the pump inlet since condensing has been done in the accumulator. This substantially increases the controllability of the subcooling because the changes in the phases at the interface of the heat exchangers make it non-linear and difficult to control with linear controllers such as PID controllers. Furthermore, the exchanger flooding level also exacerbates the non-linearities. The redesign of the 2PACL systems at CERN has also added Back Pressure Regulation (BPR) operation – which will be discussed later – not present in previous MPFLs. Finally, the new 2PACL system will run as multiple plants in parallel for redundancy, with multiple plants connected to the common load and new logic to facilitate which plant takes over the load.

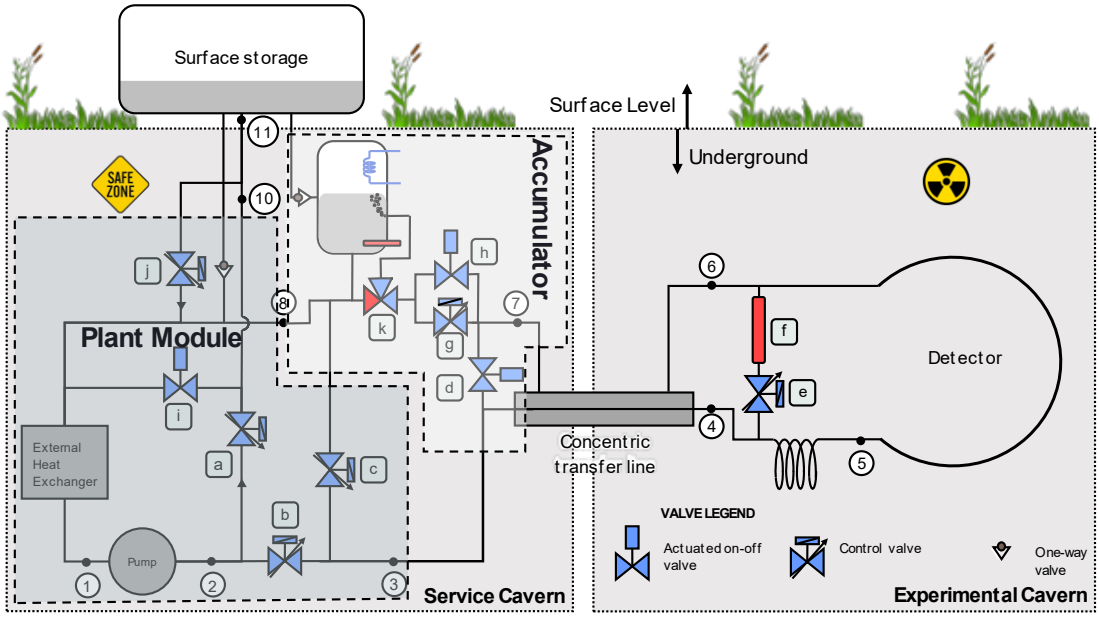

Figure 16: Simplified New 2PACL Schematic [32, 48]

3.3 New Operation Mechanism

Demo implements the new Surface-2PACL (S2PACL) operation mechanism, which is fundamentally similar to the traditional 2PACL operation, with the exception that the pump discharge is kept above the surface storage pressure because the system is now connected to the surface storage for accumulator emptying and filling functionality explained further in this subtopic. The primary chiller loop removes thermal energy from the system, while the 2PACL circuit is the link between the primary chiller and the load via the *condenser*.[2] In a steady state, the energy removed by the chiller is equal to the energy added by the detector load and the accumulator cooling or heating action. The operation of the 2PACL is described with the aid of the operation P-h diagram of the S2PACL at -30˚C in Figure 17. The CO_2 starts in **state**

[2] Condenser refers to the external heat exchanger which subcool the pump inlet. When the system is not in flow-through mode, it also condenses the returning CO2 before subcooling, otherwise its job is exclusively subcooling the pump inlet.

point 1, where the primary chiller has subcooled it. The subcooled liquid is pumped by a membrane positive-displacement pump, which pressurises the liquid CO_2. The discharge pressure control valve (b) in Figure 16 regulates the pump discharge pressure to a set value above the surface storage (5 bar in this case), which gets the system to **state point 2**.

The pressure drop across this valve takes the system to **state point 3**. From there, the refrigerant enters the coaxial heat exchanger, which also serves as a transfer line where it absorbs thermal energy from the warmer return two-phase mixture. This results in the enthalpy gain, which takes it to **state point 4**. Similar to the traditional systems, the coaxial exchanger uses the vast surface area in the long transfer line for improved heat exchange and fundamentally reduces the loading on the external heat exchanger and the accumulator. Furthermore, this exchange of energy guarantees that the CO_2 becomes saturated when it expands as it goes through the capillaries. The expansion, which is almost fully isenthalpic, takes the CO_2 to **state point 4**. This saturated liquid starts boiling once it enters the detector cooling channels in **state point 5** and gains substantial enthalpy, which moves the operation to **state point 6** at the detector exit. The boiling two-phase mixture exits the detector and loses some enthalpy to the cold saturated liquid from the pump in the coaxial heat exchanger, which gets it to **state point 7**. It goes back through the accumulator in **state point 8** to the external heat exchanger, where it is condensed and subcooled back to **state point 1**. It is finally sent back to the pump inlet. This cycle repeats throughout the operation.

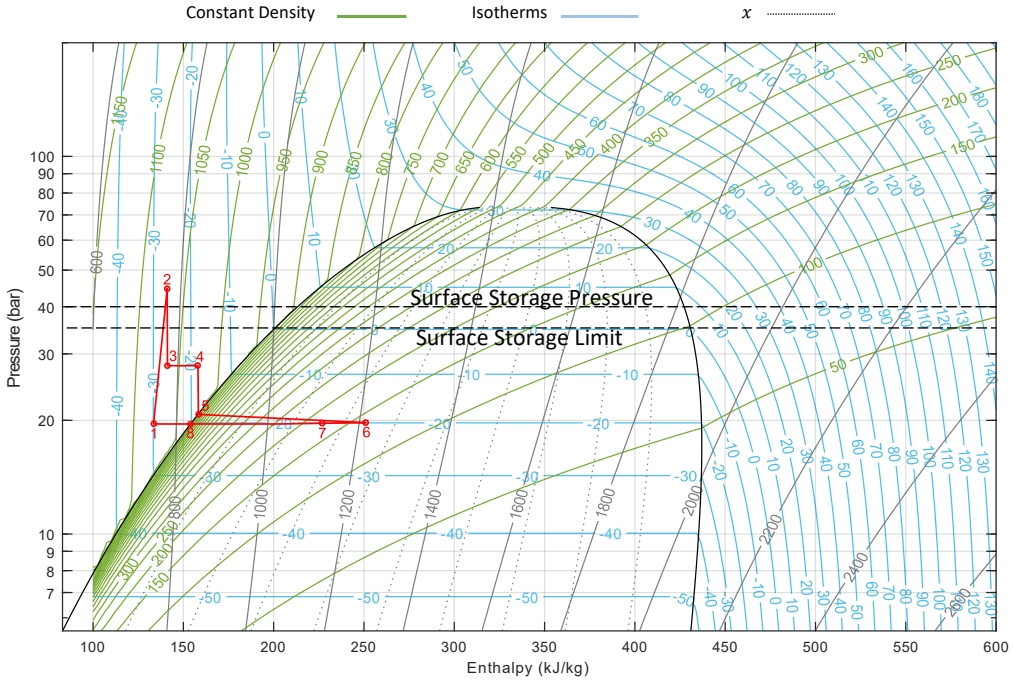

Figure 17: S2PACL Operation P-h Plot [Generated in MATLAB]

Figure 17 also illustrates the importance of keeping the accumulator, transfer line and detector at least saturated or two-phase. The change of phase is isothermal at a given pressure, and this ensures that the accumulator and return line saturation temperature approximate and control the detector temperature. If any of the points were to exit the dome, the isotherms would no

longer be horizontal, which suggests that temperature is no longer proportional to pressure. This would compromise the accurate temperature control offered by the 2PACL.

3.4 Operation Modes

Plant Operation Modes

Each plant has three distinct modes of operation, the first of which is the traditional 2PACL mode. In this mode, the system has no access to the surface storage and operates solely by the accumulator. The final systems are not designed to operate in T2PACL mode for prolonged periods; however, the systems need to be capable of operating in this mode in case of failure related to surface storage. The second mode is S2PACL mode, where surface storage is available to the system. It is in this mode that the accumulator can be emptied to surface storage through valve (a) using the 5 bar differential pressure held by valve (b) in Figure 16, when the level exceeds a preset threshold. Conversely, if the accumulator liquid level is too low, the system can be charged with CO_2 through valve (j) also shown in Figure 16. Filling the accumulator capitalises on the fact that the surface storage is always at a pressure higher than the accumulator and also benefits from the static head in the final systems. This mode also allows for surges in mass flow during load changes to be vented up to surface storage. The final operation mode is the S2PACL_StB. In principle, this mode is identical to the S2PACL mode, with the exception that the plant runs as a backup on standby, waiting to swap out a failing plant.

3.5 Process Control Object (PCO)

The system is driven by two redundant PLCs running several PCOs. PCOs are part of the control objects which give commands to their dependent field or PCO objects. In Figure 18 below, the CO_2 PCO handles all the alarms and interlocks. It monitors and may send orders to all its dependent PCOs and filed objects. The figure also shows some of the tags for field objects controlled by various PCOs, and further each PCO has a scope of field objects which it controls. A case in point is that the PCO P1, the main plant PCO, controls its dependent field objects, such as pump frequency (LP1002) and control valves, such as the differential pressure control valve (CV1a16).

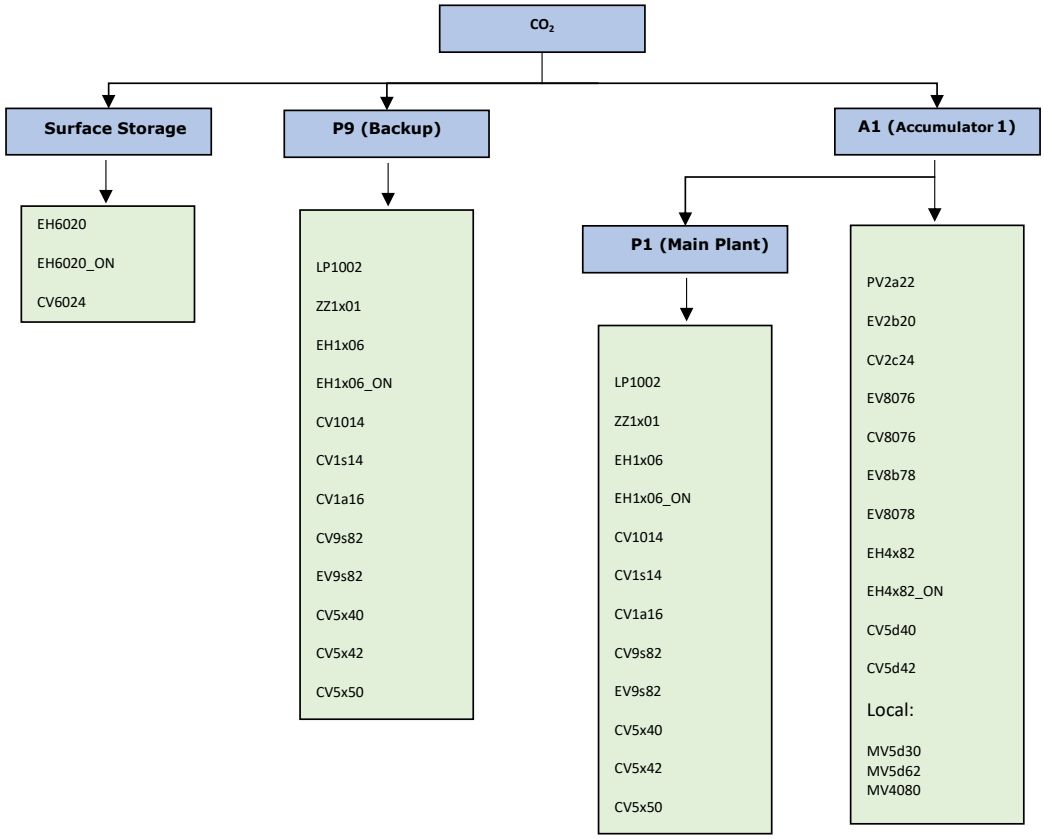

Figure 18: PCO Hierarchy [49]

3.6 Stepper Logic

The automated behaviour in Demo is executed by a PLC stepper logic. The logic checks at each stage that all conditions for the subsequent step are met before transitioning to that step. The detailed logic is elaborate and cannot be included in this report; nevertheless, the behaviour will be summarised.

T2PACL Plant Stepper (Without Surface Storage)

- **Step 0—Safety State:** The plant is off and in a safety state. All valves are in their safety positions to avoid liquid traps, and the pumps are off.
- **Step 1—Liquefy:** The controller for the valves on the primary side of the external heat exchanger at the pump inlet opens the valves to create subcooling in the pump inlet to ensure the pump has a supply of liquid CO_2.
- **Step 2 – Pump Startup:** Once the inlets of all heads are subcooled, the pump starts circulating the liquid CO_2 locally over valve (a) so that the flow does not prematurely go to the detector.
- **Step 3 – Deliver liquid:** Valve (b), which is controlled by a rate limiter, slowly opens and redirects flow towards the detector. The dP control valve (c), which is also controlled by a rate-limited controller, gradually builds differential pressure over the transfer lines so that the design flow may go through the detector.

- **Step 4 – Ready to swap:** The system is in its nominal operation and can swap out a failing plant on demand. This is achieved by opening the pneumatic valves (l) and (m) in Figure 54.

S2PACL Plant Stepper (With Surface Storage)

- **Step 0—Safety State:** The plant is off and in a safety state. All valves are in their respective safety states. That is, some valves are opened to avoid liquid traps, while some, such as the surface storage valves, are closed. The pumps are off as well.
- **Step 1 – Equalize:** The system pressure is equalised to that of the surface storage.
- **Step 2—Liquefy:** The controller for the valves on the primary side of the external heat exchanger at the pump inlet opens the valves to create subcooling in the pump inlet to ensure the pump has a supply of liquid CO_2.
- **Step 3 – Pump Startup:** Once the inlets of all heads are subcooled, the pump starts circulating the liquid CO_2 locally over valve (a) so that flow does not prematurely go to the detector.
- **Step 4 – Deliver liquid:** Valve (b), which is controlled by a rate, slowly opens and redirects flow towards the detector. The dP control valve (c), which is also controlled by a rate-limited controller, gradually builds differential pressure over the transfer lines so that the design flow may go through the detector.
- **Step 5 – Operation:** The plant has reached its nominal operating step, and the load may be turned on.
- **Step 6 – S2PACL to 2PACL:** This transition enables the operation to be changed from S2PACL to 2PACL mode.
- **Step 7 – S2PACL to S2PACL_StB:** This transition changes the mode of operation from S2PACL mode to S2PACL_StB mode.

The plant steppers above can be summarised by the grafcet in Figure 19 below.

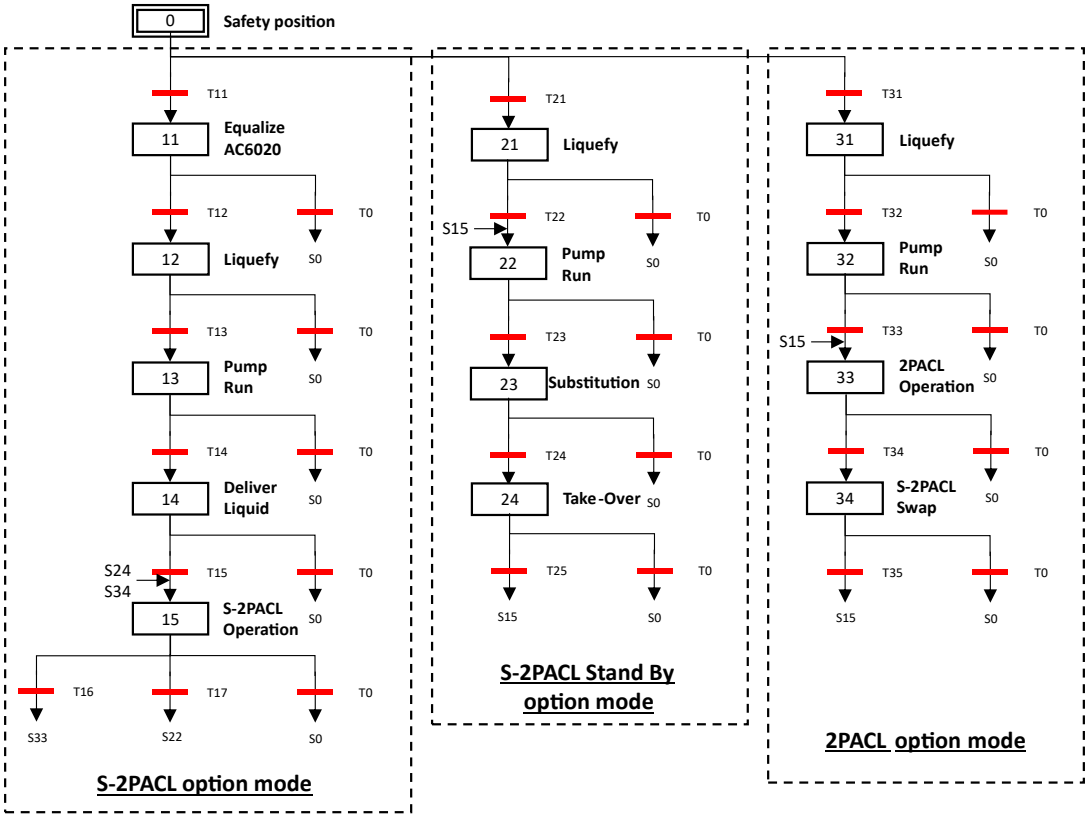

Figure 19: Demo Plant grafcet[49, 50]

Accumulator Operation Modes

The accumulator has only two operation modes, backup and main operation.

Accumulator Stepper

- **Step 0—Safety State:** The accumulator is in its safety state and requests that the plants also be off and in their respective safety states.
- **Step 1—Plant Startup:** The accumulator sends a run request to the Plant for the inlets of the pumps to be subcooled and circulation to begin.
- **Step 2 – Detector Pressurization:** The accumulator maintains the preset maximum pressure limit, and the pump flow is used to increase the detector pressure above the accumulator limit by throttling valve (g) – the BPR. The BPR controller increases this pressure in a rate-limited manner until the saturation temperature of the detector exceeds the actual detector temperature plus some margin, hence liquefying the CO_2 in the detector.
- **Step 3—Detector Circulation:** The detector is fully liquefied, and the differential pressure may be built across the detector using valve (c).
- **Step 4 – Accumulator Control:** The accumulator commences temperature control using the *split range controller*. A split range controller is one where multiple actuators respond to the common output of one controller, each actuator effectively responds in part of the full controller output range[51, 52].
- **Step 5 – Operation:** In this step, the accumulator can transition between the Main and Backup plant operation in the event of a trip.

The grafcet in Figure 20 summarises the accumulator steppers above.

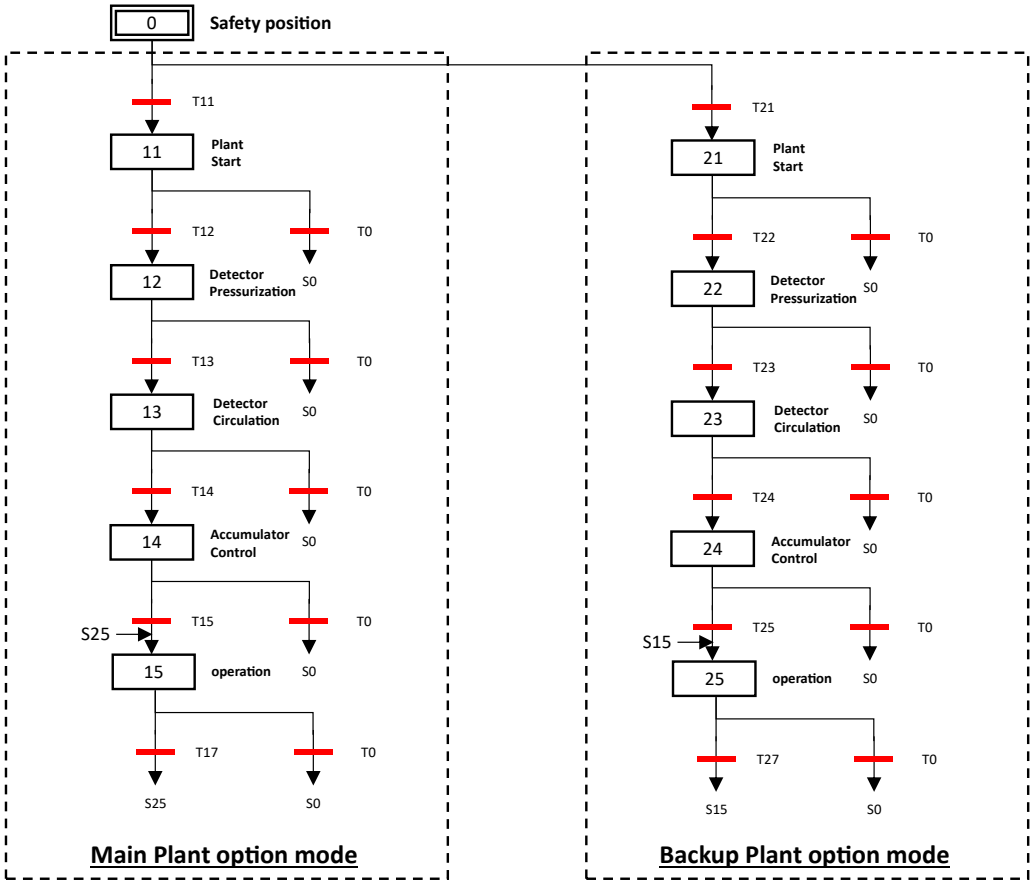

Figure 20: Demo accumulator grafcet[49]

In summary Figure 19 and Figure 20 above show that the system starts in safety mode and goes through a sequence of states separated by transition conditions (Bold horizontal bars). A subsequent state can only be reached if all the transition conditions are met. Each branch represents a mode of operation, such as S2PACL or T2PACL. The system can change branches as needed during operation. An operator with appropriate rights and operational needs can force such a change. A case in point is that if the main plant fails, the backup plant automatically changes operation from standby mode (S2PACL_StB) to its operation (S2PACL). Figure 20 The grafcet for the accumulator is shown above. The operation follows the same structure as the plant, except that the accumulator has its transition conditions.

4. Modelling

The map is not the territory.
– *Alfred Korzybski*

4.1 Modelling Philosophy

As mentioned in 1.2.3, the objective of modelling is to capture the dynamics of a physical system with high fidelity and range to gain insight into the problem. However, high-fidelity models are intricate to develop and come at a high time and computational costs. As such, a key consideration is to strike a balance between the complexity and detail of a model and the time and computational costs of developing and running such a model. This optimisation can be achieved in different ways discussed in 4.6.

The modelling of Demo was carried out using EcosimPro software by Empresario Agrupados Internacional S.A., which allows for the physical modelling of complex systems. EcosimPro has Cryolib and CO_2 libraries, which were co-developed in collaboration with CERN, making it the preferred tool for modelling the intricate thermodynamics of two-phase CO_2 flow. Figure 21 is the library architecture of the DEMO library, alongside its dependencies - namely CO2, MATH, CRYOLIB, PLC, PORTS_LIB, THERMAL, and THERMO_TABLE_INTERP. It reflects a 'uses-a' relationship where solid lines denote the dependencies of the DEMO library itself, while dotted lines illustrate the complex interdependencies among the remaining libraries. Central to this architecture is the MATH library, which is fundamental to all other libraries due to its universal applicability and lack of dependencies, thus positioning it at the core of the library hierarchy.

In a nutshell, the CONTROL and PLC libraries house control objects and interfaces to connect the simulation to external hardware such as a PLC. CRYOLIB and CO_2 are libraries for modelling complex fluid systems. CO_2 inherits some constructs from CRYOLIB but is specially developed for CO_2-based detector cooling systems and differs in the way it handles two-phase flow and momentum equations. THERMAL and THERMO_TABLE_INTERP libraries contain material and fluid properties, respectively. Fundamentally, PORTS_LIB facilitates the exchange of variables between components.

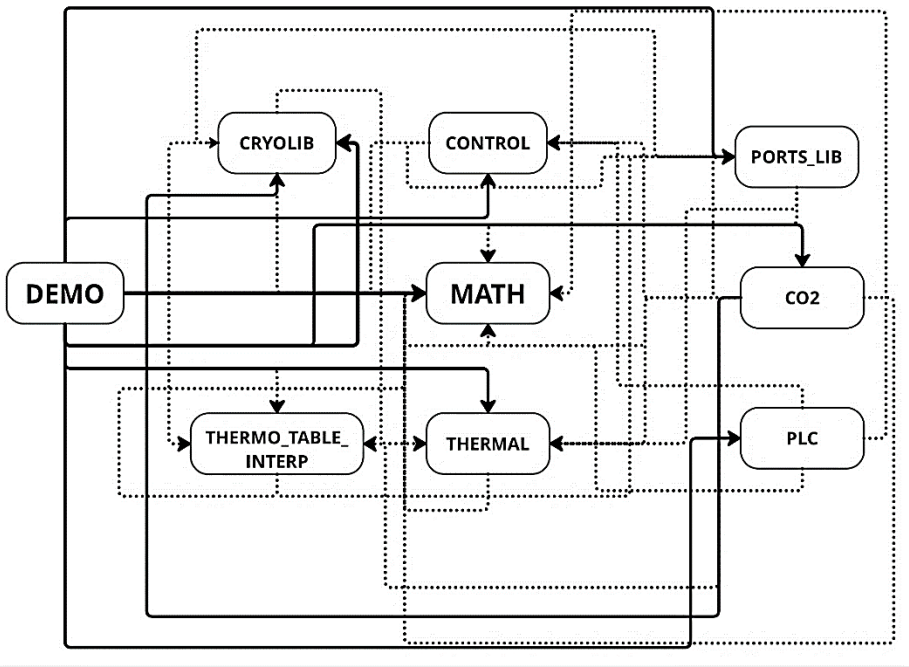

Figure 21: Demo library (left) and its dependencies (right) [Created from EcosimPro]

The development followed the modelling pipeline described by Figure 12 in 1.2.3. It involved creating a library – DEMO – where the model is located. Subsequently, the various components were modelled in the library and corresponding graphical representation where needed. Then, the model was compiled, and its partition –a mathematical model instance of the system – was generated. This concluded modelling. The simulation step comprised creating an experiment file, which defined the boundary conditions and the simulation parameters, such as the initial condition and the communication interval (CINT), respectively.

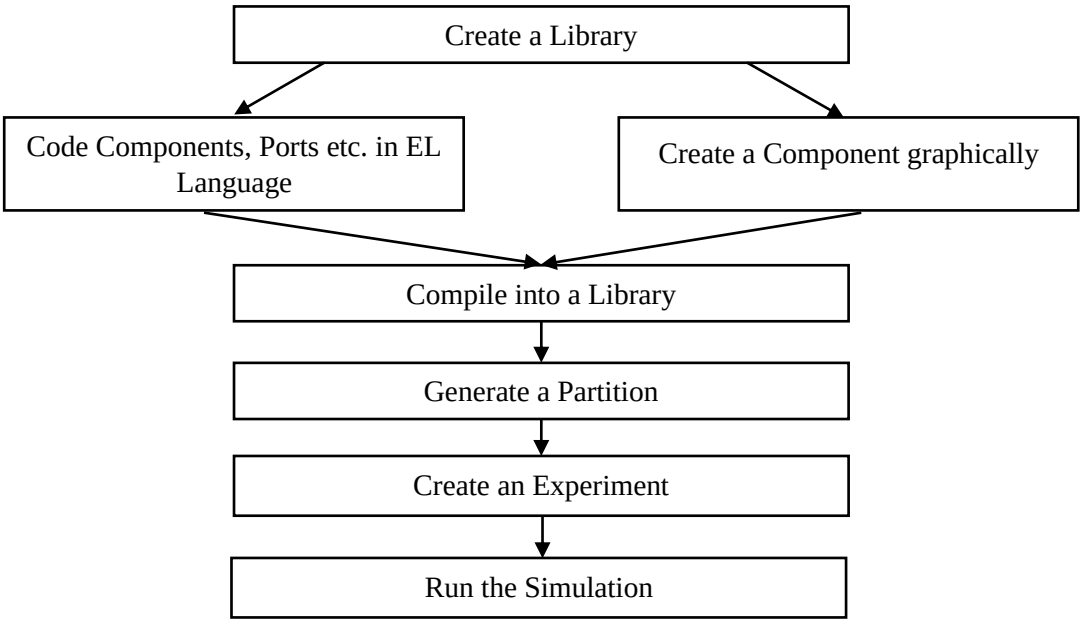

Figure 22: Modelling pipeline[53]

One advantage of modelling in EcosimPro is that the software allows the model to benefit from its *acausal* and *object-oriented* capabilities. Acausal modelling means the modeller can declare equations and relationships in any order, and the compiler determines the order necessary for successful computation. Object-oriented modelling embraces *inheritance*, *aggregation* and *encapsulation* – allowing for modular bottom-up modelling. In this way, time was not wasted on ensuring that the equations were in the correct order, and the integrity of subcomponents could be validated at a lower level before composition with other components was done for more intricate components, making debugging more effortless.

4.1.1 Inheritance

Inheritance in EcosimPro Language (EL), just like other languages like Java and C++, allows for a parent component to be defined such that a child component can extend the base functionality of the parent, as shown in the insert below. The child component adds more specialised functionality to capture more specialised behaviour. This is achieved by a statement below, which means that a CO_2 Accumulator inherits all attributes and functionalities of a Tank. Unto this, more specialised attributes will be added, which will only apply to the CO_2 Accumulator and its child components.

```
1.  COMPONENT CO2Accumulator IS_A Tank
```

4.1.2 Aggregation

A component can be modelled such that it contains multiple instances of other components. These components can then be interacted with, modified or deleted independently, improving portability and code reuse. An example is that of the chiller in Figure 23 below. It has two instances of the heat exchanger and multiple pipes, PI controllers, and pressure drop elements internally, all of which can be interacted with independently.

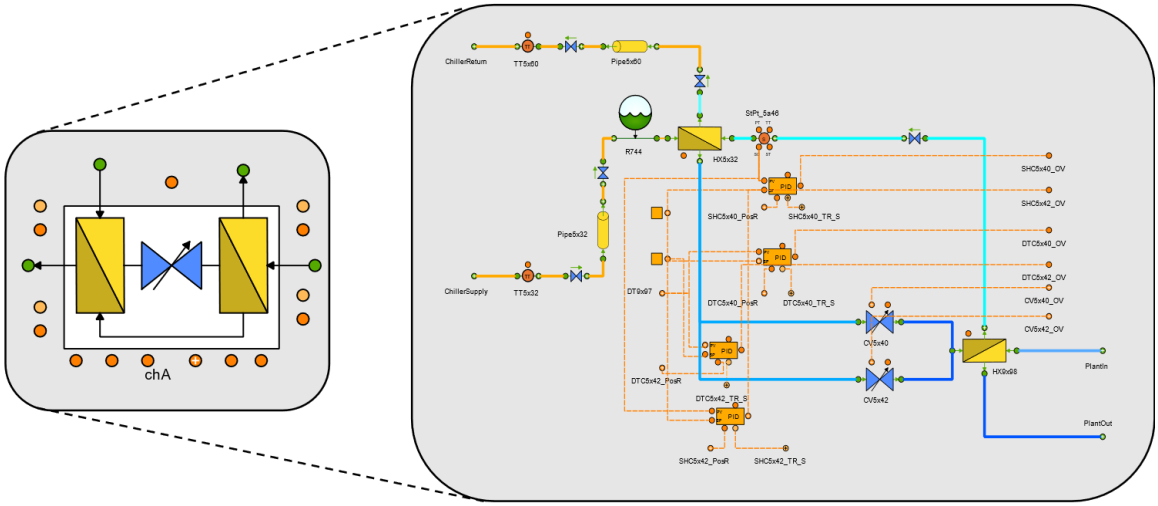

Figure 23: Chiller Aggregation [Generated in EcosimPro]

4.1.3 Encapsulation

By employing encapsulation and abstraction, the modeller can hide all the complexities in a component so that the library user only needs to worry about making the port connections. These connections, along with their behaviour and restrictions, have been predefined, which makes the modelling much faster, as the user does not need to worry about the relationship between different equations.

4.2 Modelling Fundamentals

EcosimPro uses finite-volume capacitive-inductive modelling, which decouples the momentum equations from the continuity and energy balance equations. The model is treated as a 1D, which averages physical quantities over a cross-section perpendicular to the main direction of flow. This reduction in dimensionality is key for improving the simulation's computation speed. Furthermore, the 1D offers the flexibility of choosing the spatial resolution while capturing the intricate system dynamics over large transients. In essence, this approach reduces the problem from high dimensionality Partial Differential Equations (PDEs) to Differential Algebraic Equations (DAEs) – where the derivatives of the state variable with respect to space are eliminated and only time derivatives remain [54].

Finally, pressure drop modelling also adopts the steady-state method by Wetter [32, 55]. The steady-state approach significantly reduces the *stiffness* that would otherwise result. Stiffness is a phenomenon where a solver takes infinitesimally small steps to converge when the equation has both fast and slow solution curves [31]. The eigenvalues of a Jacobian of a model indicate its stiffness; the more significant the variation in the magnitude of the eigenvalues, the stiffer a model is. When pressure states are included in the model, the eigenvalues of the Jacobian can vary by a factor of 10^4 to 10^6, such stiffness makes computation significantly slow. For further simplification, only steady-state terms are considered for the momentum equations because these approximate those of more intricate transient models well while improving the computational speed of finite volume models [34, 39, 56].

At a given pressure, the capacitive components in the model fundamentally conserve mass and energy, as described by the equations below [5, 23, 57].

The mass balance equation is given by equation 3 below.

$$\frac{\partial \rho}{\partial t} + \frac{\partial (\rho v)}{\partial x} = 0 \tag{3}$$

While equation 4 is the energy conservation [57, 58].

$$\frac{\partial (\rho u V)}{\partial t} + \frac{\partial (\rho v h)}{\partial x} = \delta \dot{Q} \tag{4}$$

Where h, u, P, ρ, t, v, x are the specific enthalpy, specific internal energy, pressure, density, time, specific volume and the spatial coordinate along the direction of flow, respectively.

Capacitive components in the model have storage and conserve mass, and since the density is expressed as a function of the other two state variables.

$$\rho = f(P, h) \tag{5}$$

Then, by chain rule,

$$\frac{\partial \rho}{\partial t} = \frac{\partial \rho}{\partial P}\frac{dP}{dt}\Big|_h + \frac{\partial \rho}{\partial h}\frac{dh}{dt}\Big|_P \tag{6}$$

This means the mass conservation equation can be expressed thus;

$$\frac{\partial (\rho V)}{\partial t} = \frac{dm}{dt} = V\left(\frac{\partial \rho}{\partial P}\frac{dP}{dt}\Big|_h + \frac{\partial \rho}{\partial h}\frac{dh}{dt}\Big|_P\right) \tag{7}$$

$$V\left(\frac{\partial \rho}{\partial P}\frac{dP}{dt}\Big|_h + \frac{\partial \rho}{\partial h}\frac{dh}{dt}\Big|_P\right) = \dot{m}_{in} - \dot{m}_{out} \tag{8}$$

The specific enthalpy is,

$$h = u + {}^{P}/_{\rho} \tag{9}$$

Where h, u, P, ρ are the specific enthalpy, specific internal energy, pressure, and density. Making the specific internal energy the subject of the formula;

$$u = h - {}^{P}/_{\rho} \tag{10}$$

Therefore, the energy conservation equation is as follows,

$$\frac{\partial (\rho h - P)V}{\partial t} = \frac{dQ}{dt} = V\left(h\frac{\partial \rho}{\partial P}\frac{dP}{dt}\Big|_h - \frac{dP}{dt}\Big|_h + h\frac{\partial \rho}{\partial h}\frac{dh}{dt}\Big|_P + \rho\frac{dh}{dt}\Big|_P\right) \tag{11}$$

$$V\left(h\frac{\partial \rho}{\partial P}\frac{dP}{dt}\Big|_h - \frac{dP}{dt}\Big|_h + h\frac{\partial \rho}{\partial h}\frac{dh}{dt}\Big|_P + \rho\frac{dh}{dt}\Big|_P\right) = \dot{m}_{in}h_{in} - \dot{m}_{out}h_{out} + \dot{q} \tag{12}$$

$$V\left(\left(h\frac{\partial \rho}{\partial P}\Big|_h - 1\right)\frac{dP}{dt} + \left(h\frac{\partial \rho}{\partial h}\Big|_P + \rho\right)\frac{dh}{dt}\right) = \dot{m}_{in}h_{in} - \dot{m}_{out}h_{out} + \dot{q} \tag{13}$$

By conserving mass and energy in a controlled volume in this manner, more complex behaviour can be modelled by using many of these and other elements such as pressure drops, heat sources, etc.

4.2.1 Assumptions

The following assumptions were made [5].

1. The system is assumed to be 1D – Properties are averaged over a cross-section
2. Axial heat conduction neglected
3. Viscous dissipation is negligible

4.3 System Modelling

To model the system, the Piping and Instrumentation diagram (P&ID) of the system was studied, and components were connected in an arrangement matching that on the P&ID. Thereafter, the PLC logic was studied extensively as it informs the logic executed by the PCO. The PCO is the model's central processing unit, and it emulates the task of a PLC in driving the various field objects during simulation. The Demo prototype has multiple PCOs, one for each of the main subsystems. For the purpose of this research, the PCOs of interest include the main and backup plants PCO and the Accumulator PCO. The model also incorporates these three PCOs of interest, as shown in the top right corner of Figure 58 and Figure 59, and the top left corner of Figure 60 in the appendices A1 through A3.

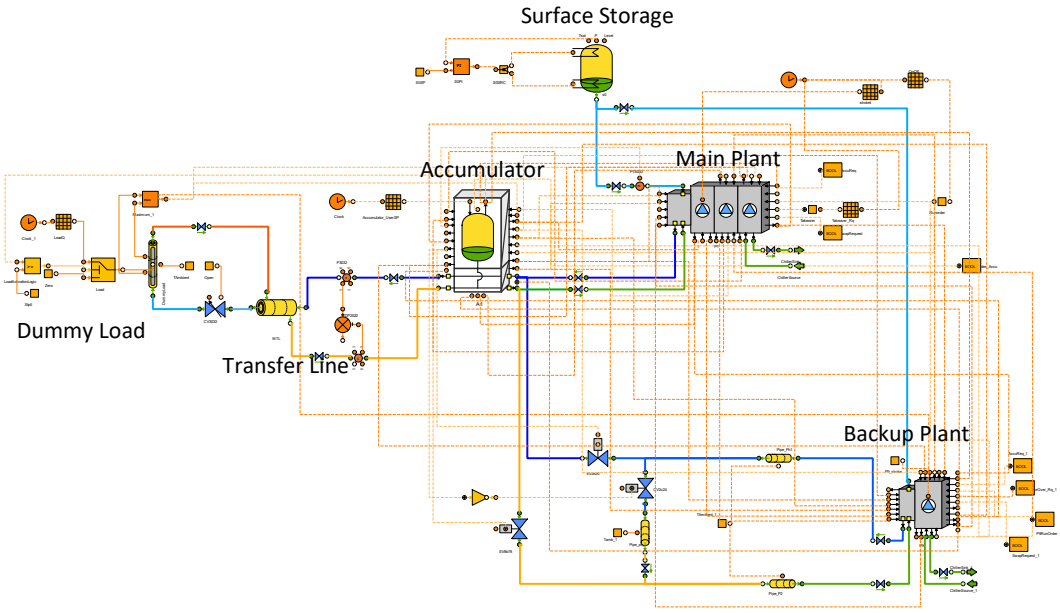

Figure 24: The Demo Model [Created in EcosimPro]

Figure 24 is the resulting model of Demo. It has the main plant with three pump heads, the single-head backup plant on the bottom right, the accumulator, surface storage, coaxial heat exchanger and a dummy load. The dotted lines in the figure represent electrical signals, while the solid bold lines represent the main flow paths in the system.

4.4 Model Calibration

Calibration is conducted after validating that the model architecture matches the system's P&ID. First, various components are sized using the part-list database and Engineering & Equipment Data Management Service (EDMS) records that CERN kept during the development of the Demo prototype. This ensures that the resulting behaviour, including transients, is representative of the actual system. Figure 25 illustrates how an entry for a valve in the part list database is used to size the corresponding valve in the model.

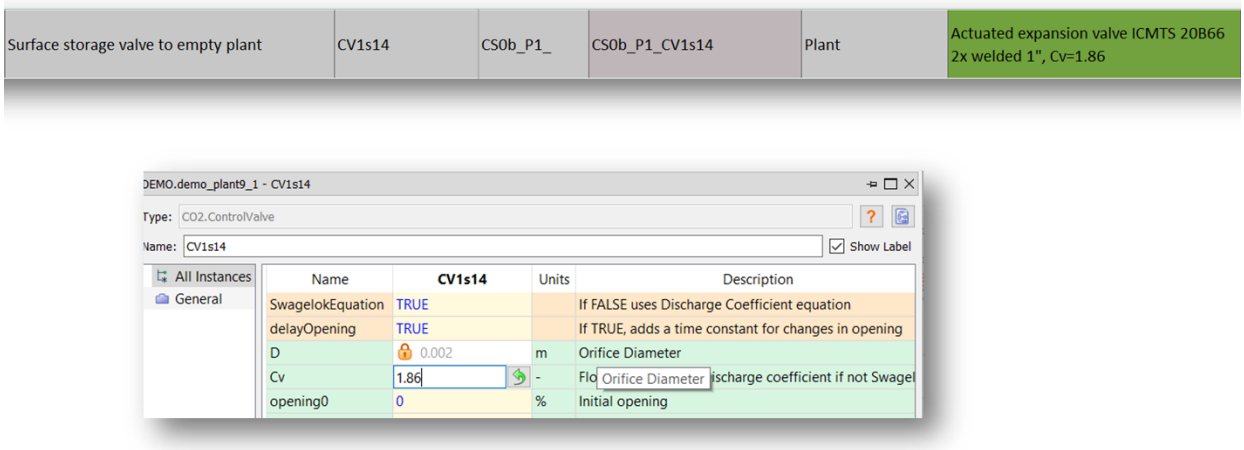

Figure 25: Valve parameterisation – Part list sheet (top), EcosimPro (bottom)[59]

4.5 Process Control Object (PCO)

The digital twin is driven by a PCO block, which executes logic identical to that of the PLC in the real system. Much of the logic executed by the system is discrete. An example is when all the conditions for a subsequent stepper are met, the PCO transitions to the next stepper. In essence, this is switching to a different branch of the selection tree and replacing all the previous equations with those relevant to the active branch. The PCO makes many such transitions during operation as various metrics evolve. This makes the model of Demo a hybrid model.

4.6 Model Optimisation

Upon completion of the calibration, the model is compiled, and a partition is created. Figure 26 shows the characteristics of the partition. The figure confirms that the model is a differential algebraic Equation (DAE) system with a high Jacobian *sparsity factor* of 93% depicted below. DAE models are a more computationally expensive generalisation of ODEs with algebraic constraints that reduce the degrees of freedom in solving.

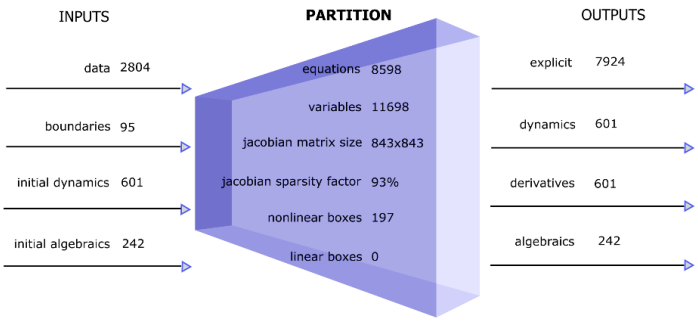

Figure 26: Demo model partition [Generated in EcosimPro]

4.6.1 Solver Choice

EcosimPro offers a variety of solvers for both Ordinary Differential Equations (ODEs) and DAEs. For DAEs, EcosimPro has the Differential Algebraic System Solver (DASSL) and Implicit Differential-Algebraic Solver (IDAS) along with their 'sparse' variants - DASSL_SPARSE and the IDAS_SPARSE as well as the Adams-Moulton solvers (AM1 to AM4). DASSL and IDAS are variable step-size solvers with step-size control algorithms, and their sparse variants allow them to exploit Jacobian sparsity. In particular, DASSL also uses the Lower-Triangular Upper-Triangular (LU) decomposition for sparse Jacobian matrices to improve speed [53]. As such, DASSL_SPARSE was chosen because it was robust enough to converge for the model, all while offering automatic step size control and exploiting the sparsity.

Generally, a solution for generic DAE in EcosimPro centres on replacing time derivatives with approximation differences and solving the resulting equations for t_n using implicit Powell's Hybrid Method. An example is shown below [53, 60].

$$F\left[t_n, y_n, \frac{y_n - y_{n-1}}{t_n - t_{n-1}}\right] = 0 \tag{14}$$

Powell's dogleg method, also called Powell's hybrid method, minimises the sum of the squares of the function values by using a combination of Newton's method and the steepest descent method, which is known as the trust region method [53]. This makes the method more stable than Newton's method. Equation 15 shows Powell's hybrid method [53, 60].

$$y_n^{m+1} = y_n^m - \left(\frac{\partial F}{\partial y} + \frac{1}{\Delta t_n} \cdot \frac{\partial F}{\partial y}\right)^{-1} \cdot F\left(t_n, y_n^m, \frac{y_n^m - y_{n-1}^m}{\Delta t_n}\right) \tag{15}$$

Where m is the iteration index.

The solver finally checks the convergence using tolerance calculated in the following manner.

```
1. --Tolerance
2. abs(local_error) <= (ABS_ERROR+REL_ERROR*abs(Y))
```

The step size for the solver was chosen to be 2.06 which is reasonably high while still allowing convergence. This value is in essence the maximum value and the solver step-size algorithm can change int to any value below as needed based on the stiffness of the model. As for the number of elements, the pipe elements were set to have three segments each which gave

insights into how the metrics evolved along the length of the pipe while also still allowing for the model to run reasonably fast. As for the heat exchanger, each had 5 segments which were also chosen to strike a balance between spatial resolution and model speed. This followed the observation that increasing the number of segments to a high number reduced the model speed.

4.6.2 Mass Flow Regularization

DAE solvers, including DASSL, often encounter challenges related to convergence in low-flow conditions [35]. This is because the derivatives of mass flow with respect to pressure drop tend to infinity as mass flow tends to zero. The unregularised plot in Figure 27 captures this behaviour, showing the range from reverse to forward flow. It shows that the slope of the mass flow versus pressure-drop plot tends to infinity close to the origin when flow changes direction. The result is that the solver oscillates at high frequencies due to this high sensitivity of mass flow to instantaneous changes in pressure drop [35]. Therefore, regularising mass flow close to the origin is necessary to improve solver speed and stability. Hao et al. found that regularisation improves the solver speed considerably, specifically, the following equation can be used for the regularisation [35, 57];

$$\dot{m} = \frac{\dot{m}_0}{\sqrt{dP_0}} (dP)^b \left(dP^2 + \Delta_p\right)^{\left(\frac{a-b}{2}\right)} \tag{16}$$

$$\dot{m} = \left(\frac{\dot{m}_0}{\sqrt{dP_0}}\right) \left(\frac{(dP)^b \left(\sqrt{dP^2+\Delta_p}\right)^a}{\left(\sqrt{dP^2+\Delta_p}\right)^b} \right) \tag{18}$$

Where $\dot{m}, m_0, dP, dP_0, \Delta_p$ are the mass flow, nominal mass flow, pressure drop, and nominal pressure drop regularisation band, respectively. a, b are the dimensionless regularization parameters used to get the desired regularisation profile. From the expression above, it is evident that different combinations of the coefficients yield different fits. The combination $(a = b = 0.5)$ results in the standard unregularised relationship between mass flow and differential pressure.

$$\dot{m} = \dot{m}_0 \sqrt{\frac{dP}{dP_0}} \tag{17}$$

Figure 27 shows the plots for the mass flow when regularised with different profiles. When $(a = 0.5,\ b = 1)$, the result is a linear fit between the bounds of the predefined regularisation band. For the combination $(a = 0.5,\ b = 3)$, cubic interpolation results, and it is flatter at the origin, favouring the solver. Finally, a quintic fit is obtained from $(a = 0.5,\ b = 5)$, which is even more aggressive and flatter. It is worth noticing that an inherent trade-off that comes with regularisation is the accuracy of $\dot{m}$ at low flow versus the increased stability and solver speed. This is seen in that as the order of the regularisation is increased, the plots deviate further from the true $\dot{m}$ (unregularised), because there now exists a dead band were, for a finite non-zero pressure, a zero mass-flow results. Consequently, it is crucial to balance these two important metrics. For this reason, the pair $(a = 0.5,\ b = 3)$ have been used while modelling.

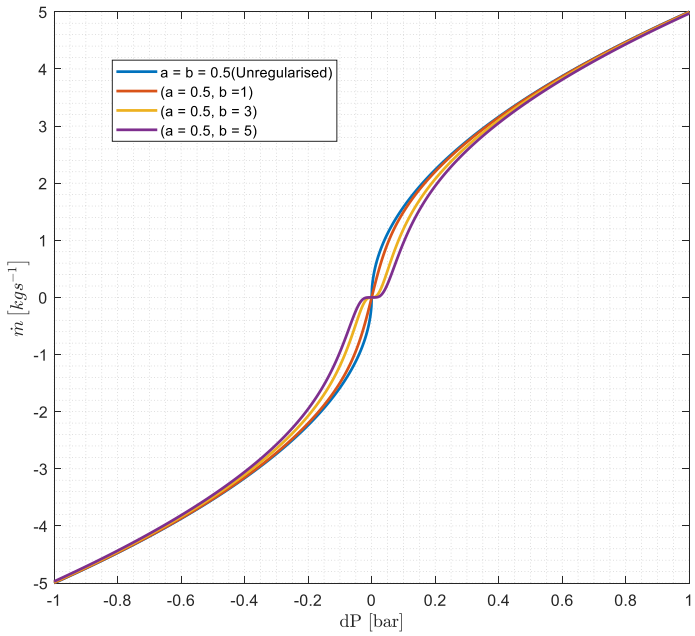

Figure 27: Mass Flow Regularization [Generated in MATLAB]

4.6.3 State Saving

During the process of modelling, validation was done at each level to ensure that the model accurately captured the behaviour of Demo. It was common to find that a logical or solver error occurred at some time T well into the simulation interval. The subsequent investigation meant the model was run iteratively as the solution is being structured, and running from the beginning is inefficient because the plants start in Safety mode where there is no flow, resulting in slow simulation. To circumvent this, a state file, which includes all the variable values, Jacobians, derivatives of variables and other information about the state of the model at the time instance, is saved just before the point of interest. Afterwards, iterations are done much faster using this an initial condition.

4.6.4 Discontinuity Handling

Smoothing was also done for the HTC at the phase boundaries. The method uses a hyperbolic tangent to smooth the HTC in a predefined band at the phase boundaries. This ensures that the HTC function is continuous which improves solver stability. Additionally, the code calls only the single-phase correlation except when in it is in the preset splicing band – in this case $\Delta x = 0.1$ around the phase boundaries. This ensures that minimal calls were made to the correlation function because some – like the Colebrook equation are implicit and solved iteratively using non-linear solvers, which is computationally costly.

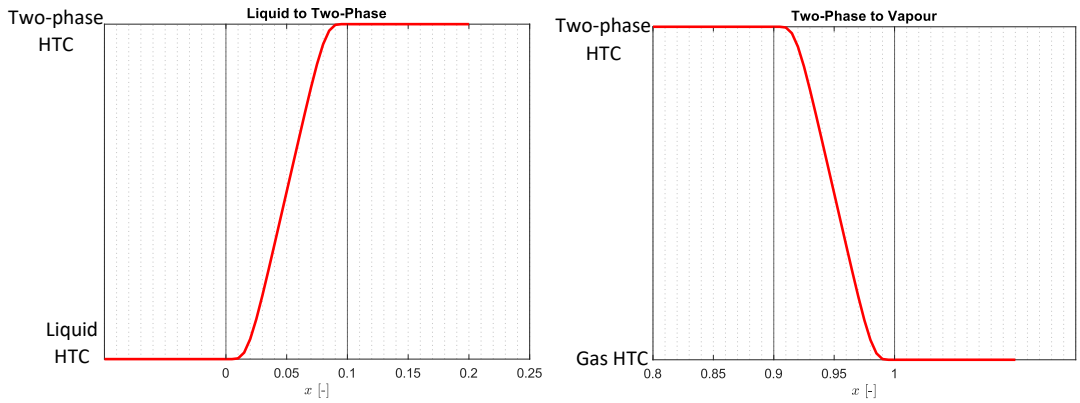

Figure 28: HTC Smoothing [Generated in MATLAB]

4.7 Key Plant Dynamics

4.7.1 Pump Inlet Subcooling Dynamics

As mentioned in 3, it is crucial for the operation of the 2PACL system to maintain a constant supply of subcooled liquid at the pump inlet. The external heat exchangers responsible for subcooling operate under vastly different conditions. In flowthrough mode, these heat exchangers need only to subcool the saturated CO_2, which has already been condensed in the accumulator. On the Operation P-h diagram in Figure 17, this means changing the specific enthalpy from **state point 8** to **1**, in order for the accumulator pressure to be controlled. Contrarily, in non-flow-through mode, the external heat exchangers must condense and then subcool the CO_2 which means changing the specific enthalpy from **state point 7** to **1**. The mass flow on the 2PACL side is constant and imposed by the pump, hence to keep up with the specific enthalpy change requirements in either mode, the chiller mass flow must change significantly. The equation below summarises the global energy conservation at the chiller interface.

$$\dot{m}_{ch}\Delta h_{ch} = \dot{m}_{2PACL}\Delta h_{2PACL}$$

A challenge that arises is that valves have limited ranges in which they exhibit desirable flow-C_v characteristics. A valve that is oversized operating continuously at a low lift (close to being closed) is undesirable because here the valve has flow characteristics that differ from the nominal range; this is also the case for an undersized valve that continuously operates at a high lift. To circumvent this problem, the system features four controllers that manage two valves – one with a bigger C_v of 0.42 and a smaller valve with a C_v of 0.21 shown in Figure 29. Each pair of controllers operates one valve, and the PCO executes selection logic to determine the active controller. In flowthrough mode, substantially lower mass flow is needed on the chiller side, hence the PCO selects the small valve to regulate the subcooling, and the big valve remains closed and inactive to hand over regulation solely to the small valve. Conversely, in non-flowthrough mode, much larger flow rates are needed on the primary side. Consequently, the PCO activates the controller linked to the big valve. This ensures that the regulating valve always operates in its nominal range which improves the valve *rangeability*. Valve rangeability refers to the ratio of the maximum controllable flow to the minimum controllable flow of a

valve. This approach also enhances resolution because, to achieve the same pressure drop at a flow lower than the aforementioned point, the valve needs to travel more.

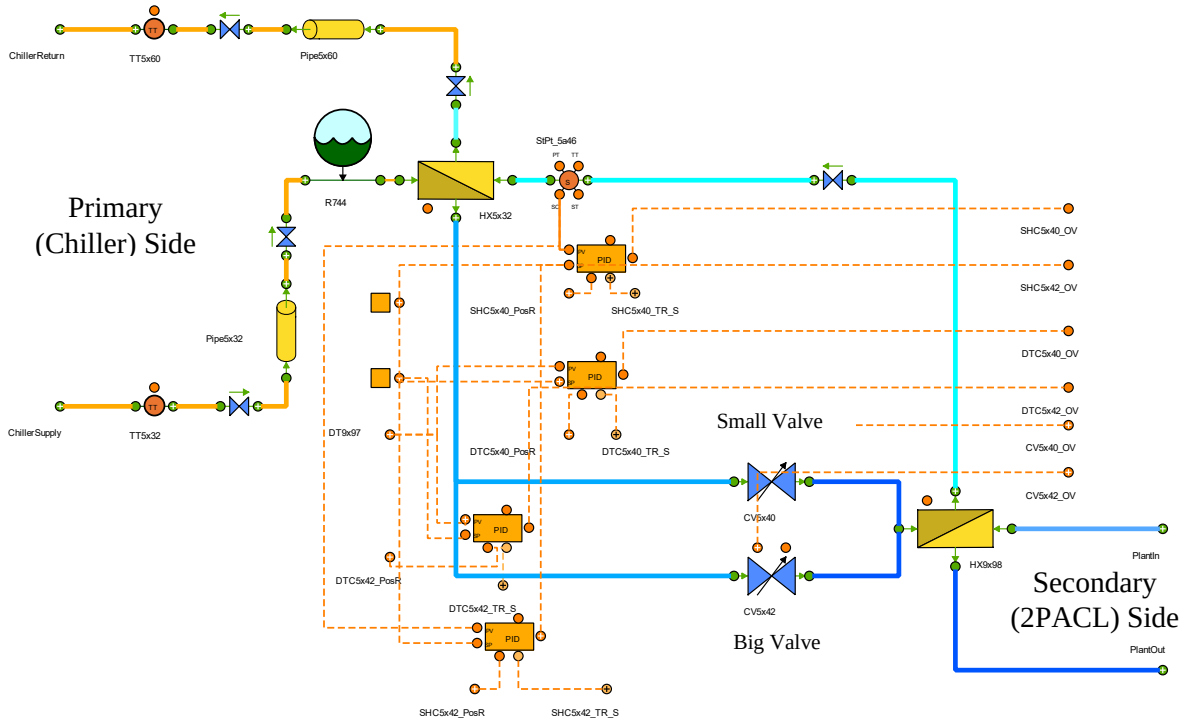

Figure 29: Chiller Module [Generated in EcosimPro]

The pump inlet subcooling is controlled by controlling the mass flow rate of the refrigerant on the primary chiller side. The chiller has two modes of control – namely, Differential Temperature Control (DTC) and Superheat Control (SHC). In DTC, the PCO regulates the pump inlet subcooling so that the absolute temperature of the pump inlet is always a set value below the saturation at operation. In SHC, the PCO controls the exit superheat of the external heat exchanger (HX9x98) on the chiller side. In doing this, the pump inlet is exposed to the maximum chiller capacity because the aim is to get a preset superheat at the outlet. The DTC mode is used when the system operates at temperatures warmer than or equal to -40˚C. Otherwise, the PCO initiates the SHC mode, allowing the system to operate stably as it approaches its limit (-45˚C).

4.7.2 The Detector Temperature Dynamics

Accumulator Temperature Control

The accumulator is at the core of pressure control in the 2PACL system, which in turn speaks to temperature control. In order to design and test the controller for this subsystem. Its dynamic mathematical model that captures its temperature dynamics needs to be formulated. The accumulator is a thermodynamically *open system*, which means mass and/or energy can cross the boundary. A dynamic model of a system comprises state variables, and these quantities must not depend on the history of the system's past states. Additionally, because the accumulator will operate in the two-phase region, the chosen state variables are specific

enthalpy and density. This choice is advantageous because both are intensive variables and independent of each other, even in the two-phase region [54].

A homogenous accumulator model also respects the mass and energy conservation equations for open systems [61].

Mass Conservation

$$\frac{dm}{dt} = \dot{m}_{in} - \dot{m}_{out} \tag{18}$$

m, $\dot{m}_{in}$ and $\dot{m}_{out}$ are the mass in the accumulator, the mass flow rate out and in, respectively.

Energy Conservation

The specific internal energy equation is given by equation 19 below.

$$u = h - {}^{P}/_{\rho} \tag{19}$$

Where h, ρ, P are the averaged specific enthalpy, averaged density and pressure respectively. Multiplying both sides of this equation by mass yields the internal energy equation below.

$$U = H - PV \tag{20}$$

Where U, H, P and V are the internal energy, total enthalpy, pressure and volume, respectively.

$$\frac{d}{dt}(H - PV) = \dot{m}_{in}h_{in} - \dot{m}_{out}h_{out} + \dot{q} \tag{21}$$

The equation states that the net enthalpy inflow or outflow and the heating or cooling action drive the change in the total internal energy of the accumulator;

$$\frac{d}{dt}(mh - PV) = \dot{m}_{in}h_{in} - \dot{m}_{out}h_{out} + \dot{q} \tag{22}$$

$$m\frac{dh}{dt} + h\frac{dm}{dt} - V\frac{dP}{dt} = \dot{m}_{in}h_{in} - \dot{m}_{out}h_{out} + \dot{q} \tag{23}$$

Where m, h, Substituting for $\dot{m}$ and rearranging,

$$m\frac{dh}{dt} = \dot{m}_{in}h_{in} - \dot{m}_{out}h_{out} - (\dot{m}_{in} - \dot{m}_{out})h + \dot{P}V + \dot{q} \tag{24}$$

If mass and specific enthalpy are chosen as the state variables, then;

$$\frac{dP}{dt} = \frac{\partial P}{\partial h}\Big|_{\rho}\frac{dh}{dt} + \frac{\partial P}{\partial \rho}\Big|_{h}\frac{d\rho}{dt} \tag{25}$$

Substituting for the derivative of density in 25, the equation becomes;

$$\frac{dP}{dt} = \frac{\partial P}{\partial h}\Big|_{\rho}\frac{dh}{dt} + \frac{\partial P}{\partial \rho}\Big|_{h}\left(\frac{\dot{m}_{in} - \dot{m}_{out}}{V}\right) \tag{26}$$

Substituting 25 into 26;

$$m\frac{dh}{dt} = \left(\dot{m}_{in}(h_{in} - h) - \dot{m}_{out}(h_{out} - h) + V\left(\frac{\partial P}{\partial h}\Big|_{\rho}\frac{dh}{dt} + \frac{\partial P}{\partial \rho}\Big|_{h}\left(\frac{\dot{m}_{in} - \dot{m}_{out}}{V}\right)\right) + \dot{q}\right) \tag{27}$$

$$m\frac{dh}{dt} - V\frac{\partial P}{\partial h}\Big|_{\rho}\frac{dh}{dt} = \left(\dot{m}_{in}(h_{in} - h) - \dot{m}_{out}(h_{out} - h) + \frac{\partial P}{\partial \rho}\Big|_{h}(\dot{m}_{in} - \dot{m}_{out}) + \dot{q}\right) \tag{28}$$

$$\frac{dh}{dt} = \frac{\left(\dot{m}_{in}\left(h_{in} - h + \frac{\partial P}{\partial \rho}\Big|_h\right) - \dot{m}_{out}\left(h_{out} - h + \frac{\partial P}{\partial \rho}\Big|_h\right) + \dot{q}\right)}{V\left(\rho - \frac{\partial P}{\partial h}\Big|_\rho\right)} \tag{29}$$

The terms $\frac{\partial P}{\partial \rho}|_h$ and $\frac{\partial P}{\partial h}|_\rho$ can be found using Reference Fluid Thermodynamic and Transport Properties (REFPROP) database and the corrected enthalpy and density terms are plotted in Figure 30 below.

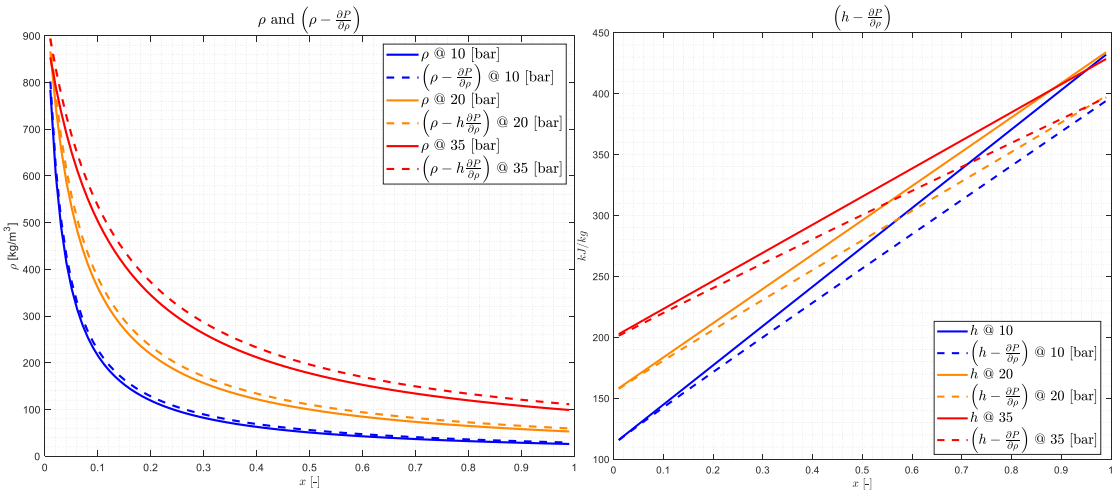

Figure 30: Property-corrected density and specific enthalpy [Generated using MATLAB REFPROP]

Figure 30 the comparison between the corrected enthalpy and density terms from equation 32. The figure shows that the uncertainty space from unmodified density covers the enthalpy-corrected terms and, in essence, includes the bounding cases. Hence for the design, equation 32 can be approximated by the simplified equation below.

$$\frac{dh}{dt} \approx \frac{(-\dot{m}_{in}h + \dot{m}_{out}h + \dot{m}_{in}h_{in} - \dot{m}_{out}h_{out} + \dot{q})}{m} \tag{30}$$

Which can then be rearranged thus;

$$\frac{dh}{dt} = \frac{-(\dot{m}_{in}h - \dot{m}_{out}h) - \dot{m}_{out}h_{out}}{m} + \frac{\dot{m}_{in}h_{in}}{m} + \frac{\dot{q}}{m} \tag{31}$$

In the case of the accumulator for Demo, only saturated liquid flows out so that;

$$\frac{dh}{dt} = \frac{-(\dot{m}_{in}h - \dot{m}_{out}h) - \dot{m}_{out}h_l}{m} + \frac{\dot{m}_{in}h_{in}}{m} + \frac{\dot{q}}{m}$$

Where h_l is the specific enthalpy of saturated liquid CO_2 leaving the tank. h_l is itself coupled to the averaged specific enthalpy through the pressure loop. This term can be numerically approximated using REFPROP in MATLAB, and used to find its uncertainty space.

$$\Delta h_l \approx \left(\frac{\partial h_l}{\partial h}\Big|_\rho\right)\Delta h$$

The complete forward loop becomes;

$$\frac{dh}{dt} = \frac{-(\dot{m}_{in}h - \dot{m}_{out}h) - \left(\frac{\partial h_l}{\partial h}\Big|_\rho\right)\dot{m}_{out}h}{m} + \frac{\dot{m}_{in}h_{in}}{m} + \frac{\dot{q}}{m}$$

The first term characterises the dynamics of the system, the second term is the disturbance that must be rejected, and the last term is the input.

$$\frac{dh}{dt} = \frac{-(\dot{m}_{in}h - \dot{m}_{out}h) - \left(\frac{\partial h_l}{\partial h}\Big|_{\rho}\right)\dot{m}_{out}h}{m} + \frac{\dot{q}}{m} \tag{32}$$

Using Vidyasagar's theorem for *Slow Varying Systems* – a condition which the accumulator meets at quasi-steady state, local linearization of the plant is done at different operating points so that its non-linear dynamics are represented by a set of linear time-invariant (LTI) plant cases, where a controller that stabilizes these plant cases will also stabilize the accumulator despite it being a non-linear system [62, 63].

The accumulator can be represented by the following non-LTI state space representation.

$$\dot{\boldsymbol{x}} = \boldsymbol{f}(t, x(t), u(t)) \tag{33}$$

$$\boldsymbol{y} = \boldsymbol{h}(t, x(t), u(t)) \tag{34}$$

A state space representation for a linear system given by the equation below.

$$\dot{\boldsymbol{x}} = \boldsymbol{A}\boldsymbol{x}(\boldsymbol{t}) + \boldsymbol{B}\boldsymbol{u}(\boldsymbol{t}) \tag{35}$$

Which can be simply written as:

$$\dot{\boldsymbol{x}} = \boldsymbol{A}\boldsymbol{x} + \boldsymbol{B}\boldsymbol{u} \tag{36}$$

Where $\dot{\boldsymbol{x}}$,$\boldsymbol{x}$, $\boldsymbol{A}$ $\boldsymbol{B}$, and $\boldsymbol{u}$ are the state derivatives vector, the state variables vector, the system dynamics matrix the input matrix and the inputs vector respectively.

The algebraic output equation for a linear system is then given by:

$$\boldsymbol{y} = \boldsymbol{C}\boldsymbol{x} + \boldsymbol{D}\boldsymbol{u} \tag{37}$$

Where;

$$\boldsymbol{y} = \begin{pmatrix} h \\ m \end{pmatrix} \tag{38}$$

$$\boldsymbol{u} = \begin{pmatrix} \dot{q} \\ \dot{m}_{in} \\ h_{in} \\ \dot{m}_{out} \end{pmatrix} \tag{39}$$

Where $\boldsymbol{y}$, $\boldsymbol{C}$ and $\boldsymbol{D}$ are the outputs vector, the output matrix and the throughput matrix.

To get an approximate linear state space equation of the non-LTI model about the operating point, the accumulator is linearised using *small signal* linearisation by a coordinate transformation to variation in parameters around the equilibrium point $\boldsymbol{x}^*$. The resulting coordinates are as follows:

$$\boldsymbol{\Delta x} = \boldsymbol{x} - \boldsymbol{x}^* \tag{40}$$

$$\boldsymbol{\Delta u} = \boldsymbol{u} - \boldsymbol{u}^* \tag{41}$$

$$\boldsymbol{\Delta y} = \boldsymbol{y} - \boldsymbol{h}(\boldsymbol{x}^*, \boldsymbol{u}^*) \tag{42}$$

The state space representation of the system in the neighbourhood of the equilibrium point is:

$$\boldsymbol{\Delta \dot{x}} = \boldsymbol{A\Delta x} + \boldsymbol{B\Delta u} \tag{43}$$

$$\boldsymbol{\Delta y} = \boldsymbol{C\Delta x} + \boldsymbol{D\Delta u} \tag{44}$$

The system matrix can be derived using a Jacobian as follows [64]:

$$\boldsymbol{A} = \begin{pmatrix} \frac{\partial f_1(t,x_1^*,\dots,x_n^*,u^*)}{\partial x_1} & \cdots & \frac{\partial f_1(t,x_1^*,\dots,x_n^*,u^*)}{\partial x_n} \\ \vdots & \ddots & \vdots \\ \frac{\partial f_n(t,x_1^*,\dots,x_n^*,u^*)}{\partial x_1} & \cdots & \frac{\partial f_n(t,x_1^*,\dots,x_n^*,u^*)}{\partial x_n} \end{pmatrix} \tag{45}$$

$$\boldsymbol{A} = \begin{pmatrix} \frac{\partial \dot{h}}{\partial h} & \frac{\partial \dot{h}}{\partial m} \\ \frac{\partial \dot{m}}{\partial h} & \frac{\partial \dot{m}}{\partial m} \end{pmatrix} \tag{46}$$

$$\boldsymbol{A} = \begin{pmatrix} \frac{-(\dot{m}_{in}-\dot{m}_{out})-\left(\frac{\partial h_l}{\partial h}\Big|_\rho\right)\dot{m}_{out}}{m} & \frac{(\dot{m}_{in}-\dot{m}_{out})+\left(\frac{\partial h_l}{\partial h}\Big|_\rho\right)\dot{m}_{out}}{m^2} \\ 0 & 0 \end{pmatrix} \tag{47}$$

The output matrix is given by:

$$\boldsymbol{B} = \begin{pmatrix} \frac{\partial f_1(t,x_1^*,\dots,x_n^*,u^*)}{\partial u_1} & \cdots & \frac{\partial f_1(t,x_1^*,\dots,x_n^*,u^*)}{\partial u_n} \\ \vdots & \ddots & \vdots \\ \frac{\partial f_n(t,x_1^*,\dots,x_n^*,u^*)}{\partial u_1} & \cdots & \frac{\partial f_n(t,x_1^*,\dots,x_n^*,u^*)}{\partial u_n} \end{pmatrix} \tag{48}$$

$$\boldsymbol{B} = \begin{pmatrix} \frac{\partial \dot{h}}{\partial \dot{q}} & \frac{\partial \dot{h}}{\partial h_{in}} & \frac{\partial \dot{h}}{\partial \dot{m}_{in}} & \frac{\partial \dot{h}}{\partial \dot{m}_{out}} \\ \frac{\partial \dot{m}}{\partial \dot{q}} & \frac{\partial \dot{m}}{\partial h_{in}} & \frac{\partial \dot{m}}{\partial \dot{m}_{in}} & \frac{\partial \dot{m}}{\partial \dot{m}_{out}} \end{pmatrix} \tag{49}$$

$$\boldsymbol{B} = \begin{pmatrix} \frac{1}{m} & \frac{\dot{m}_{in}}{m} & \frac{h_{in}-h}{m} & h - \left(\frac{\partial h_l}{\partial h}\Big|_\rho\right)h \\ 0 & 0 & 1 & -1 \end{pmatrix} \tag{50}$$

The dynamics of interest, from q to pressure are captured by the first column, the rest of the columns in the output matrix are for the disturbance inputs which include h_{in}, $\dot{m}_{in}$ and $\dot{m}_{out}$. Finally, for the algebraic output equation, since the loop of interest is from the heating or cooling action to pressure:

$$\boldsymbol{C} = \begin{pmatrix} \frac{\partial P}{\partial h}\Big|_\rho & \frac{\partial P}{\partial \rho}\Big|_h \frac{1}{V} \end{pmatrix} \tag{51}$$

The system in this case has no throughput.

$$\boldsymbol{D} = 0 \tag{52}$$

The conversion from the linearised state space equation is given by [64, 65]:

$$P(s) = \boldsymbol{C}(s\boldsymbol{I} - \boldsymbol{A})^{-1}\boldsymbol{B} + \boldsymbol{D} \tag{53}$$

$$\frac{\Delta P(s)}{\Delta H(s)} = \begin{pmatrix} \left.\frac{\partial P}{\partial h}\right|_{\rho} & \left.\frac{\partial P}{\partial \rho}\right|_{h}\frac{1}{V} \end{pmatrix} \times \begin{pmatrix} s + \frac{(\dot{m}_{in}-\dot{m}_{out})+\left(\left.\frac{\partial h_l}{\partial h}\right|_{\rho}\right)\dot{m}_{out}}{m} & \frac{(\dot{m}_{in}-\dot{m}_{out})+\left(\left.\frac{\partial h_l}{\partial h}\right|_{\rho}\right)\dot{m}_{out}}{m^2} \\ 0 & s \end{pmatrix}^{-1} \begin{pmatrix} \frac{1}{m} \\ 0 \end{pmatrix} + 0$$

$$P(s) = \frac{\Delta P(s)}{\Delta H(s)} = \frac{\frac{1}{\rho V}\left.\frac{\partial P}{\partial h}\right|_{\rho}}{\left(s + \frac{\dot{m}_{in}-\dot{m}_{out}\left(1-\left.\frac{\partial h_l}{\partial h}\right|_{\rho}\right)}{m}\right)} \text{ bar/kW} \tag{54}$$

The system can be written in a first-order form.

$$P(s) = \frac{A}{(s+\alpha)} \text{ ,where } A = \frac{1}{m}\left.\frac{\partial P}{\partial h}\right|_{\rho} \text{ and } \alpha = \frac{\dot{m}_{in}-\dot{m}_{out}\left(1-\left.\frac{\partial h_l}{\partial h}\right|_{\rho}\right)}{m} \tag{55}$$

The coefficient $\left.\frac{\partial P}{\partial h}\right|_{\rho}$ can be well approximated using numerical differentiation of the plot of pressure versus enthalpy along constant density lines in the two-phase region.

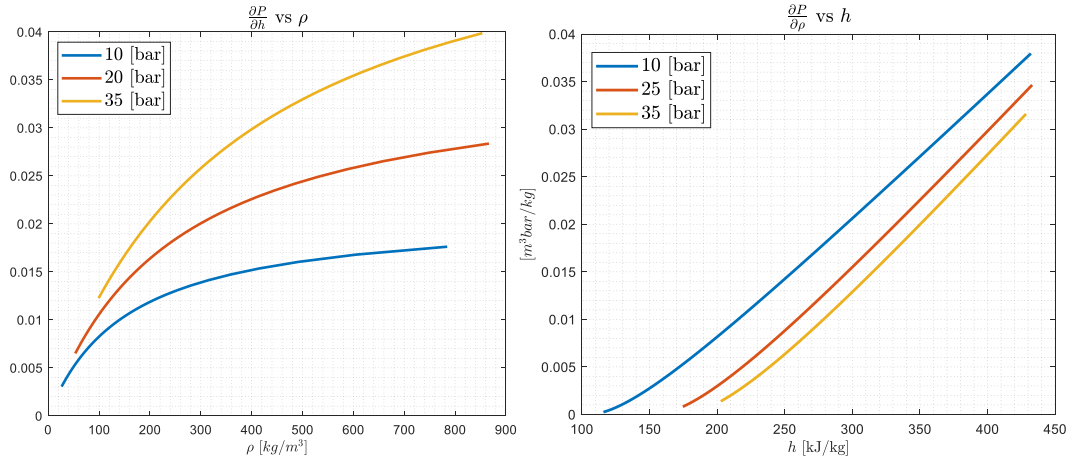

Figure 31: Sensitivity of Pressure to Specific Enthalpy [Generated using MATLAB REFPROP]

Equation 55 shows that the response from the heat input to the pressure of the accumulator is governed by a first-order response. The equation further shows that the system has uncertain gain (A) and corner frequency (α). The accumulator can momentarily have a right-hand pole during transients when the numerator coefficient is negative; however, it will always be closed-loop stable because of the high actuator gain and properly tuned controller. Finally, in flowthrough mode, the accumulator has feedback through specific enthalpy, which makes it go to a steady state when constant power is supplied. In other words, a power input increases the averaged specific enthalpy (h), which in turn increases the specific enthalpy of the saturated liquid (h_l) at the bottom of the accumulator. h_l increases until $m_{out}h_l$ balances out the heat input at a new pressure level.

Conversely, in non-flowthrough mode at a quasi-steady state if $\dot{m}_{in} = \dot{m}_{out} = 0$, the accumulator becomes an integrator with uncertain gain. What this means in practice is that the pressure will rise in a ramp until either the system enters the supercritical region, there is a

failure, or the accumulator is empty as long as the heat input is added to the system. Equation 55 also shows that the corner frequency of the specific enthalpy dynamics of the accumulator decreases with the increase in the CO_2 mass in the accumulator. Finally, the net mass inflow or outflow impacts both the corner frequency, gain, and even the stability of the accumulator. Figure 29 shows the forward loop of the accumulator pressure control by heating or cooling action.

The actuator for this process is the heat exchanger and heater. However, the actuator that is mainly active is the heat exchanger because the return mixture usually has a higher specific enthalpy than needed in flow-through mode, which requires constant cooling action. Secondly, the heater dynamics are much faster and can be approximated as an ideal step input. Therefore, the actuator that will be explored in detail is the heat exchanger. and the dynamics through the actuator are given by a First-Order Dead-Time model.

$$A(s) = \frac{k_a e^{-sT_d}}{\tau_a s+1} \tag{56}$$

$$k_a = k_{HX}(T_{CO2} - T_{R744}) \tag{57}$$

k_a,T_d, T_{R744} and T_{CO2} are the heat exchanger gain, delay, and temperatures of the CO_2 on the primary side and the accumulator temperatures, respectively. The heat characterisation data from the experiment conducted from the 13th to the 14th of October 2023 is shown in Figure 32 below. From this experiment, the capacity and transport delay may be calculated.

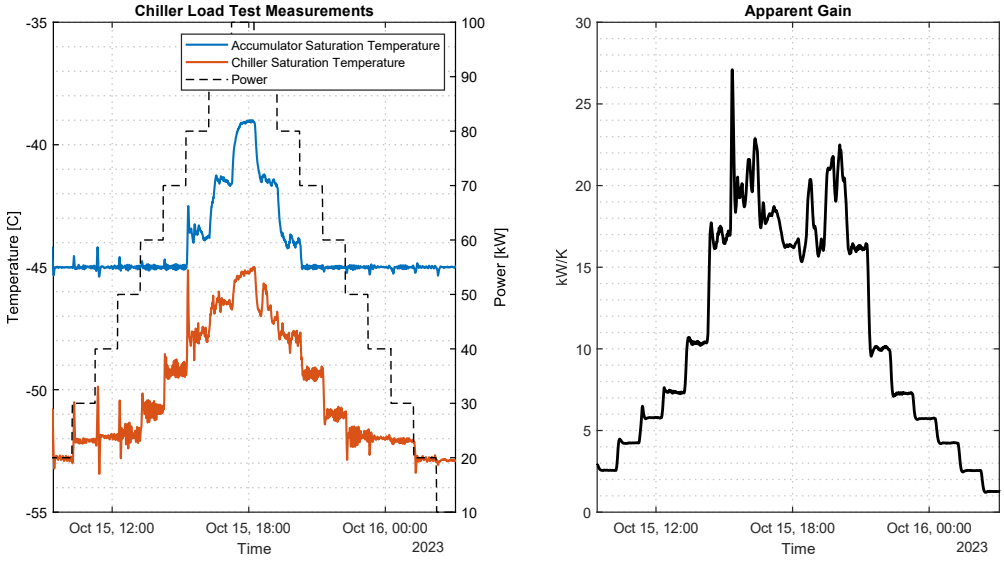

Figure 32: Heat Exchanger Data [Retrieved from Timber]

At the moment just before the accumulator drifts warm, the heat exchanger is delivering its maximum power (Q_{HX}) is equal to the power input (Q_{in}). This gives the capacity of the chiller, which is approximately 80 kW.

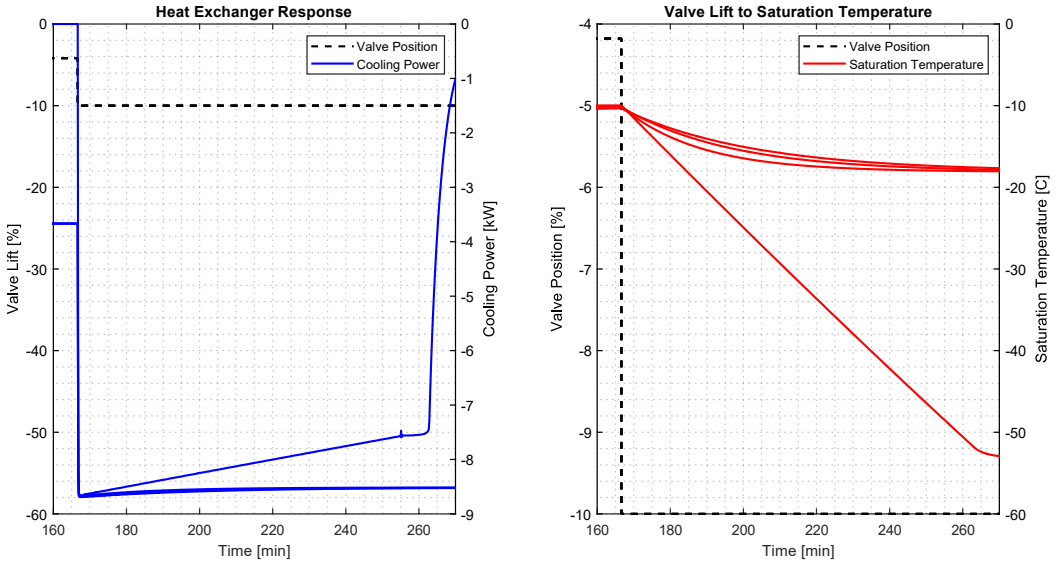

Figure 33: Actuator Responses

In addition, the cooling forward dynamics were also simulated, and the results are plotted in Figure 33. Here, the heat exchanger valve was stepped in for three accumulator levels 10%,50% and 80% in flow-through mode. The last step was done in non-flow-through mode. These tests confirm that the system is a pure integrator when $\dot{m}_{in} = \dot{m}_{out} = 0$. This case is represented by the saturation temperature ramping down to actuator saturation, which is consistent with integrator behaviour. There is a loss of cooling power when the actuator saturates. The simulations also revealed that the actuator has more bandwidth than the accumulator dynamics. The rest of the parameters were calculated from the simulation to be,

$T_d \approx 0.1$

$\tau_a \in [5,6]$

The resulting forward loop is from the reference (r) to the output pressure (y), while the rest of the inputs and outputs are disturbances to the system;

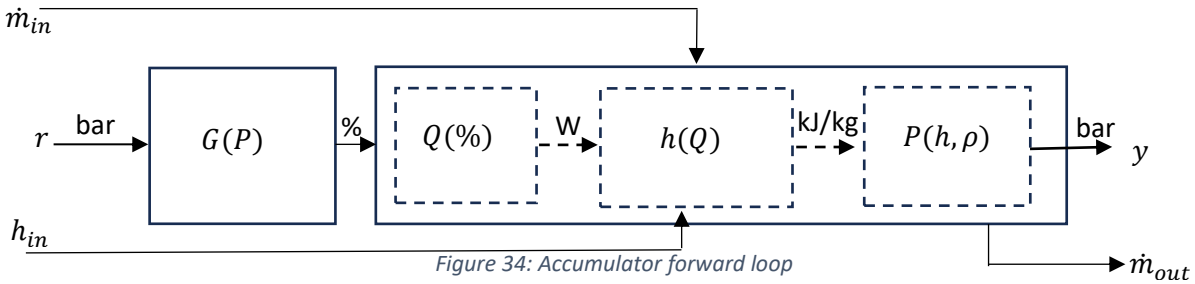

Figure 34: Accumulator forward loop

The forward loop shows that given a pressure reference, which in this case is coupled with the saturation temperature, the controller gives a percentage command which is the chiller valve opening percentage for the cooling action, or the heating power command as a percentage of the full capacity. This then changes the specific enthalpy of the accumulator, which results in a corresponding change in pressure at the operating average density.

BPR Temperature Control

The subzero requirement mentioned in 1.3.1 can be violated for short periods of time because the time constant for reverse annealing is in the time scale of several months. Bringing the detectors to room temperature for several weeks allows the detectors to benefit from beneficial annealing, with leakage current reduced substantially over a few days without significant loss in charge collection efficiency from reverse annealing [29]. The detector must be at sensibly warmer temperatures before being worked on. Consequently, the system must be capable of warm operation (0˚C-15˚C) while still minimising thermal gradients.

The accumulator is, however, limited by the restrictions for the energy that can be stored in a pressure vessel underground and cannot operate at pressures high enough for warm operation. Therefore, a mechanism to get the system even higher in pressure was needed, which is where the back-pressure regulator (BPR) comes in. The back pressure regulator enables the pump discharge pressure to drive the return line to pressures hence temperatures higher than the accumulator limit. This is achieved by throttling the BPR valve located just after the return of the transfer lines in Figure 16. Thus, the pressure upstream of the valve increases while the pressure after the valve is held at the accumulator pressure. A controller handover between the two control modes is implemented for a smooth handover between accumulator control and where the BPR takes over. Similar to the accumulator, the BPR will only be able to control the detector exit temperature if the returning working fluid is two-phase.

The BPR control mechanism is not that different from the accumulator. The main difference is that it uses the return line and detector volume together with the density to increase the pressure at saturation. This is achieved by changing the accumulation of mass in the return line by changing the BPR exit mass flow.

$$\frac{dm}{dt} = \dot{m}_{in} - \dot{m}_{out} \tag{58}$$

$$\frac{dm}{dt} = \dot{m}_{in} - c_v \phi \sqrt{(P_d - P_a)\rho} = \ f(\rho, \phi, P_a, P_d) \tag{59}$$

Once again, linearising the equation results in the following;

$$\frac{\partial f}{\partial m} = \frac{-c_v \phi_0 \left(\frac{\left(P_{d_0} - P_a\right)}{V} + \frac{m_0 \frac{\partial P_d}{\partial \rho}}{V^2} \right)}{2\sqrt{\left(P_{d_0} - P_a\right)\frac{m_0}{V}}} = \alpha \tag{60}$$

Linearising the input;

$$\frac{\partial f}{\partial u} = \frac{\partial f}{\partial \phi} = -c_v \sqrt{\left(P_{d_0} - P_a\right)\frac{m_0}{V}} = b \tag{61}$$

The output equation becomes $P_d = g(h, \rho) = P_d(h, \rho)$

$$\frac{\partial g}{\partial m} = \frac{1}{V}\frac{\partial P_d}{\partial \rho} = c \tag{62}$$

$$\frac{\Delta P_d(s)}{\Delta \phi(s)} = \frac{bc}{s - \alpha} \tag{63}$$

V is the volume from the inlet of the BPR to that of the detector. The system is open loop stable because $P_d > P_a$ during operation, and the system will be a pure integrator for $\phi_0 = 0$. The negative sign of the gain comes from the fact that an increase in the valve lift decreases the pressure and vice versa. However, because the *sense* of the controller can be changed in the UNICOS framework, the negative gain can be disregarded for controller design. Finally, by plugging in the values for the bounding operational cases in nominal conditions, the pressure dynamics have a much higher bandwidth than the actuator. This means the *dominant mode* with the limiting dynamics is that of the valve.

$$\alpha \gg \frac{1}{\tau} \tag{64}$$

Since in this case $|\alpha| > \frac{5}{\tau}$, order reduction was used to do QFT for the actuator with some gain from the reduced pole.

$$\frac{\Delta P_d(s)}{\Delta \phi(s)} = \frac{A}{(\tau s+1)} \text{ bar/\%, A} = \frac{\frac{2}{V}\frac{\partial P_d}{\partial \rho}(P_{d_0} - P_{a_0})\frac{m_0}{V}}{\phi_0\left(\frac{(P_{d_0} - P_{a_0})}{V} + \frac{m_0}{V^2}\frac{\partial P_d}{\partial \rho}\right)} \tag{65}$$

$(P_d - P_a) \in [0.3,16]$ bar

The $\frac{\partial P_d}{\partial \rho}|_h$ is retrieved from using REFPROP, in which properties are calculated in single-phase formulations and weighted by vapour quality, as illustrated below [66, 67].

$$\hat{x} = \frac{\hat{h} - h_l}{h_v - h_l} \tag{66}$$

$\hat{x}$, $\hat{h}$,h_l, and h_v are the averaged vapour quality, averaged specific enthalpy, specific enthalpy of liquid fraction, and specific enthalpy of the vapour fraction, respectively.

$$h_{vl} = h_v - h_l \tag{67}$$

$$\frac{\partial T}{\partial P} = \frac{T(v_v - v_l)}{h_{vl}} \tag{68}$$

v_v and v_l are the specific volumes of vapour fraction and liquid fraction, respectively.

Where $v_v = \frac{1}{\rho_v}$ and $v_l = \frac{1}{\rho_l}$.

$$\frac{\partial h_v}{\partial P} = v_v(1 - \beta T) + c_{pv}\left(\frac{\partial T}{\partial P}\right) \tag{69}$$

$$\frac{\partial h_l}{\partial P} = v_l(1 - \beta T) + c_{pl}\left(\frac{\partial T}{\partial P}\right) \tag{70}$$

β is the volume expansivity and $c_p$is the isobaric heat capacity.

$$\frac{d\hat{x}}{dP} = \frac{\hat{x}\left(\frac{\partial h_v}{\partial P}\right) + (1 - \hat{x})\left(\frac{\partial h_l}{\partial P}\right)}{-h_{vl}} \tag{71}$$

Then the derivatives of specific volumes with respect to pressure are calculated thus.

$$\frac{\partial v_l}{\partial P} = \beta_l v_l\left(\frac{\partial T}{\partial P}\right) \tag{72}$$

$$\frac{\partial v_v}{\partial P} = \beta_v v_v\left(\frac{\partial T}{\partial P}\right) \tag{73}$$

The penultimate step calculates the vapour quality weighted partial derivative of a specific volume with respect to pressure.

$$\frac{\partial v}{\partial P} = \frac{\partial v_l}{\partial P} + \left(\frac{d\hat{x}}{dP}\right)(v_v - v_l) + \hat{x}\left(\frac{\partial v_v}{\partial P} - \frac{\partial v_l}{\partial P}\right) \tag{75}$$

$$\frac{\partial \rho}{\partial P} = -\rho^2\left(\frac{\partial v}{\partial P}\right) \tag{76}$$

$$\frac{\partial P}{\partial \rho} = -\frac{1}{\rho^2}\left(\frac{\partial P}{\partial v}\right) \tag{77}$$

The result is plotted against specific enthalpy in the two-phase dome for the three pressure levels, which include the boundaries – 35 and 70 bars – in Figure 35. It shows that as the specific enthalpy increases, the sensitivity of pressure due to changes in density decreases; this is because the compressibility of the fluid increases. Overall, the derivative also increases with increasing baseline pressure because an already compressed two-phase mixture is less compressible than one that is not.

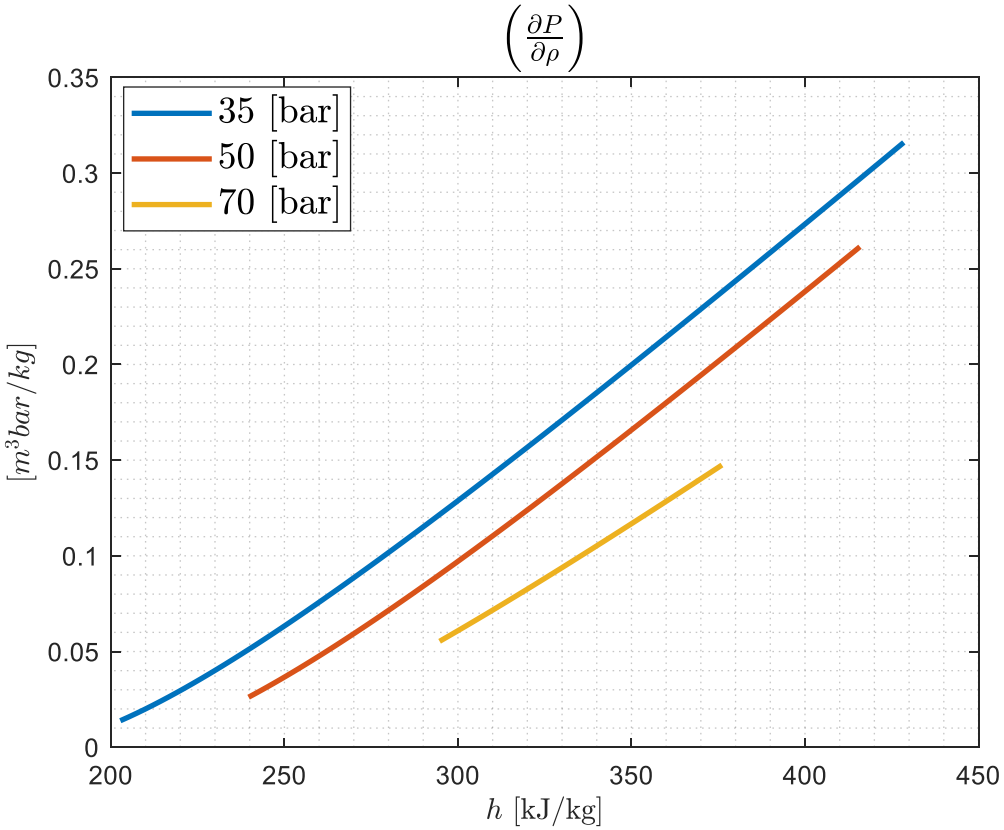

Figure 35: Sensitivity of Pressure Density Changes [Generated using MATLAB REFPROP]

All in all, when P_{d_0} tends to P_a, which occurs when the BPR is fully open, and the loop gain is the lowest. Conversely, when the valve is fully closed, the response is dominated by integrating behaviour. The rated valve opening time is 3 seconds. However, a test revealed that this parameter was uncertain and could go as high as 11 seconds. Hence, the actuator dynamics will be modelled as an uncertain first-order system.

$A \in [0.04, 2.07]$ Bar/%

$\tau \in [0.6, 2.2]$ s

The full opening time is assumed to approximate 5-time constants using first order modelling.

4.7.3 Detector Differential Pressure Control

The remaining pressure control feedback loops, which, much like the BPR control, can be designed using the same procedure.

5.Quantitative Feedback Theory Design

> Not everything that can be counted counts, and not everything that counts can be counted.
>
> – *Albert Einstein*

Real-world processes, such as the pressure and temperature control discussed in this work, are often inherently non-linear and can display both structured and unstructured uncertainties. This complexity necessitates the design of a controller that accounts for these uncertainties and any sampling effects if the system is periodically sampled. By employing robust control design, controllers that mitigate uncertainty while ensuring the stability of the plant across its entire operational range can be designed. The above can be achieved using the Inverse Nichols Chart loop shaping in Quantitative Feedback Theory.

The Inverse Nichols Chart Loop-shaping design employed in this research is similar to the traditional Nichols Chart Loop-shaping approach. The primary distinction is that it inherently focuses on designing for sensitivity (S) instead of the complementary sensitivity (T), which is the case in the Nichols plot. Nonetheless, it remains feasible to incorporate the boundaries of T into the design, as is the case in this dissertation, allowing for performance, sensitivity, and sampling effects to be effectively designed simultaneously, which is often not the case with other simpler PID tuning methods. Important metrics such as gain and phase margins can also be read off the chart. On the other hand, H-infinity was not used because the highly structured parameter uncertainty. Another complicated method which is outside the scope of this research is μ – synthesis. The major drawback with these methods is that they do not provide as much engineering insight during the design stage and can often result in high order controllers which need order reduction for implementation. The disadvantage of the Inverse Nichols Chart design is that frequencies are not explicitly labelled, and it can be difficult to read. The Figure 36 below shows that the Inverse Nichols Chart is a contour map where if the open-loop curve of a system is plotted using open-loop phase (x-axis) and magnitude (y-axis) coordinate pairs, the corresponding closed-loop sensitivity behaviour can be read directly from the contour lines without requiring additional calculations. The figure below presents a 3D Inverse Nichols Chart, which works in a manner that is analogous to the Nichols Chart.

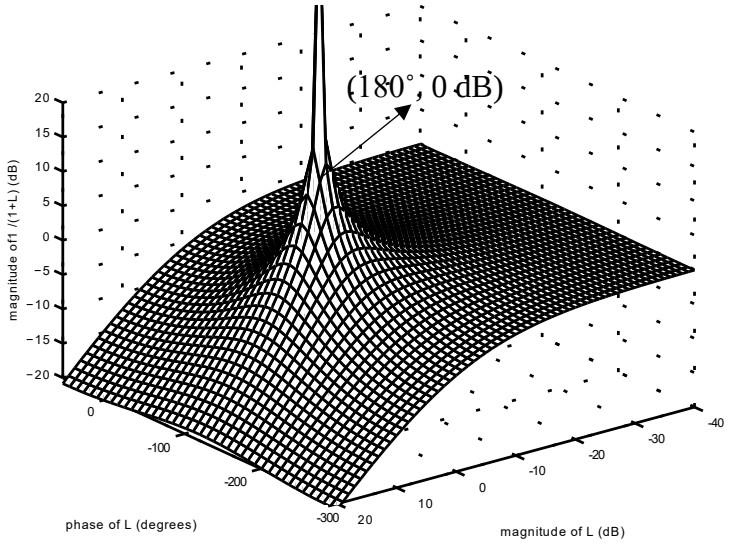

Figure 36: Inverse Nichols Chart [68]

5.1 Accumulator

The accumulator is an uncertain first-order system that may momentarily have a right-hand pole during transients when the numerator of α in the equation is negative. However, the RHS pole will always be close to the origin because α has a small magnitude, this means a sufficiently high actuator gain will maintain stability in this case as well because the high-frequency gain always has the same sign. The accumulator will be a pure integrator when the system is operating in non-flowthrough mode. The feedback loop has fast actuator dynamics for heating and slower actuator dynamics for cooling and the sensor dynamics are relatively fast compared to the closed loop bandwidth.

5.1.1 Specifications

In order to conduct robust controller design that takes into account sampling effects, the design will be carried out in the digital domain (w). The change of base from the continuous Laplace domain (s) is given by the following approximation [69].

$$P_d(w) \approx P_c(s)\left(1 - \frac{T_s}{2}w\right)\Big|_{s=w} \tag{74}$$

Where P_c, P_d, and T_s are the continuous plant transfer function, the digital (sampled) transfer function and the sampling period T_s. PLCs used for Demo have a sampling time ranging between 20 ms and 100 ms. The worst case will be used for this design. This approximation is accurate to the order $\mathcal{O}(T^2)$, provided the sampling period is much smaller than the *mode* that has the highest *residual*. For the accumulator;

$$P(w)A(w) = \frac{k_a e^{-wT_d}}{\tau_a w+1}\frac{A}{(w+\alpha)}\text{, where } A = \frac{1}{\rho V}\frac{\partial P}{\partial h}\Big|_\rho \text{ and } \alpha = \frac{\dot{m}_{in} - \dot{m}_{out}\left(1 - \frac{\partial h_l}{\partial h}\Big|_\rho\right)}{\rho V} \tag{75}$$

$A \in [5.1 \times 10^{-7}, 1.5 \times 10^{-5}]$ bar/kW

$\alpha \in [-0.0011, 0.0156]$

$T_d \in [0.1, 0.3]$

$\tau_a \in [5, 6]$

$k_a \approx 19\ kW/K$

The following frequency domain specifications were drawn up to meet the desired time domain behaviour;

1. $\left|\frac{1}{1+L}\right| \leq -20$ @ $0.001\ rads^{-1}$ (Attenuate output disturbance by 0.1)
2. $\left|\frac{1}{1+L}\right| \leq 3dB\ \forall\ \omega$ (Sensitivity: Attenuate closed-loop plant uncertainty to below 3 dB for all frequencies)
3. $\left|\frac{L}{1+L}\right| \leq 3dB\ \forall\ \omega$ (Performance: Keep the closed-loop gain below 3 dB at all frequencies for fast response and acceptable overshoot.)
4. $\lim_{s\to 0}|L| = \infty$ (Track with zero steady-state error.)

The MATLAB QFT Toolbox was used to conduct this design. First, the `ndgrid()` function is used to create a matrix of combinations of different uncertain parameters. This ensures that the bounding (corner) cases are included, which is especially important for robust design. The next step is to draw the plant templates of the nominal plant at different frequencies. The accumulator loop may be gain-scheduled to guarantee maximum performance while upholding robust stability. In this case, the scheduling is done by accumulator density, as shown in Figure 37 below.

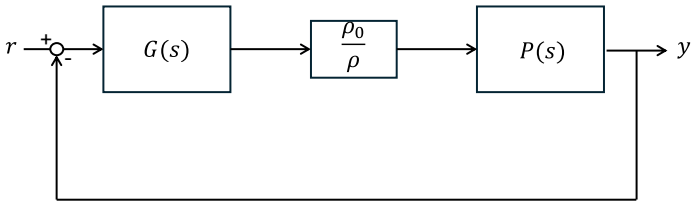

Figure 37: Gain scheduled Two Degree of Freedom (2-DOF) Feeback block diagram

In practice, with proper scaling, the scheduling can be done using the level which is readily available because in a homogeneous model;

$$\rho \approx \frac{\ell A \rho_l}{V}$$

This scheme effectively allows for the design of a controller using one fixed-gain plant, which is corrected by the gain schedule block. This correcting is what captures the uncertainty. Gain scheduling effectively shrinks the templates, hence the robust sensitivity and stability boundaries for each schedule set, as depicted by Figure 38. The scheduled design has a lower magnitude variation.

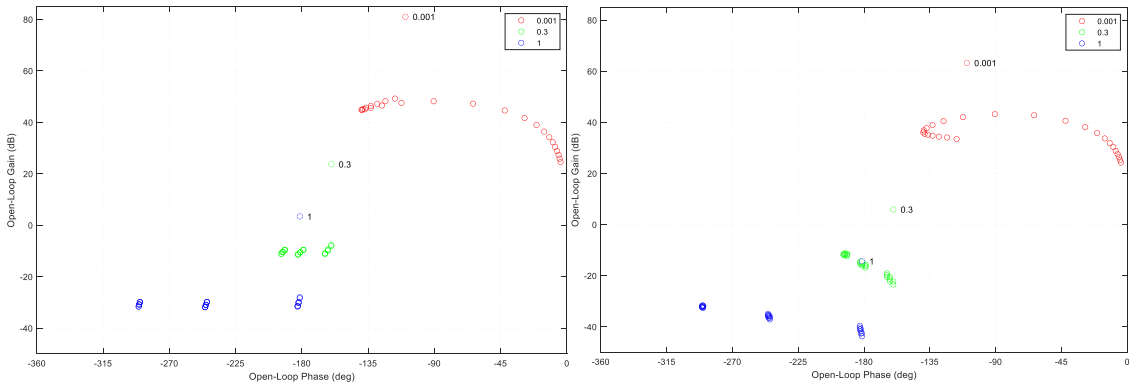

Figure 38: Nominal Plant Templates (non-gain scheduled left, gain scheduled right)

Then, these templates are used to draw the specification boundaries, as shown below. What makes QFT a powerful tool is that the nominal plant is arbitrarily chosen in the set of uncertain plant cases and only serves as a placeholder. If a proper design is achieved for this one plant case, it is guaranteed that all other plant cases bounded by the *corner cases* will be both stable and adhere to the imposed sensitivity specifications. The construction of the specification boundaries begins with the low-frequency specifications for sensitivity and output disturbance rejection, specification 1. This boundary – drawn as a red curved closed-loop magnitude curve - means disturbances at or below this frequency will be attenuated by a factor of 10 or more respectively; this is also the case for the effects of plant uncertainty at this frequency.

Specifications 2 and 3 centre on sensitivity (S), robust stability and complementary sensitivity (T). It is worth noting that while an inverse Nichols Chart has been chosen to carry out this design to deal with plant uncertainty, the bounds of T have also been included to guarantee robust stability in the input-output dynamics. The templates for the nominal plant at the remaining frequencies are then used to draw robust stability and sensitivity boundaries. The boundaries mark the region where robust stability is guaranteed for all plant cases and minimal overshoot for the high-gain plant case. The bottom line is that the two lowest frequencies (0.001 rads and 0.05 rads) must be on or above their respective boundaries (shown by matching colours). Similarly, all the remaining frequencies must be outside their respective boundaries and cannot go around the left-hand side. The resulting boundaries are shown in Figure 39. The figure corroborates the fact that gain scheduling shrinks the specification boundaries, which helps the loop-shaping process.

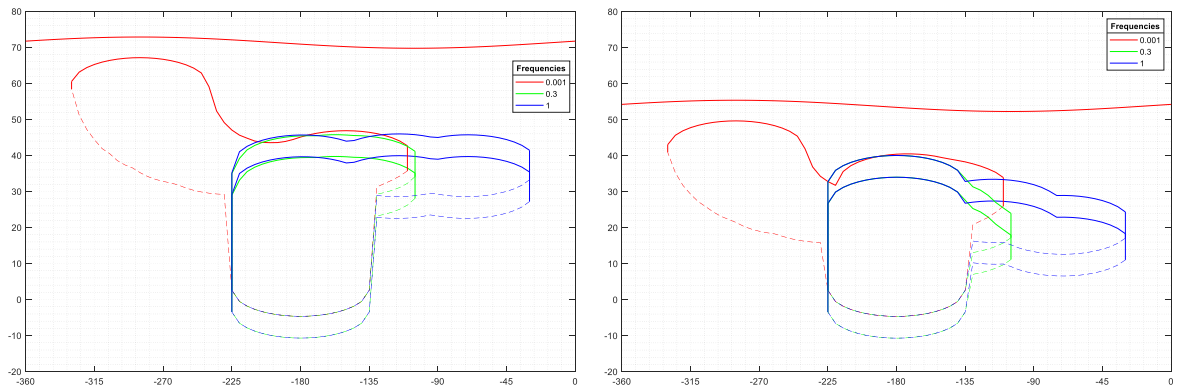

Figure 39: Combined Sensitivity and Performance Boundaries (non-gain scheduled left, gain scheduled right)

5.1.2 Design

The nominal plant needs infinite gain at low frequencies to guarantee zero steady-state error. This gain also ensures that specifications 1 and 4 are met and are achieved by means of an integrator in the controller. The plant sensitivity improves substantially, as shown by the two low frequencies clearing their boundaries. However, the system now violates the robust stability specification. In this case, some plant cases may be unstable, while others will have oscillatory responses because the system needs phase lead. The final step is to add a lead term (a real zero). This pushes all frequencies outside the robust stability boundaries, and the system now meets all specifications. Some overdesign is seen, with sensitivity for the low frequencies even lower than what was specified. This is tolerable as it means that the system will attenuate disturbances and plant uncertainties more aggressively at low frequencies.

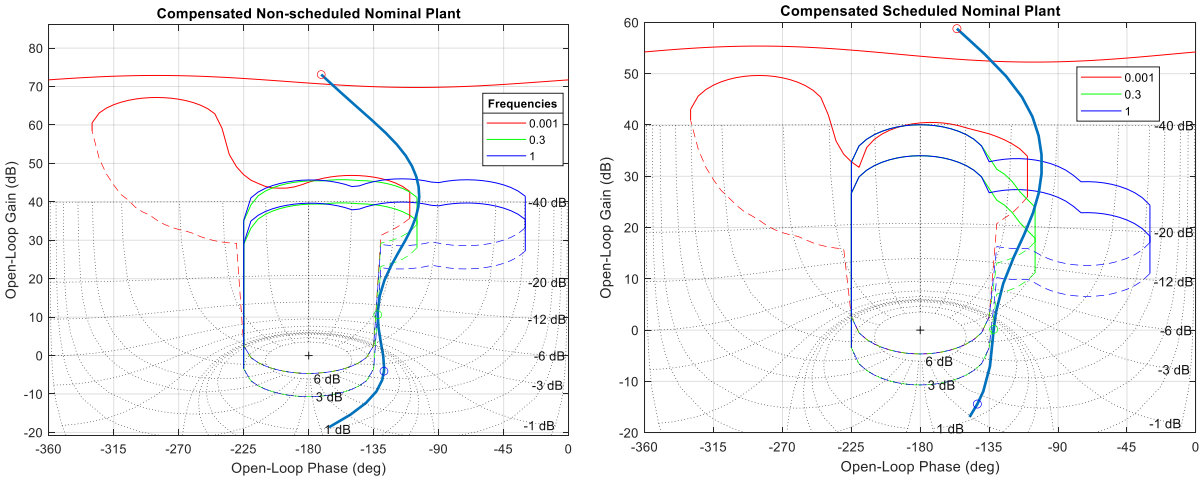

Figure 40: Plot of the final Compensated Nominal Plant [Generated in MATLAB]

The Inverse Nichols plot in Figure 40 only shows half of the curve, and a full picture can be shown by the Nyquist plot. Figure 41 below is a Nyquist plot with a logarithmic frequency scale [70], and plant cases from the three distinct categories have been sampled. The Nyquist Stability Criterion can be used to illustrate that due to sufficient actuator gain and a properly tuned controller, the system is stabilised for all cases elaborated below. The Criterion states that the number of closed-loop right-hand-side (positive and unstable) poles is equal to the sum of the number of clockwise encirclements of the point (-1,0) by the Nyquist curve and the number of open-loop right-hand-side (positive and unstable) poles. The criterion can be summarised by the equation;

$$P_{CL} = N_{CW} + P_{OL} \tag{83}$$

Where P_{CL}, N_{CW} and P_{OL} are the closed-loop right-hand-side poles, closed-loop right-hand-side poles and the open-loop right-hand-side poles, respectively. The pure integrator case plot encloses the entire right-hand plane (i.e. goes from $-j\infty \; to \; j\infty$ and crosses the real axis at $+\infty$). The spiralling at the origin is a consequence of the actuator transport delay, which results in an unbounded roll-off of phase.

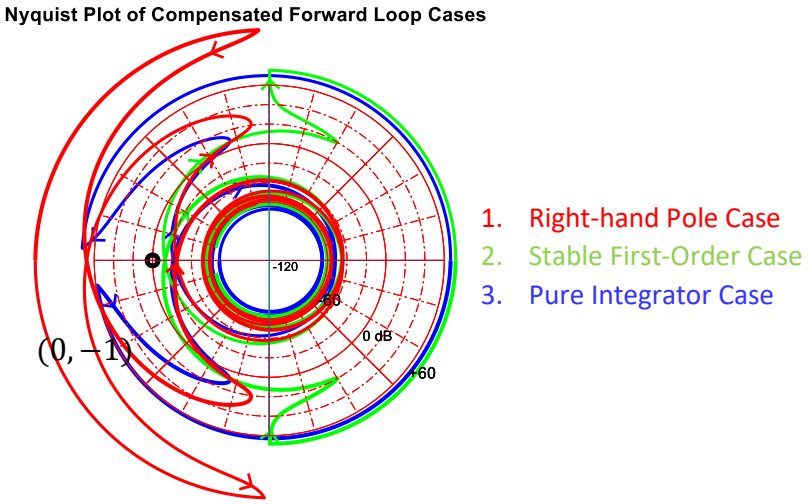

Figure 41: Logarithmic Nyquist Plot of Compensated Plants [Generated in MATLAB]

The resulting closed loop is stable for all cases, and sensitivity to variation in the plant dynamics will be attenuated as specified in the frequency domain specifications. The open-loop case with a right-hand pole, in red, encircles $(0, -1)$ counterclockwise once, as depicted by the Nyquist plot in Figure 41 [70], which means $P_{CL} = 0$ for all plants. The actuator transport delay results in an unbounded roll-off in phase, which results in the encirclements of the origin.

The process of loop shaping is now completed, and the resulting PID controller is;

$$G(w) = K_p\left(\frac{w+1/T_i}{w}\right)\left(\frac{T_d w+1}{\alpha T_d w+1}\right),\ \alpha = \frac{1}{T_{ds}} \tag{76}$$

The parallel equivalent of the interacting filtered PID controller above used in the UNICOS framework is;

$$G(w) = K_c\left(1 + \frac{1}{T_i w} + \frac{T_d w}{\alpha T_d w+1}\right),\ \alpha = \frac{1}{T_{ds}} \tag{77}$$

The resulting parameters for the non-scheduled controller are;

$$Kc = 19.2, T_i = 143.9, T_d = 0.5 \text{ and } \alpha = 0.5$$

The parameters of the scheduled scheme are as follows;

$$Kc' = 1.0, T_i' = 143.9\ T_d' = 0.5 \text{ and } \alpha' = 0.4$$

The primes indicate that these are parameters before the gain is scaled by the scheduling parameter – the density in this case. Figure 42 shows the step responses of the accumulator in a closed loop at the corner cases of operation. The negative sign for the output on the right means the cooling action by the heat exchanger, while the positive range is the heating action by the accumulator heater. For the scheduled system, the fastest possible responses result from the low-gain (sluggish) cases while maintaining stability for the high-gain (fast) cases, as seen on the left. The unscheduled system has slower responses because both high-gain cases and low-gain cases have the same parameters.

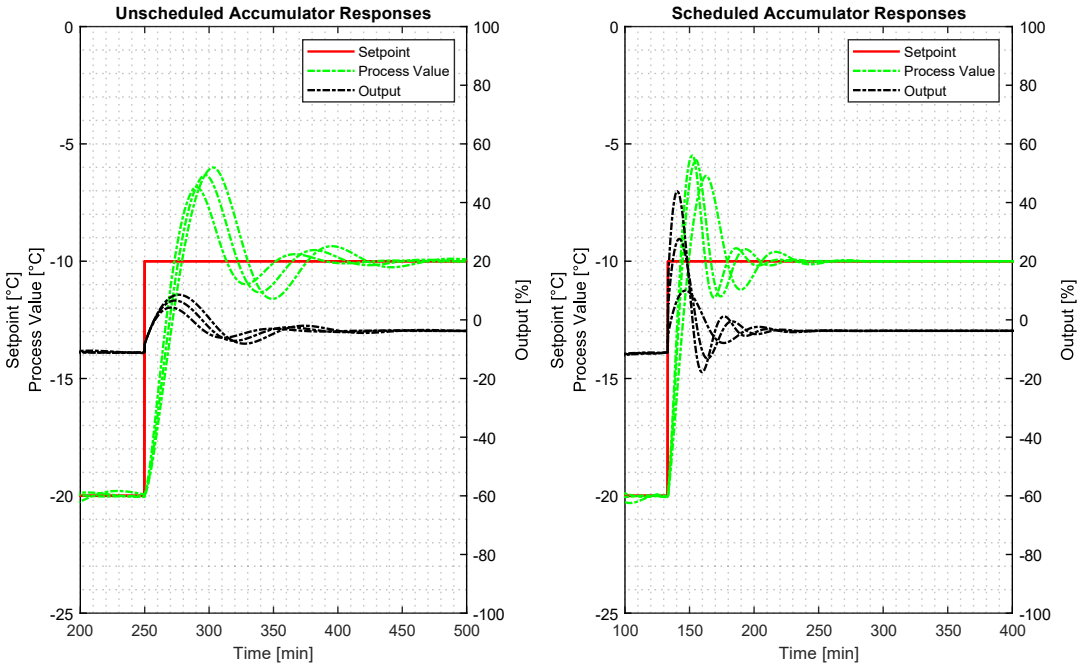

Figure 42: Compensated Accumulator Responses [Generated in EcosimPro]

Figure 43 below is the comparison of the controller in the Demo and that resulting from the non-scheduled QFT design. It shows that the low-frequency behaviour is largely similar, with differences at higher frequencies because of the lead-lag term. The oscillatory behaviour results from the fact that the design was primarily for sensitivity $(1/(1+L))$, whereas the step responses are for the complementary sensitivity $(L/(1+L))$. However, in Demo, the setpoints are rate-limited to one unit per minute, which will ensure that these high-frequencies are not excited, reducing overshoot during setpoint changes.

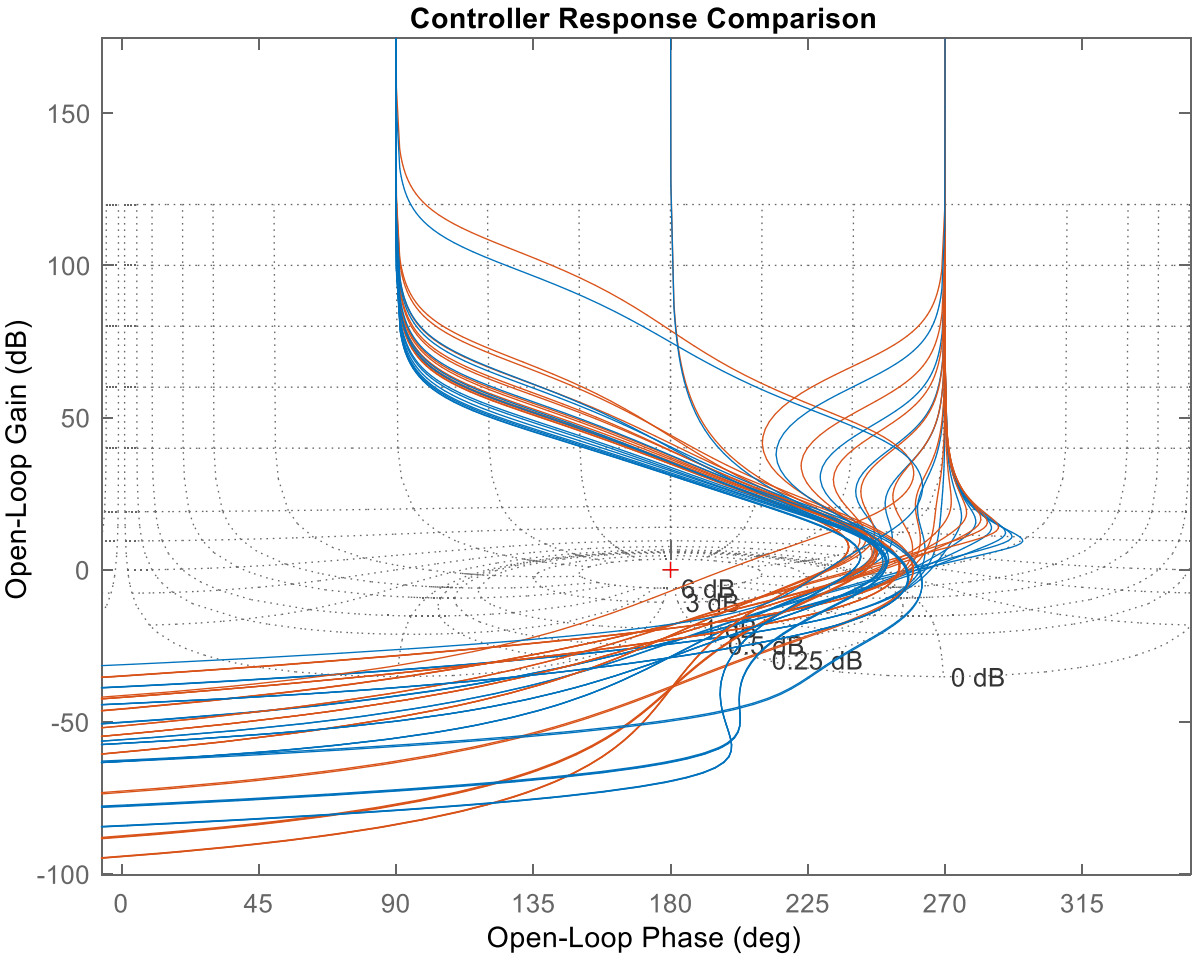

Figure 43: Controller Response Comparison

5.2 Back pressure regulator

In the case of the BPR at the nominal pump flow (1.5 kg/s), the return line and, hence, the detector exit pressure go as fast as the valve dynamics with some gain. Once again, to account for sampling effects, digital design is conducted in the *w* domain. So, from the transfer function for the BPR in 4.7.2;

$$P_d(w) = \frac{A(1-Tw/2)}{(\tau w+1)}\Big|_{T_s=0.01} \text{ bar/\%, A} = \frac{\frac{2}{V}\frac{\partial P_d}{\partial \rho}(P_{d_0}-P_{a_0})\frac{m_0}{V}}{\phi_0\left(\frac{(P_{d_0}-P_{a_0})}{V}+\frac{m_0}{V^2}\frac{\partial P_d}{\partial \rho}\right)} \tag{78}$$

5.2.1 Specifications

The following frequency domain specifications were drawn to meet the desired time domain behaviour;

1. $\left|\frac{1}{1+L}\right| \leq -20$ @ $0.01\ rads^{-1}$ (Attenuate output disturbance by 0.1)
2. $\left|\frac{1}{1+L}\right| \leq 3dB\ \forall\ \omega$ (Sensitivity: Attenuate plant uncertainty to below 3dB for all frequencies)

3. $\left|\frac{L}{1+L}\right| \leq 3dB \; \forall \; \omega$ (Performance: Keep the closed-loop gain below 3dB at all frequencies for fast response and minimal overshoot.)
4. $\lim_{s\to 0}|L| = \infty$ (Track with zero steady-state error.)

The MATLAB QFT Toolbox was used to conduct this design. First, the `ndgrid()` method is used to create a matrix of combinations of different uncertain parameters. This ensures that the bounding cases in the uncertainty space are included in the design.

5.2.2 Design

Once again, similar to the accumulator design, the design starts with the drawing of templates shown in Figure 44. These are then used to draw specification boundaries, which are included in the design in Figure 45.

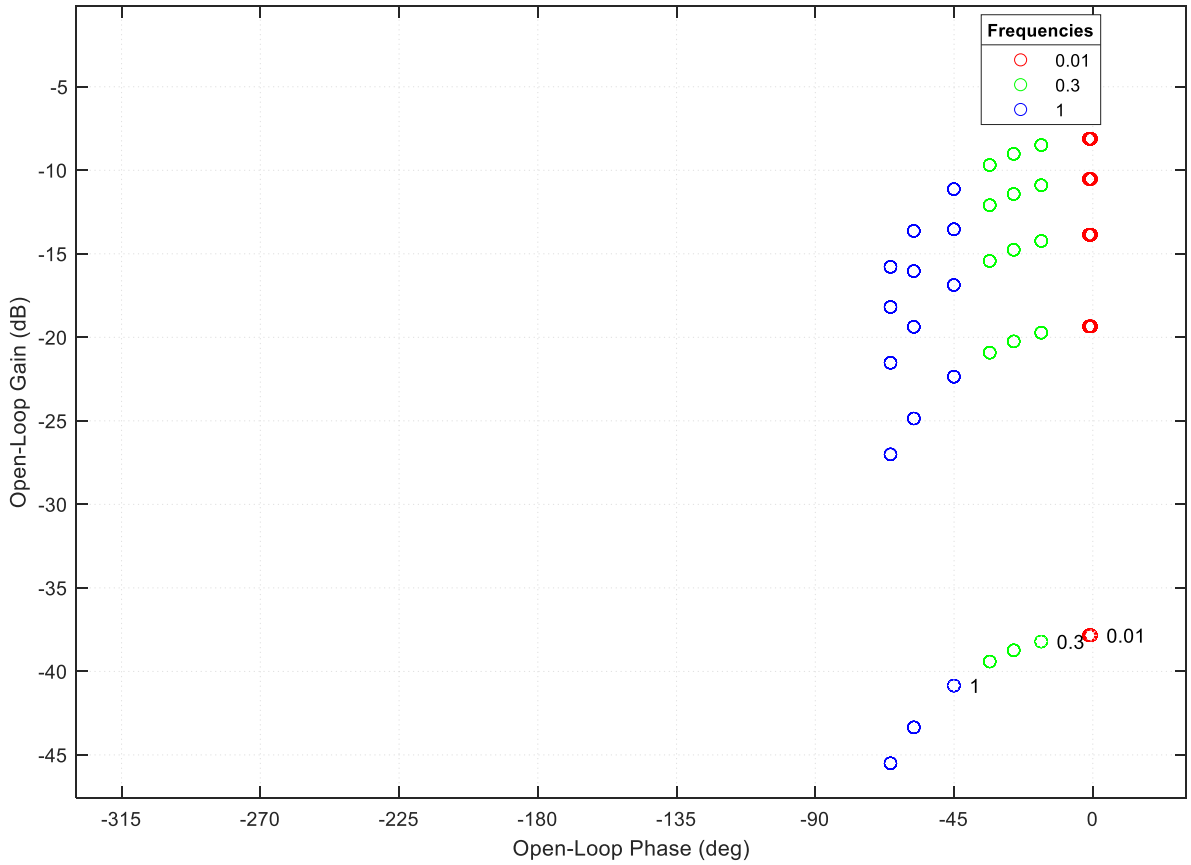

Figure 44: Nominal Plant Templates (non-gain scheduled left, gain scheduled right)

When the valve is near closed and the dynamics are dominated by integrating behaviour, the system inherently meets the 4th specification because the integrator has infinite gain at low frequency. However, an integrator was added to improve roll-off behaviour.

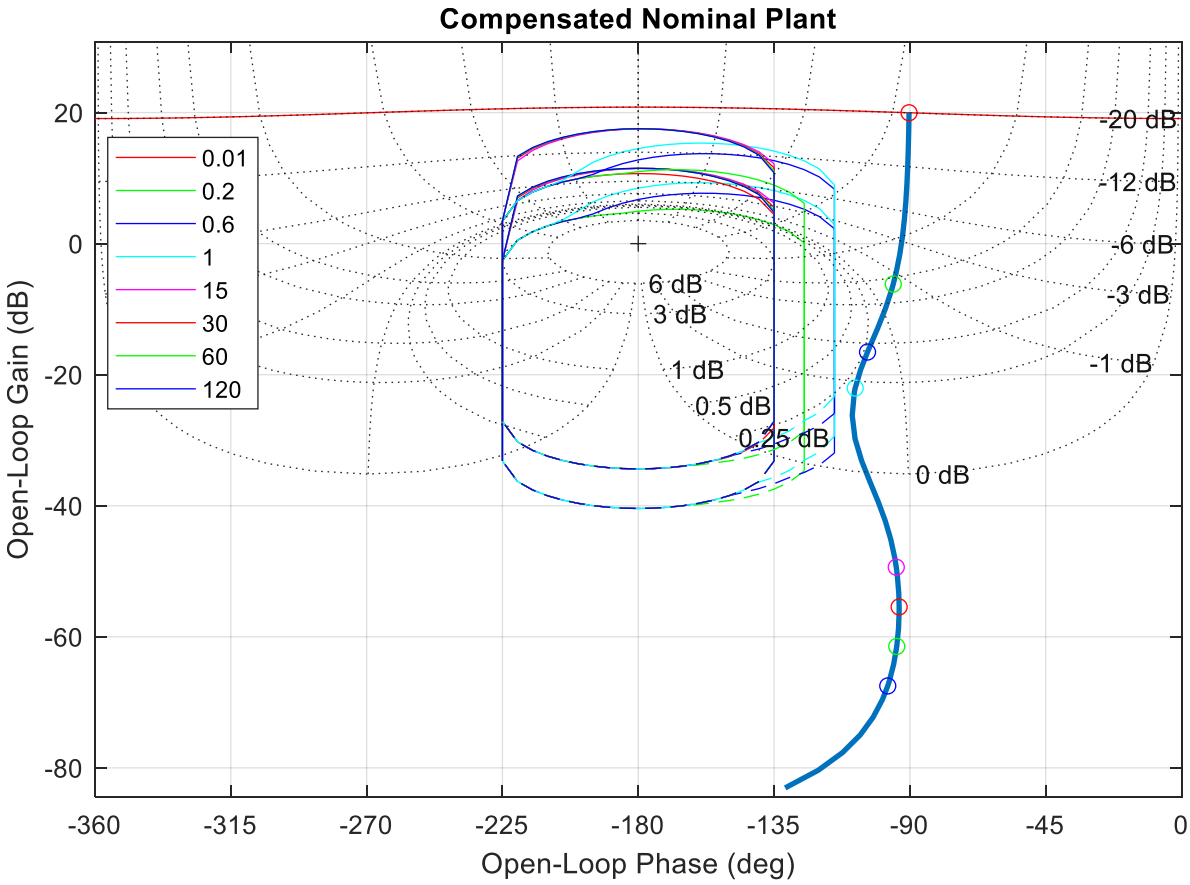

Figure 45: Plot of final compensated Nominal Plant [Generated in MATLAB)

The resulting interacting PI controller with a filtered derivative action is

$$G(w) = K_p\left(\frac{w+1/T_i}{w}\right)$$

The equivalent ideal PI used by the UNICOS frameworks is given by;

$$G(w) = K_c\left(1 + \frac{1}{T_i w}\right)$$

Where $K_p = 7.8$ and $T_i = 0.5$

Figure 46 shows the closed loop responses with the valve position on the right axis and the setpoint and process value on the left. The closed-loop step responses in Figure 46 shows that the system is stable in closed-loop for different values of ϕ_0,$P_{a_0}$and P_{d_0}. Furthermore, the controllers in UNICOS have an anti-windup scheme, as shown by the fact that the controllers exited saturation immediately when the error sign changed. Once again, just as in the accumulator loop, during operation, the rate limit will limit the excitation of high frequencies in the complementary sensitivity $(L/(1+L))$ seen in the step response, which results from the design being primarily for sensitivity.

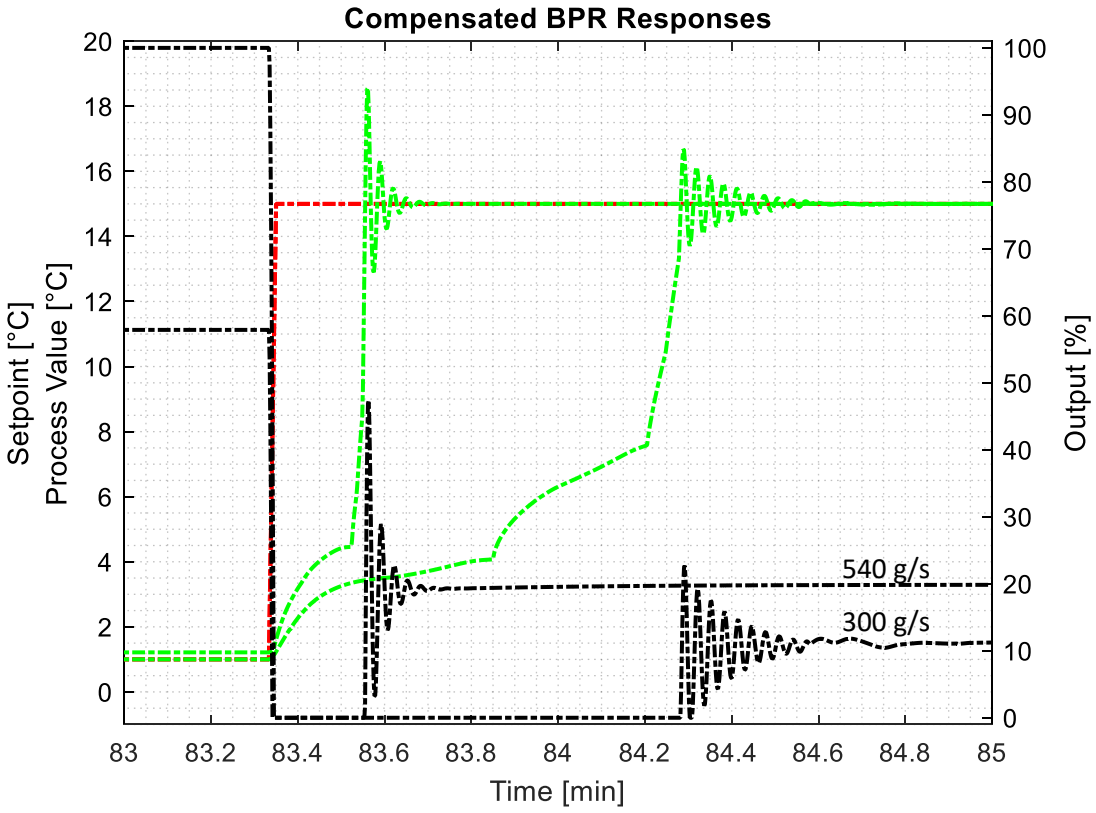

Figure 46: Compensated BPR Responses [Generated in EcosimPro]

The inverse Nichols plot in Figure 47 below is the frequency domain comparison of the sample PI parameters used in Demo ($K_p = 2$ and $T_i = 30$) and which results from QFT design.

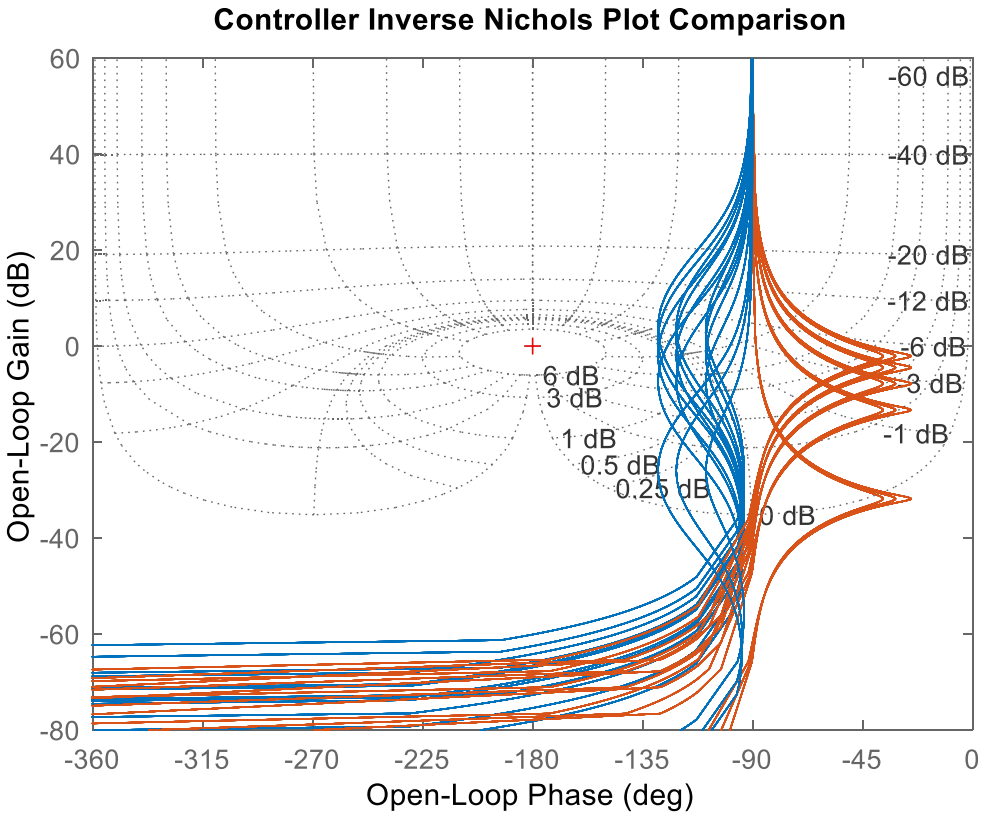

Figure 47: Comparison of Demo and QFT Controller (Generated in MATLAB)

6.Results and Analysis

"The signal is the truth. The noise is what distracts us."

– Nate Silver

6.1 Data Acquisition

The PLC that controls Demo mentioned above are connected to CERN's WinCCOA Supervisory Control and Data Acquisition (SCADA), which was used to operate and monitor Demo through the Remote Operator Gateway (ROG). The SCADA panels for Demo are shown below. Measurements from transmitters on various field objects were temporarily stored on ROG and archived on Timber for later retrieval; the archiving was lossy, as discussed below. Furthermore, an Electronic Logbook (Elog) was kept, describing how the experiments were conducted and objectives. The Elog also documents the general status of the Demo, including replacement and addition of components and more.

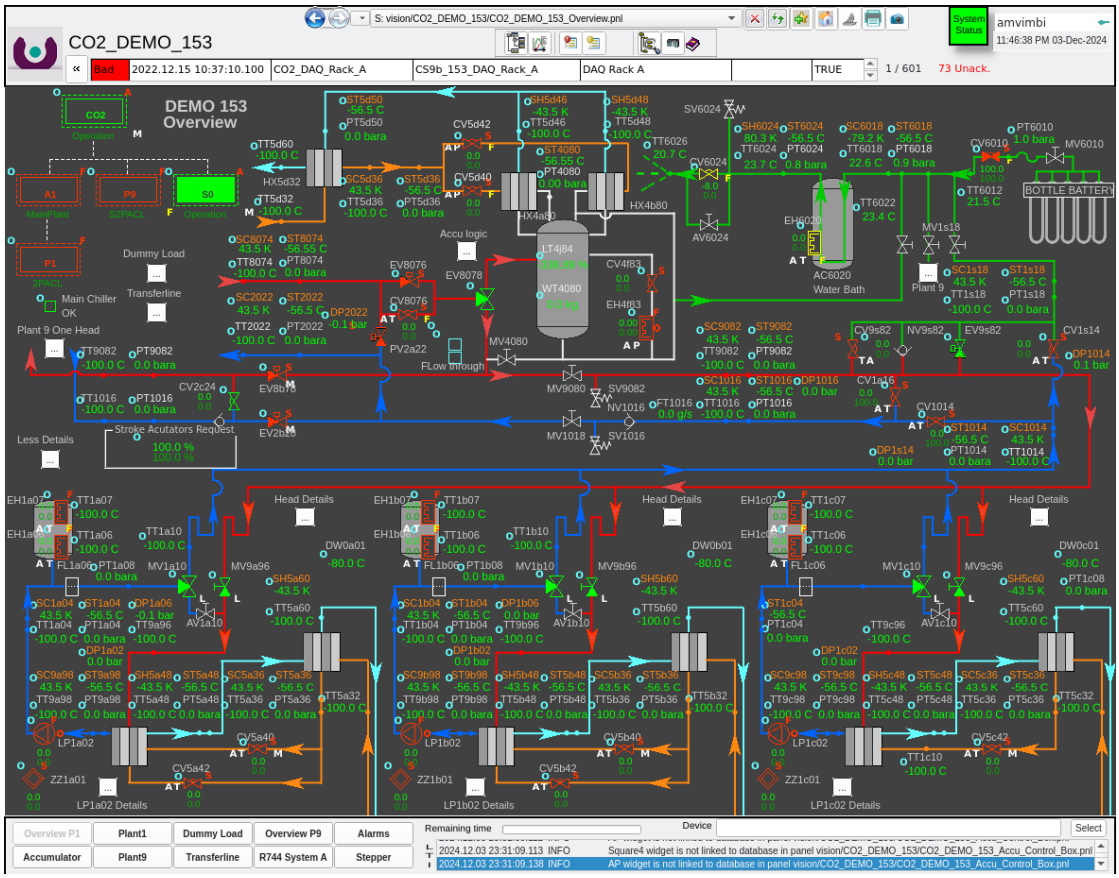

Figure 48: Demo SCADA Panels (Plant Overview)

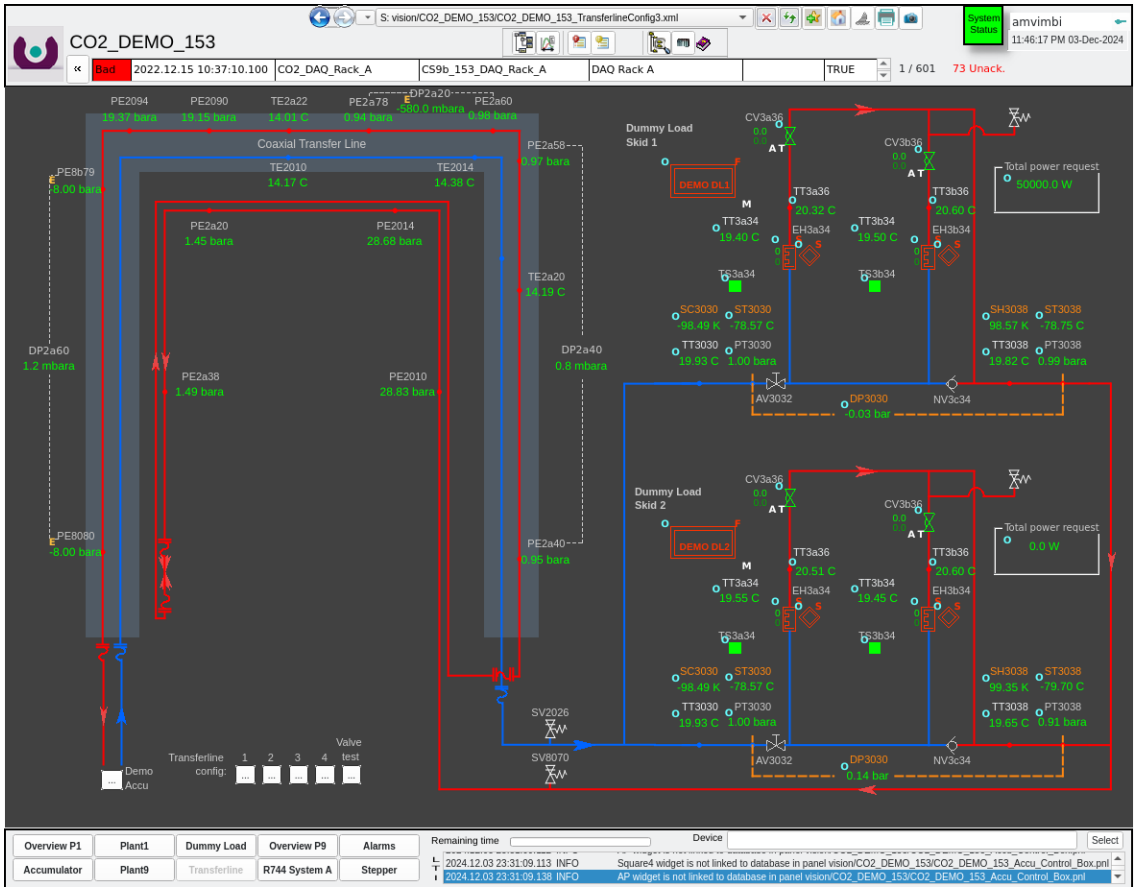

Figure 49: Demo SCADA panel (Transfer lines and Dummy Loads)

6.2 Data Post-Processing

Two approaches were employed to retrieve the measurements for Demo. The first approach involved saving trends as Comma-Separated Value (CSV) files, which could then be read and post-processed using a MATLAB script. The second approach, later adopted as a substitution for the first one, uses a MATLAB script to read previously exported data into data structures in MATLAB, which could then be processed further. The first post-processing step involved filtering to remove noise from the measurements so that trends could be clearly seen. Care was taken to design a filter that attenuates noise sufficiently while preserving fast dynamics of interest. Timber internally filters measurements during compression. The compression policy saves a subsequent data point if it changes beyond a predefined deadband or after a preset time, resulting in asynchronous sampling. Ignored entries may be interpolated or padded with the preceding entry. For the purpose of this research, interpolation was used, which is equivalent to convolving the measurement sample train with a triangular pulse, which, in the frequency domain, has an impulse response of a squared Sinc function; this has bad pass band behaviour [71]. This can result in some spurious behaviour and excite resonance in moving average filters such as the Savitzy-Golay filter. Consequently, a simple second-order discrete Butterworth filter was used for filtering, and Figure 50 illustrates the difference between unfiltered (noisy) and filtered measurements. It shows that the trends are easier to see for filtered measurements where measurements are noisy.

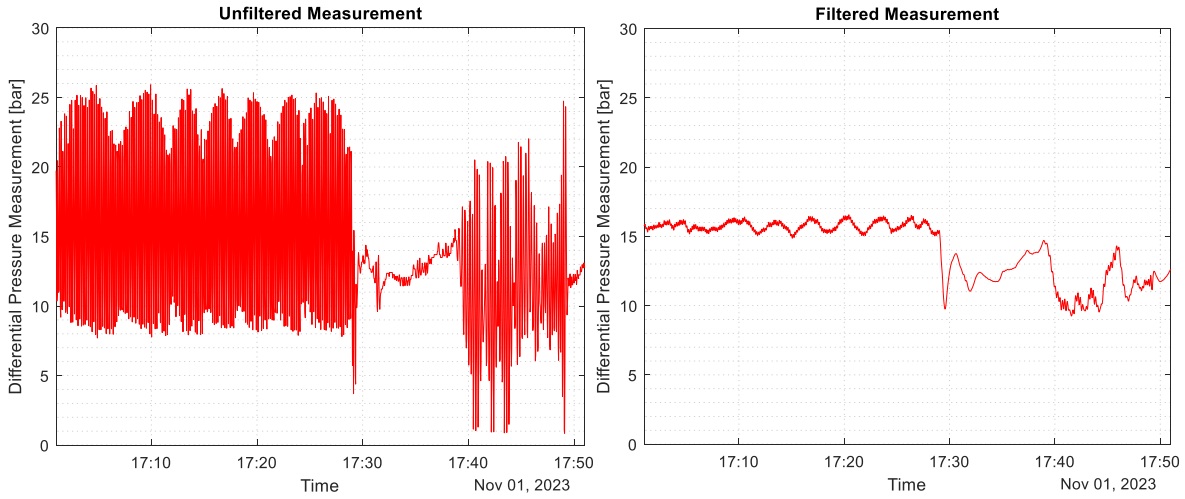

Figure 50: Unfiltered and Filtered Measurements

On the other hand, the simulation data was exported as CSV files, which could also be loaded into MATLAB to generate various plots. Once both post-processed measurements and simulation data are loaded into the MATLAB workspace, a MATLAB script searches for and finds the starting point for the simulation intervals of interest and aligns it with the starting point of the experiment using the stepper. Then, the discrete events and trajectory behaviour are plotted as they are from that point on, allowing for a fair comparison between simulation data and measurements.

Simulations were conducted using a model built in EcosimPro V6.02 on a Dell OptiPlex 7000 with a 12th-generation Intel(R) Core (TM) i5-12500 3GHz processor and 16GB RAM. DASSL_SPARSE solver was used for the reasons mentioned in 4.6.1, and the simulations were carried out so that the initial and boundary conditions were consistent with those of Demo during the corresponding experiments. The experiments cover startup, steady state and setpoint changes, load changes, and redundancy experimentation. To cover the entire operational space in the full system test, the main plant is started in T2APCL mode while the backup is started in standby mode (S2PACL_StB). Then, the main plant is shut down during operation to simulate a failure, prompting the backup plant to take over and run in S2PACL mode. The Main plant is then restarted in backup mode (S2PACL_StB) and subsequently takes over the accumulator and load from the backup plant. This sequence covers all modes of operation.

6.3 Startup & Stepper Simulation

6.3.1 Methodology

This experiment recreated a plant run that was conducted on February 15th, 2024. The main plant was started, and it was allowed to traverse its startup sequence in T2PACL mode automatically. Essentially, startup should be a simple single-button operation. The following

initial conditions and states of controlled variables were imposed, consistent with those of the actual system.

Table 1: Initial Simulation Parameters

Parameter	Value	Units
Initial pressure	35	Bar
Initial temperature	2.7	°C
Initial accumulator liquid level	80	%
Pump stroke	100	%
Pump speed	35	Hz
Accumulator volume	456	L

6.3.2 Experimental Data

At startup, the key objective is to subcool the pump inlet for the reasons mentioned in 1.1.1. However, premature delivery of cold flow to the detector is avoided to prevent detector thermal shock. Figure 51 demonstrates the startup of the Demo. The right axis always represents the accumulator and plant steppers, as explained in 3.3. The dashed dot and dashed lines represent the plant and accumulator, respectively. All the other metrics are always on the left axis. The experiment started at the twentieth minute when both the Main plant and accumulator transitioned from **Step 0** (Safety) to **Step 1** (Liquefy). Then, the surface storage pressure was reduced to 35 bars from 40 bars for this experiment. The accumulator and, hence, the whole system also ramped down to 30 bar to guarantee that 5 bar differential pressure from surface storage to the system is maintained so that the surface storage could use this to charge (fill) the system. In **Step 1**, the external heat exchanges began condensing and subcooling the pump inlet, as shown by the navy blue trace in subplot (c). This lasted for 60 minutes, owing to the large thermal inertia in the system.

Once the liquefication was complete, the plant transitioned to **Step 2,** where the pump commenced circulation - which is captured by the mass flow starting in subplot (b). In addition to the synchronising script, a timer mechanism was used to synchronise the simulation from the point when subcooling was achieved. Once this alignment was achieved, the simulation proceeded without interventions, ensuring that the resulting dynamics behaviour was authentic. This approach ascertained that the data accurately reflects the dynamics system behaviour once flow began. Circulation is necessary so the pump discharge can be used for generation during the detector pressurisation in **Step 2**. The pump flow bypassed the detector and mainly flowed through valves c and d – the TL differential pressure control valve and TL bypass valves to avoid thermal shock to the detectors. Immediately when circulation began, the pump inlet temperature increased to 5˚C below the accumulator outlet temperature. Valve g (the BPR) began throttling, as depicted by the red trace in subplot (d). Once the detector was fully liquid, the plant and the accumulator proceeded to **Step 3**.

In **Step 3**, the plant was already in operation, and the accumulator was waiting for valve c to build the design differential pressure of 15 bar across the transfer lines. Once this differential pressure was achieved, the detector received a nominal mass flow of around 730g/s, as shown by the blur trace in subplot (b). Then, the accumulator transitioned to Step 4, where temperature

regulation started ramping down to the user setpoint – -30C. Once the saturation temperature reached this user setpoint, the accumulator went on to Step 5, which is its nominal operation step where it will read for the load to turn on. This marked the end of the autonomous start-up sequence.

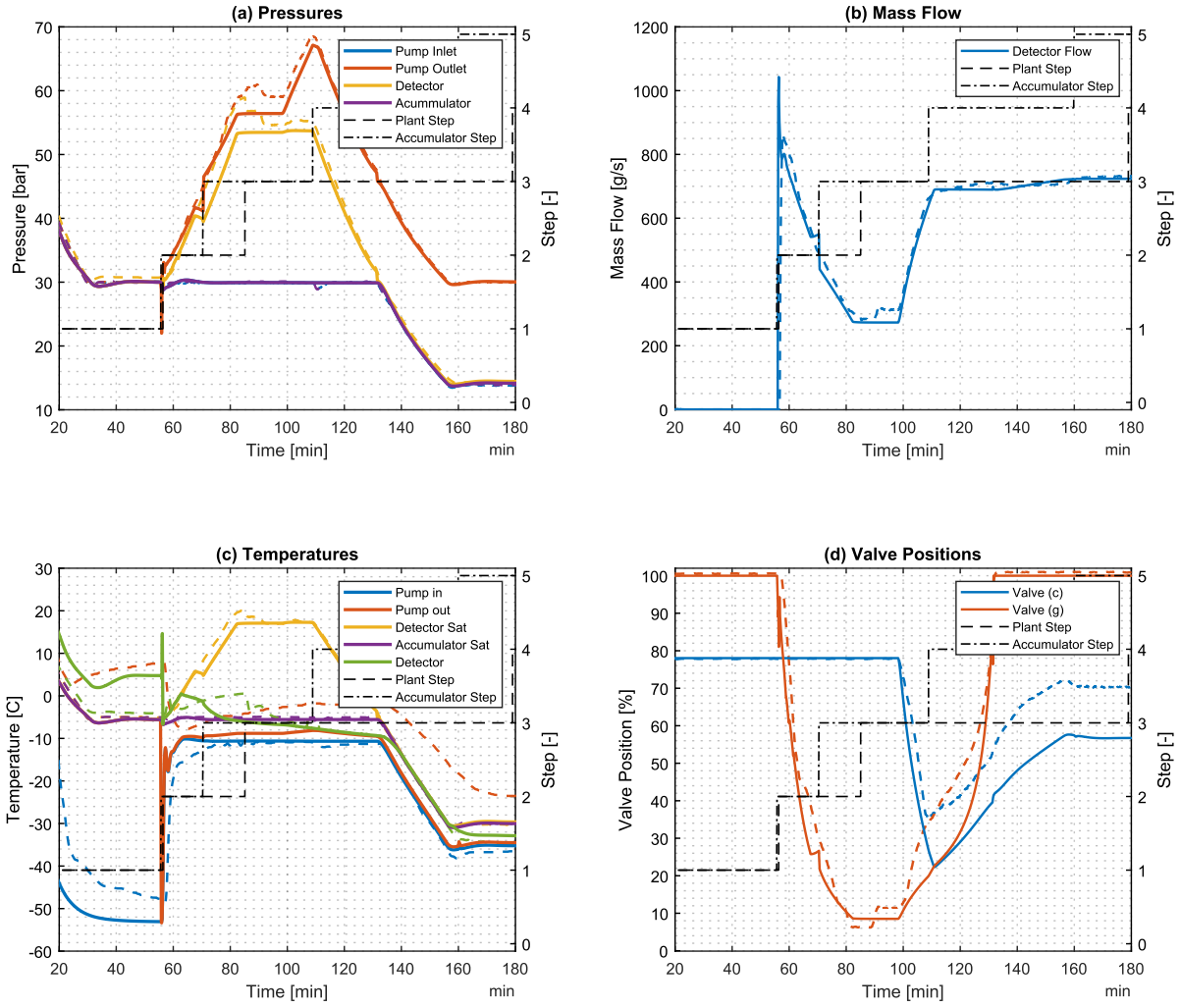

Figure 51: Start-up Simulation (Experimental – Dashed lines, EcosimPro Simulation – Solid lines)

6.3.3 Analysis

Figure 51 shows that Demo follows its startup sequence successfully. First, the pump heads were liquefied up to just before the 60th minute, and then once the pump commenced flow, the BPR was used to increase pressure and liquefy the plant at ambient temperature (6˚C in this case). Subplot (c) corroborates this because the detector saturation temperature trace, in yellow, exceeds the actual detector temperature – in green. Immediately when the pump started, the inlet temperature rose to 5˚C below the accumulator. This resulted from the action of the DT controller, which began regulating the subcooling of 5˚C. Both the simulation data and the measurements indicate that in order to liquefy the system at warmer temperatures, the pump discharge pressure may enter the supercritical region. Broadly, the BPR lift trajectory once

again shows the quadratic relationship between pressure and mass flow. Mass flow, which is directly proportional to the valve lift the linear valves used, is proportional to the square root of pressure drop. In other words, the pressure drop is proportional to the square of mass flow, and this is seen in the nearly parabolic profile of the valve lift as the controller ramped up the pressure at a linear rate limit.

6.4 Steady-state Operation & Setpoint Changes

6.4.1 Methodology

An experiment that was identical to a plant operation that was carried out on Demo from the 19th of March 2023 and the experiment from February 15th, 2024, for warm operation. On the 19th, the system was operating cold and the setpoint was changed from -45˚C to -30˚C and then back to -40˚C. The warm operation experiment involved operating the system at a setpoint higher than the surface storage limit (0˚C) and then ramping down to (-30˚C). This provided the necessary coverage to test steady-state operation, response to setpoint changes, and, more importantly, the handover between the BPR and accumulator control. This emulated a case where the operator requested the detector to operate at a warm temperature and ramps down the temperature.

6.4.2 Experimental Data

Figure 52 shows the system arriving at the 100th minute running stably at a setpoint of -45˚C. This is equivalent to the accumulator pressure of 8.3 bar. Then, the operator requested a saturation temperature of -30˚C, which the system then ramped up to just after the 100th minute; the setpoint is finally reduced back to -40˚C and is followed by the system.

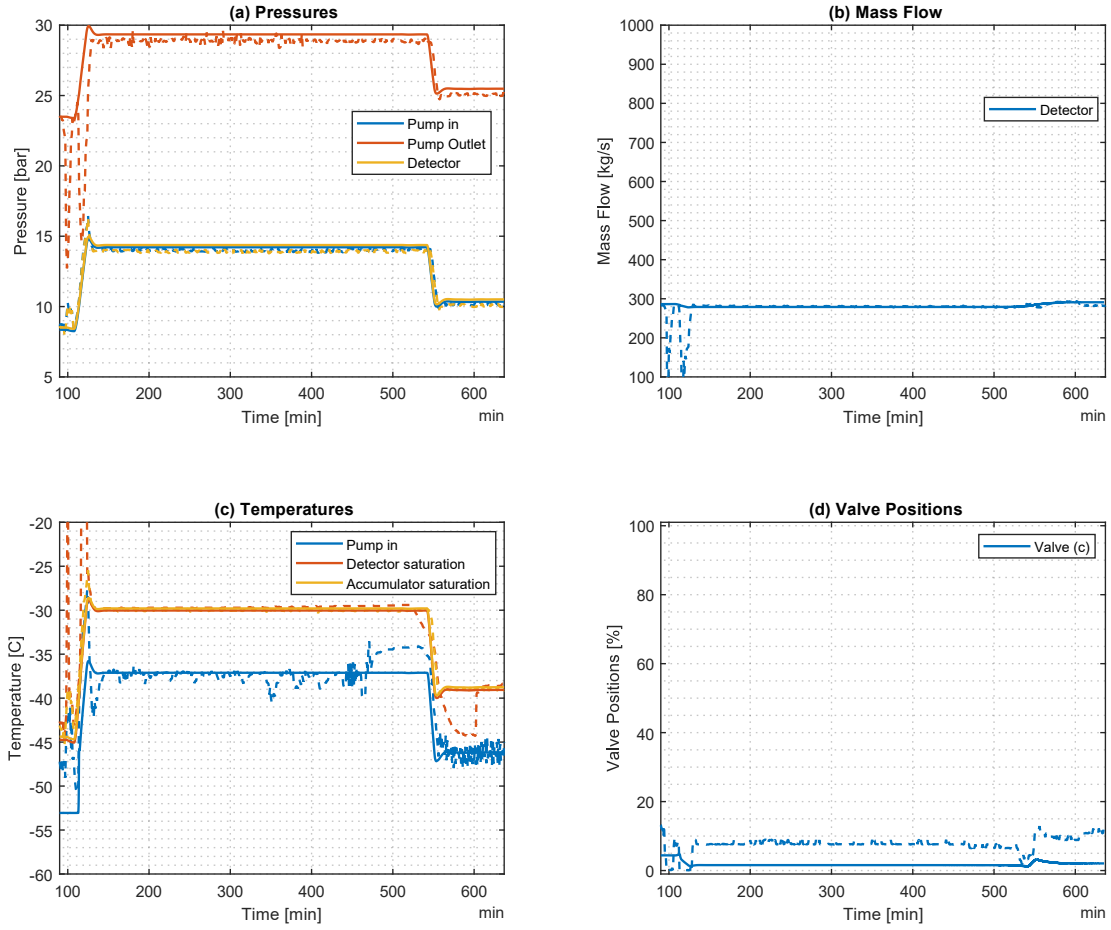

Figure 52: Setpoint Change (Cold) (Experimental – Dashed lines, EcosimPro Simulation – Solid lines)

The warm operation can be observed during the startup experiment in Figure 51 above. There, the system setpoint was set to the detector temperature, which was 17˚C; subplot (a), the pressure plot, shows that in order to achieve this, the detector was at a pressure of 54 bar – much higher than the 35-bar surface storage limit corresponding to a temperature of 17˚C. During the 109th minute, the system setpoint became the user setpoint request of -30˚C, and the system began ramping down to the setpoint. At the moment of the handover, valve (g) - the BPR opened fully, as did its bypass. Then, the accumulator continued cooling and ramping down the temperature at the preset rate until -30˚C is reached. The setpoint was tracked with zero steady state.

6.4.3 Analysis

Figure 52 shows that the results from the full-scale simulation are corroborated by the measurements obtained from Demo. The system follows the user setpoint. Secondly, the cold operation also demonstrates that the PCO executes the same logic as Demo. When a setpoint colder than or equal to -45˚C is requested, the system switches to Super Heat Control (SHC), where the controller on the primary side regulates the external heat exchanger superheat. This is seen in that the inlet temperature is colder than the 7˚C DTC set point. When the BPR regulation was engaged, the system maintained pressure above the accumulator pressure at the

detector, as shown by the detector pressure in subplot (a). The consequence is that the detector was able to sustain warm operation at 17˚C. Measurements from Demo have oscillations which are attributed to sensor noise and pulsations that are caused by the pump, which are absent in the simulation. The results further confirm that the simulation PCO executes the same logic as Demo. That is, when the exit saturation temperature of the detector was above the surface storage limit, the BPR handled the temperature regulation. Conversely, when the saturation temperature crossed the limit to a lower value, the BPR went into tracking mode (inactive), and the accumulator took over the temperature regulation. One observation is that during cold operation when the process value went colder, the density at the pump inlet increased; hence, the pump generated slightly higher flow, as seen just after the 550th minute in Figure 52. Consequently, more flow needed to be bypassed, which is why valve (c) lift increased as the system got colder.

Another key observation from the data is that when the system crossed over between the BPR and accumulator regulation, there was a negligible drop in pressures and, therefore, temperatures – in the 240th minute in subplots (a) and (c). This was caused by the BPR (valve (g)) bypass opening as the system enters accumulator control mode; hence, the intrinsic pressure drop of the BPR valve is eliminated by the opening of its bypass (valve (h)) which has a much larger C_v. This eliminates unwanted pressure drop by the BPR at high flow, which ensures the accumulator well approximates the detector exit pressure. Because of this intrinsic pressure drop, there exists a deadband of temperature setpoints which the system will track with an offset if requested by the user, and the lower bound of this band is the surface storage limit, while the upper bound is this threshold plus the intrinsic pressure drop of the BPR. Here, when the bypass is closed, and a temperature setpoint just above the limit is requested, the BPR is fully open, and yet its innate pressure drop results in the process value being slightly higher than requested. Nonetheless, during the handover, the BPR and its bypass were open fully, and the split-range controller handed the control over to the accumulator, which continued ramping down the pressure until the setpoint was reached.

All in all, the simulation captures the discrete behaviour of Demo well, including the handover logic and the SHC/DTC switching logic. In addition, the simulated trajectory behaviour of metrics such as pressure and temperature agree with those of Demo. Both the simulation and the measurements illustrate that the BPR can be used to get the system to higher setpoints than the surface storage limit.

6.5 Load changes (Disturbance rejection)

6.5.1 Methodology

An experiment identical to that carried out on Demo on 15th October 2023 was conducted with the model after imposing the initial conditions consistent with the operation on that day. The system was allowed to run at -45˚C; then, the detector load was increased in steps of 10kW.

6.5.2 Experimental Data

Figure 53 below illustrates the pressure, mass flow, temperature, level, valve positions and detector load trends during this interval. The subplot (d) expresses the detector load as a percentage of the maximum load capacity – 100kW. The measurement and simulation data indicate that each time when the load was stepped up, there was a slight increase in pressures and, hence, temperatures in the system, as seen in subplots (a) and (c). Furthermore, When the detector power was turned on, there was a substantial liquid level increase in the accumulator, followed by smaller level increases each time the load was stepped. Finally, throughout the interval, the mass flow to the detector remained stable and virtually undisturbed.

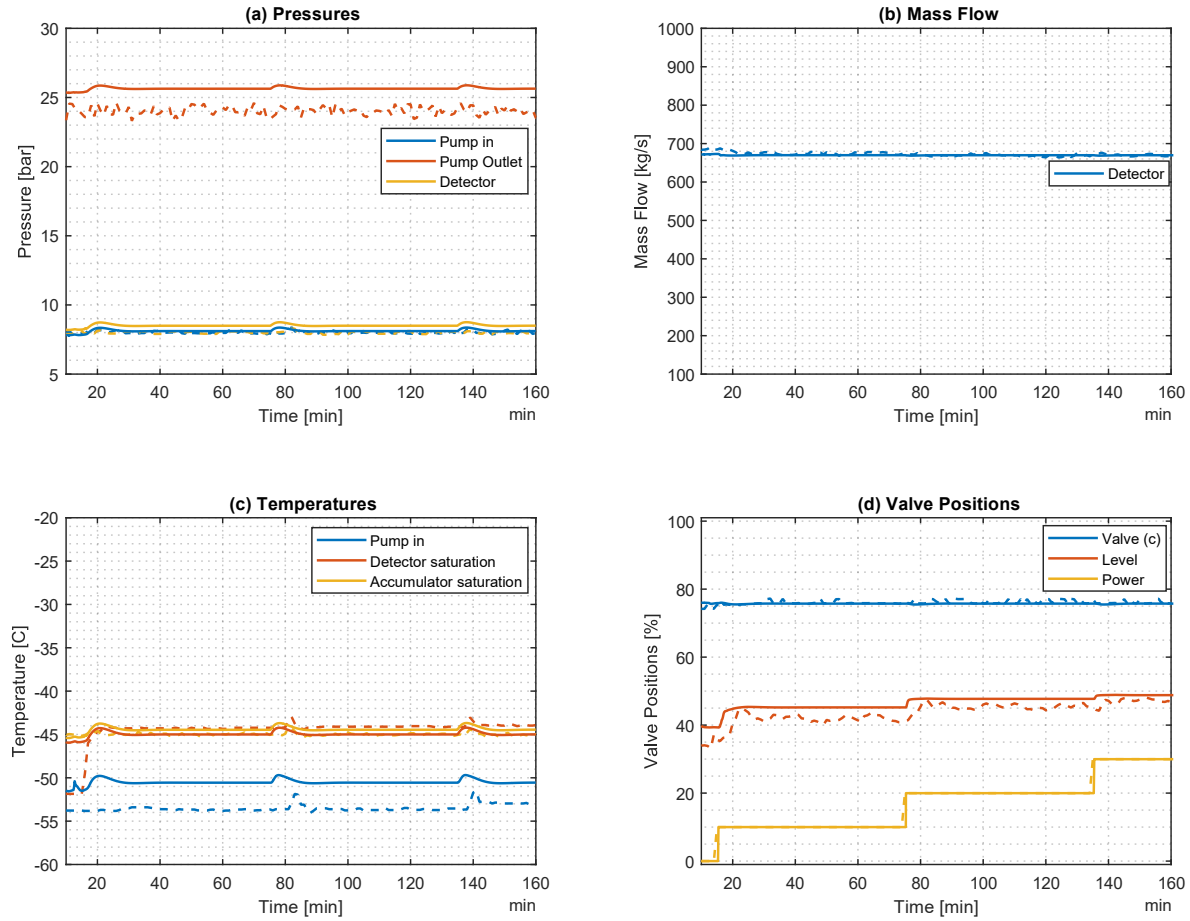

Figure 53: Load Change (Experimental – Dashed lines, EcosimPro Simulation – Solid lines)

6.5.3 Analysis

The load change experiment results above demonstrate that the simulation is consistent with the trajectory behaviour of the Demo. Subplot (a) of Figure 53 shows that each time the load was stepped up, there was a disturbance in the pressure. This was because when the detector power suddenly increased, it caused a sudden increase in boil up at the detector; the expanding vapour, in turn, caused a pressure surge that increased the pressure of the accumulator and

hence system pressure each time the load is stepped; the saturation temperature controller in the accumulator then rejected this disturbance by ramping up the cooling action and returning the pressure to the setpoint. The transfer line differential pressure controller also rejected pressure disturbance, holding a 15-bar pressure drop across the transfer line for the entire interval; hence, the mass flow to the detector remained almost undisturbed at its nominal value, as seen in subplot (b). As for the level change, when the power is turned on, there a pressure surge occurs at the detector, and the liquid CO_2 downstream is pushed down at a higher mass flow than that which is imposed by the pump; the only possible path for the surplus flow is the accumulator; hence, the level increases [5]. The vice versa is also true. The changes in the level gradually decrease with the change in level per power increase after power is on because the void fraction change per change in vapour quality is highest at low quality.

6.6 Redundancy

6.6.1 Methodology

This experiment recreated one that was conducted on 1st November 2023. The operation here exploited the design that both plants have non-return valves preventing backflow; this allows both to be connected to the load via the accumulator simultaneously in a configuration shown by Figure 54 below. The plant at a lower pressure level imposes a constant mass flow, which guarantees that all flow from the plant operating at a higher pressure level circulates exclusively through that plant. During the takeover, the plants enter a differential pressure contest where the plant with a higher differential pressure takes over the load from the other. In this experiment, the main plant was running in S2PACL mode while the backup was running in S2PACL_StB mode, sending flow to the bypass valve (n). Then, failure was simulated by turning off the main plant. In reaction to this, the accumulator PCO swapped out the main plant by opening the pneumatic valves (m) and (l), redirecting flow from the backup plant to the load. After the backup operation stabilised, the main plant was restarted in S2PACL_StB and allowed to automatically take over the accumulator and load from the backup plant.

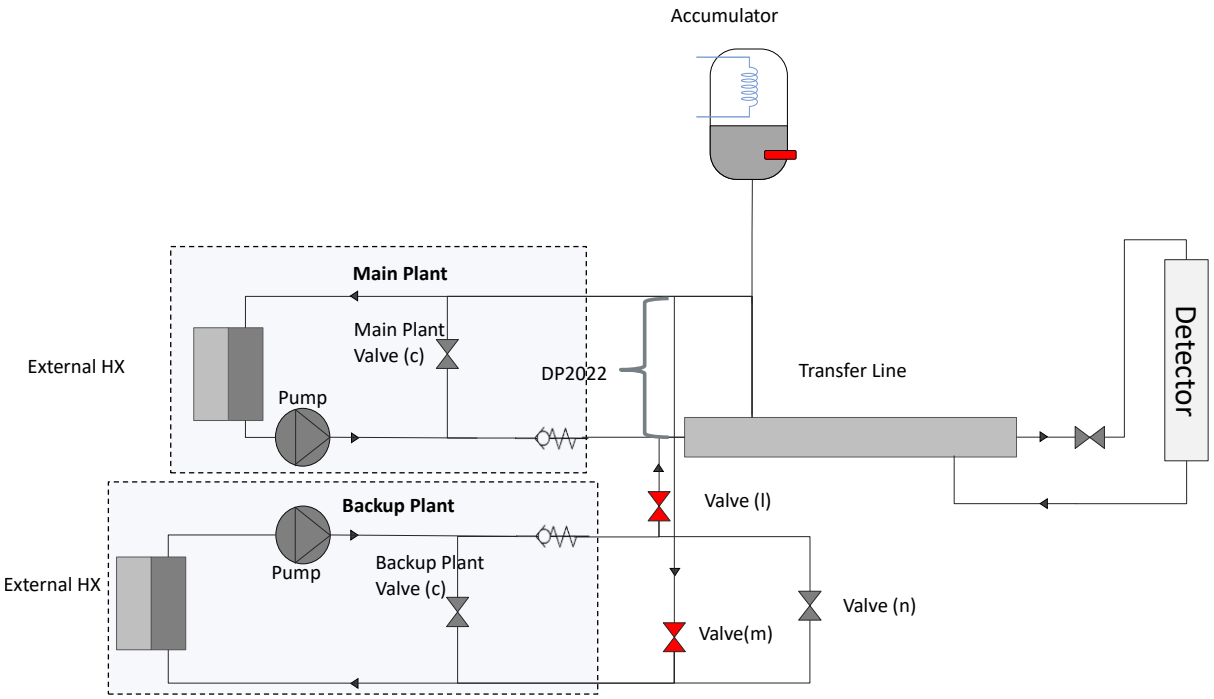

Figure 54: Swap and Re-takeover Simplified Schematic

Once the primary plant had restarted and was ready to supply liquid to the load, its PCO set its pressure drop setpoint to half a bar above that of the backup plant. Half a bar is high enough to ensure that one plant can take over successfully while also ensuring that the load does not receive excessive flow. To achieve this, the valve (c) of the main plant, responsible for differential pressure control, began to close and redirected more flow to the detector. Consequently, the backup plant's differential pressure control valve (c) opened and bypassed more flow as the common process value exceeded its setpoint. This resulted in a seamless handover where the flow lost by the load to the bypass in the backup plant was compensated by the primary plant so that the detector saw no disturbance in flow. This setup incorporates redundancy, as either plant failing during the takeover can be compensated for by the other. Furthermore, even if both plants fail to develop the required differential pressure individually, they can supply the load jointly.

6.6.2 Experimental Results

Figure 55 shows that the Main plant failed at the 34th minute, which is seen in the loss of differential pressure developed by the main plant (blue trace) shown in subplot (c) and hence the mass flow delivered by this plant to the load (orange trace) shown by subplot (b). The backup plant immediately sent flow to the detector during the failure, and the system continued running.

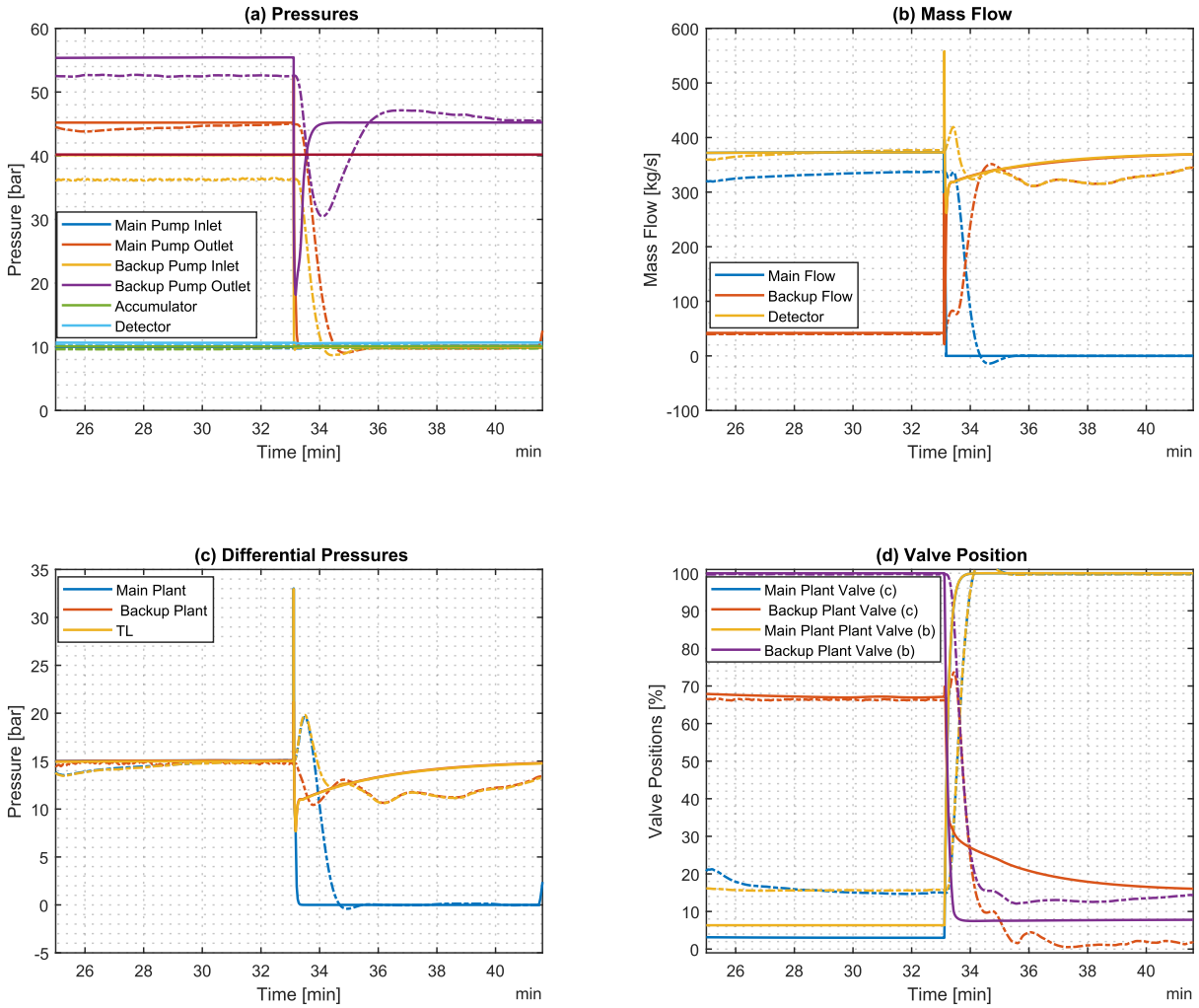

Figure 55: System Swap (Experimental – Dashed lines, EcosimPro Simulation – Solid lines)

Figure 56 is a zoomed-in plot of the Swap. At the instant of failure, there is a minor disturbance in the detector flow, after which the system recovered to the nominal value of 376 g/s. This is captured by the flow through the detector in subplot (b). Subplot (c) also shows a corresponding surge in the differential pressure across the load 33.2 minutes into operation.

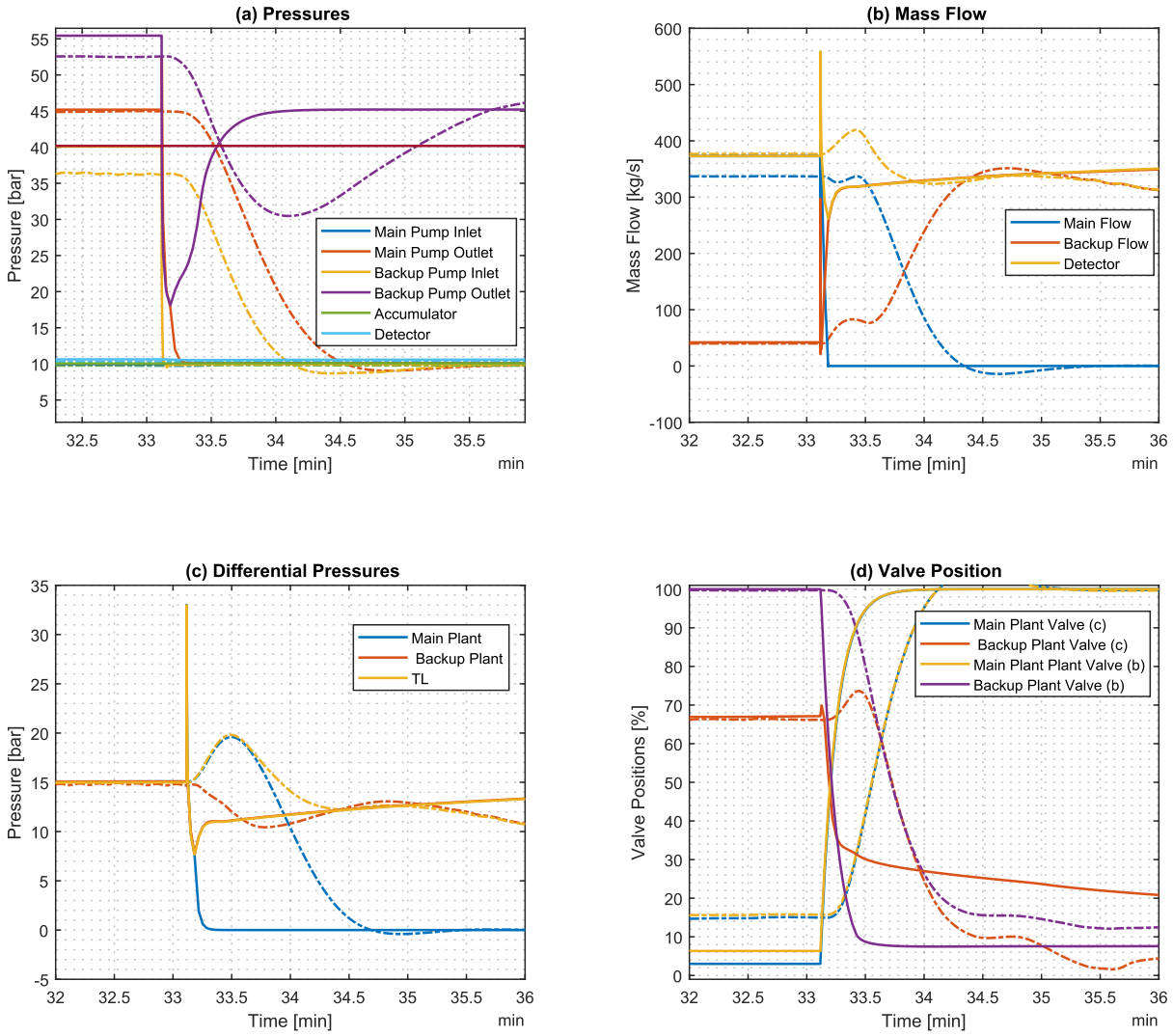

Figure 56: System Swap (Experimental – Dashed lines, EcosimPro Simulation – Solid lines)

Measurements and simulation results for the re-takeover are shown in Figure 57. The figure shows that the main plant was restarted once the backup operation had stabilised, generating a differential pressure of 6 bars in Demo and 4 bars in the simulation. From there, the main plant began increasing its differential pressure to half a bar above that of the backup plant. As the differential pressure across the transfer line approached and exceeded fifteen bar – which is the setpoint for the backup plant, the differential pressure controller in the plant began to open its valve and bypass more flow through its valve (c) to compensate for the process value that exceeded the setpoint. This continued until the backup plant bypassed its full flow, and the main plant took over the load completely. This trajectory behaviour is captured by the mass flow in subplot (b) of Figure 57. The backup plant pump discharge pressure, differential pressure, and mass flow measurements show some oscillatory behaviour.

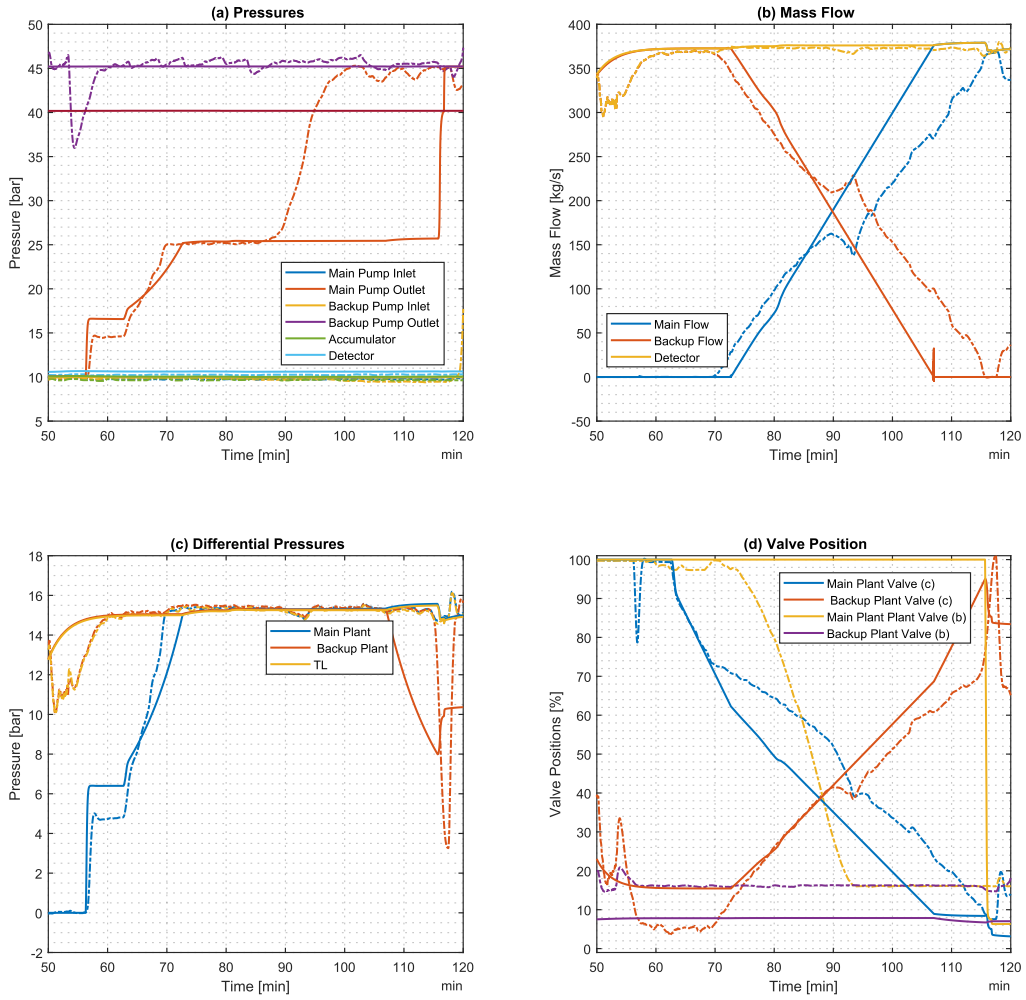

Figure 57: Retake over (Experimental – Dashed lines, EcosimPro Simulation – Solid lines)

6.6.3 Analysis

The results in 6.6.2 illustrate the redundancy built into the system. Before the main plant failed, the backup operated on standby, sending 42 grams of flow to the bypassing load-side expansion valve, valve (n), and the rest of the pump flow flowed through valve (c). Upon failure of the main plant. The discrete logic executed by the accumulator PCO logic opened the pneumatic ON-OFF valves – valve(l) and valve(m) and redirected 338g/s of flow from the Backup Plant to the load. The differential pressures across both plants and the transfer line (TL) in both the simulation and Demo experiment are also consistent with the trajectory behaviour of the mass flows. That is, when the main plant failed, its developed differential pressure fell to zero, as shown by subplot (c) of Figure 55. The speed with which flow stopped in the simulation is faster than the measurement, as depicted by Figure 51, and this is the case because the full momentum equation has not yet been implemented in the current simulation in order to improve simulation speed, as described in 4.2. Furthermore, the discrepancy in the pump outlet pressure is due to the fact that the simulation PCO executes the updated logic where the pump discharge control valve regulated five bar above the surface storage only after the swap is completed as opposed to during the swap as Demo did.

The backup plant, on the other hand, maintained its developed differential pressure of fifteen bar, which was then exposed to the load during failure; this resulted in the transfer line maintaining a differential pressure of 15 bar, which guaranteed nominal mass flow. This behaviour is also captured by the transfer line (TL) plot in subplot (c) of Figure 55. It is worth noting that the differential pressure across the transfer line and, hence, the load was disturbed momentarily during the swap; this is because it is limited by the opening speed of valve (l) and valve (m). In other words, immediately when the main plant fails, its differential pressure goes to zero, and there exists a brief period when these pneumatic valves open when the differential pressure across the detector falls below its nominal value. This is seen as a dip in the differential pressure across the transfer lines (TL). The implication is that the detector flow will also have a similar disturbance where the mass flow momentarily falls below the nominal value at the swap. However, in the context of detector cooling, this disturbance does not pose a significant threat because it lasts only 25 seconds and will be filtered out by the detector's thermal inertia. The retake-over is also fail-safe in that if one of the plants fails during retake over, the remaining plant automatically takes over the full load.

In summary, the discrete logic and trajectory behaviour of the simulation and demo results are consistent. After accounting for the sensor noise and other discrepancies due to constraints during operation, the results corroborate each other, and both the simulation and experiment data demonstrate that the system will operate beyond the failure of the main plant.

7.Conclusions and Recommendations

> Science is a relentless pursuit of understanding. Your conclusions are not an endpoint but a launchpad for future inquiry.
>
> - Max Planck

7.1 Conclusions

The 2PACL systems have enjoyed extensive research because they form a crucial component of the monumental high-luminosity upgrade at CERN. These systems offer novel solutions that address non-trivial engineering problems under tight engineering constraints. The new systems discussed in this dissertation enable precise control of detector temperature over large distances by elegantly exploiting two-phase thermodynamics, thereby allowing the separation of active and passive components for better system maintainability. The addition of a flow-through mode improved the subcooling control. Finally, the incorporation of surface storage guarantees that the system adheres to the safety regulations for the amount of CO_2 that can be stored under pressure underground while also ensuring the availability of CO_2 to charge the system on demand. The systems achieve all these while using a natural refrigerant with a global warming potential of three orders of magnitude less than comparable chlorofluorocarbon-based refrigerants.

This dissertation commenced by surveying the literature on 2PACL systems as well as the thermodynamics applicable to their operation mechanism in Chapter 2. This chapter further set a broader context for the research on simulations of the new state-of-the-art cooling systems at CERN. The surveillance of literature revealed that the 2PACL had undergone an extensive redesign since its conception at NIKHEF, allowing it to meet CERN's tight engineering constraints and unparalleled scale. However, simulations that include the new designs, such as the BPR operation, flowthrough mode, and surface storage, are lacking. In addition, there is no literature on the system-level study of these new systems. Finally, little emphasis is placed on the procedural design of controllers for the feedback loops in the system. Both of these discoveries from the literature review gave relevance to this investigation

Chapter 3 then proceeded by describing Demo—CERN's 2PACL prototype. This chapter describes the main components of the system. It is followed by a detailed description of the operation modes of various components and the PLC hierarchy of the system. In Chapter 4, the bulk of the modelling and design are detailed. Here, the modelling philosophy is briefly discussed, and next, the fundamental conservation equations that form the basis of capacitive components are outlined. The system was then modelled, and the forward loops for critical feedback loops were derived. From these, the plant uncertainties were revealed – sources of uncertainty included for the two main loops included the net mass inflow changes in thermodynamic properties with respect to the operation point. The derivation of forward loops shows that both the accumulator and BPR pressure control are first order systems with

uncertain gains and corner frequencies. However, the accumulator has a slow pole that can momentarily move to the right-hand plane. The system will always be stable, which is enabled by the high gain of the actuator and a properly tuned controller.

Quantitative Feedback Theory was then used to conduct stability and sensitivity analysis for the critical loops in the system. This was followed by the design of robust controllers that strike a balance between sensitivity and performance for the feedback loops in Chapter 5. Chapter 5 also illustrates that the QFT can be used to design robust controllers that mitigate plant uncertainty while offering performance and accounting for sampling effects. In Chapter 6, data acquisition and post-processing procedure are discussed, next, results were presented and analysed. The analysis reveals that the model accurately captures discrete behaviour executed by the PLC, and differences occur only where there have been logic updates and or where are there are some uncaptured dynamics. The simulation captures the trajectory behaviour of the demo well. The discrepancies, such as in the mass flow transient speed and oscillations in measurements, can be accounted for by the absence of the full momentum equation, sensor noise and pump pulsation, respectively.

In conclusion, the EcosimPro model for Demo captures both the discrete and continuous behaviour well enough to enable valuable insights about the system to be gained. The model serves as a great tool for the system-level study of the new intricate cooling systems.

7.2 Future Recommendations

Further work can include the implementation of full momentum conservation in order to ensure that the mass flow transients are as close to reality as possible. The model could also be used for to conduct an audit of failure modes in the stepper logic, instrumentation and actuators. The system should be connected in a Hardware-in-a-Loop configuration. Such a setup will be beneficial for virtually commissioning the PLC logic while the plant is under intervention and/or the plant is being built. In addition, the model could be used to explore the benefits of other control schemes such as the Shinskey control scheme – effectively using the valve control and the fast heater dynamics to improve the accumulator control. Finally, a virtual commissioning setup may be used for operator training.

8.References

[1] CERN. "Facts and figures." CERN. https://public-archive.web.cern.ch/en/LHC/Facts-en.html#:~:text=At%20full%20power%2C%20trillions%20of,head%20collisions%20of%2014%20TeV. (accessed 17/08, 2024).

[2] E. S. Planetarium. "Aerial view of CERN." https://supernova.eso.org/exhibition/images/cern-aerial-cc/ (accessed 05, 2024).

[3] CERN. "The ATLAS Detector." https://atlas.cern/Discover/Detector (accessed 05, 2024).

[4] J. Daguin *et al.*, "Evaporative CO2 cooling system for the upgrade of the CMS pixel detector at CERN," in *13th InterSociety Conference on Thermal and Thermomechanical Phenomena in Electronic Systems*, 30 May-1 June 2012 2012, pp. 723-731, doi: 10.1109/ITHERM.2012.6231499.

[5] V. Bhanot, "Process Modelling and Dynamic Simulation of CO2 Cooling Systems based on Two-Phase Pumped Loops," Doctor of Philosophy, Mechanical, Aerospace and Civil Engineering, University of Manchester Manchester, 145, 2020. [Online]. Available: https://research.manchester.ac.uk/files/173354610/FULL_TEXT.PDF

[6] J.-H. Arling *et al.*, "Performance tests of dual-phase CO2 cooling for particle detectors," *Journal of Physics: Conference Series,* vol. 2374, 11/01 2022, doi: https://doi.org/10.1088/1742-6596/2374/1/012063.

[7] J. Daguin *et al.*, "Evaporative CO2 cooling system for the upgrade of the CMS pixel detector at CERN," *13th InterSociety Conference on Thermal and Thermomechanical Phenomena in Electronic Systems,* pp. 723-731, 2012.

[8] L. Cheng, G. Ribatski, J. Moreno Quibén, and J. R. Thome, "New prediction methods for CO2 evaporation inside tubes: Part I – A two-phase flow pattern map and a flow pattern based phenomenological model for two-phase flow frictional pressure drops," *International Journal of Heat and Mass Transfer,* vol. 51, no. 1, pp. 111-124, 2008/01/01/ 2008, doi: https://doi.org/10.1016/j.ijheatmasstransfer.2007.04.002.

[9] L. Cheng, G. Xia, and J. R. Thome, "Flow boiling heat transfer and two-phase flow phenomena of CO2 in macro- and micro-channel evaporators: Fundamentals, applications and engineering design," *Applied Thermal Engineering,* vol. 195, p. 117070, 2021/08/01/ 2021, doi: https://doi.org/10.1016/j.applthermaleng.2021.117070.

[10] R. Mastrullo, A. W. Mauro, A. Rosato, and G. P. Vanoli, "Carbon dioxide heat transfer coefficients and pressure drops during flow boiling: Assessment of predictive methods," *International Journal of Refrigeration,* vol. 33, no. 6, pp. 1068-1085, 2010/09/01/ 2010, doi: https://doi.org/10.1016/j.ijrefrig.2010.04.005.

[11] J. Wu *et al.*, "Investigation of heat transfer and pressure drop of CO2 two-phase flow in a horizontal minichannel," *International Journal of Heat and Mass Transfer,* vol. 54, no. 9, pp. 2154-2162, 2011/04/01/ 2011, doi: https://doi.org/10.1016/j.ijheatmasstransfer.2010.12.009.

[12] P. Barroca, "Modelling of CO2 cooling of the ATLAS ITk Pixel Detector," 2019.

[13] M. Doubek *et al.*, "Measurement of heat transfer coefficient in two phase flows of radiation-resistant zeotropic C2F6/C3F8 blends," *International Journal of Heat and Mass Transfer,* vol. 113, pp. 246-256, 2017/10/01/ 2017, doi: https://doi.org/10.1016/j.ijheatmasstransfer.2017.05.049.

[14] B. Verlaat and L. Contiero, "Cooling Below -40°C." [Online]. Available: https://indico.cern.ch/event/1228626/contributions/5238839/attachments/2588303/4465914/VeloWorkshopFeb23.pdf

[15] W. Poonsawat, C. Kobdaj, M. Sitta, and Y. Yan, "Calculation of radiation length in materials," CERN, Geneva, arXiv:1706.02110, 2010.

[16] B. Verlaat *et al.*, "The development of the CO2 cooling plants for the upgrade silicon detectors of ATLAS and CMS at CERN," presented at the 16th Gustav Lorentzen, International Institute of Refrigeration, 2024.
[17] J. Daguin and A. Duccio, "Operation of the Tracker cooling system at HL-LHC," A. Onnela and N. Bacchetta, Eds., Geneva: CERN, 2022.
[18] T. Hortala, "Carbon dioxide for the environment." [Online]. Available: https://home.cern/news/news/engineering/carbon-dioxide-environment
[19] B. Verlaat. *Development of the VELO Thermal Control System (VTCS)*. (2008).
[20] I. Sadrehaghighi, *Multiphase /Multicomponent & Multiscale Flows with Case Studies*. 2024.
[21] B. Verlaat, "Controlling a 2-phase CO2 loop using a 2-phase accumulator," 01/01 2007.
[22] B. Verlaat, "Cooling R&D needs for future detectors," ed, 2021.
[23] H. van Gerner and N. Braaksma, "Transient modelling of pumped two-phase cooling systems: Comparison between experiment and simulation," presented at the 27th European Space Thermal Analysis Workshop, Noordwijk, 2013.
[24] R. G. A. Bolder, "Numerical Simulation of a Two-Phase Thermal Control System," Master of Science, Technische Universiteit Delft, 2017. [Online]. Available: https://hdl.handle.net/10921/1435
[25] A. E. Aad G, Abdallah, Aleppo M, Alexa C, "The ATLAS Experiment at the CERN Large Hadron Collider," *Journal of Instrumentation,* 2008. [Online]. Available: https://jinst.sissa.it/LHC/.
[26] A. Koutoulaki, "CO2 evaporative cooling for the ATLAS detector," 2021.
[27] B. Verlaat *et al.*, "CO2 cooling challenges at CERN for the future phase 2 upgrade program," presented at the 25th IIR International Congress of Refrigeration, Montreal, 2019.
[28] J.-H. Arling, S. D. Cornell, I.-M. Gregor, F. Poblotzki, and A. Renardi, "Performance study of dual-phase CO2 cooling on the example of the ATLAS ITk strip end-cap detector," *Nuclear Instruments and Methods in Physics Research Section A: Accelerators, Spectrometers, Detectors and Associated Equipment,* vol. 1038, p. 166953, 2022/09/01/ 2022, doi: https://doi.org/10.1016/j.nima.2022.166953.
[29] J. Daguin and D. Abbaneo, *Operation of the Tracker cooling system at HL-LHC*, N. Bacchetta and A. Onnela, eds., Geneva: CERN, 2022. [Online]. Available: https://edms.cern.ch/document/2739902 Accessed on: 01/11/2023.
[30] U. Parzefall, "Silicon for High-Luminosity Tracking Detectors -Recent RD50 Results," *Physics Procedia,* vol. 37, pp. 899-906, 2012/01/01/ 2012, doi: https://doi.org/10.1016/j.phpro.2012.02.430.
[31] F. E. Cellier and E. Kofman, *Continuous System Simulation*. Springer US, 2006.
[32] V. Bhanot, L. Davoine, P. Pategna, A. Cioncolini, and B. Verlaat, "Design and Dynamic Simulations of Next Generation in Two-Phase CO2-Based Particle Physics Detector Cooling Systems," CERN.
[33] V. Bhanot, P. Petagna, A. Cioncolini, and H. Iacovides, *Dynamic Modelling of Two-Phase Cooling Systems Using the Object-Oriented Modelling Platform EcosimPro*. 2018.
[34] H. Qiao and C. Laughman, *COMPARISON OF APPROXIMATE MOMENTUM EQUATIONS IN DYNAMIC MODELS OF VAPOR COMPRESSION SYSTEMS*. 2018, pp. 2043-2050.
[35] H. Qiao and C. Laughman, *Performance Enhancements for Zero-Flow Simulation of Vapor Compression Cycles*. 2023, pp. 128-135.
[36] P. Petagna, B. Verlaat, and A. Francescon, "Two-Phase Thermal Management of Silicon Detectors for High Energy Physics: Macro and Micro Flow Boiling and Numerical Modeling Fundamentals(A 4-Volume Set)," 2018, pp. 335-412.
[37] H. van Gerner and N. Braaksma, *Transient modelling of pumped two-phase cooling systems: Comparison between experiment and simulation*. 2016.
[38] V. Bhanot, P. Petagna, A. Cioncolini, and H. Iacovides, *Simulation and Validation of a CO2-Based Pumped Loop Cooling System*. 2019.

[39] V. Bhanot, P. Petagna, A. Cioncolini, and H. Iacovides, "Development and validation of a simulation tool for next generation detector cooling systems," *Nuclear Instruments and Methods in Physics Research Section A: Accelerators, Spectrometers, Detectors and Associated Equipment,* vol. 955, p. 163264, 2020/03/01/ 2020, doi: https://doi.org/10.1016/j.nima.2019.163264.

[40] B. Bradu, E. B. Vinuela, and P. Gayet, "Example of cryogenic process simulation using EcosimPro: LHC beam screen cooling circuits," *Cryogenics,* vol. 53, pp. 45-50, 2013/01/01/ 2013, doi: https://doi.org/10.1016/j.cryogenics.2012.04.011.

[41] B. Bradu, "Dynamic simulations of the HL-LHC cryogenic system during beam operation," *Cryogenics,* vol. 113, p. 103214, 2021/01/01/ 2021, doi: https://doi.org/10.1016/j.cryogenics.2020.103214.

[42] B. Bradu, "The CERN Cryogenic Simulation Lab: a great support for the operators' training," in *Cryo-Ops*, Grenoble, 2024.

[43] B. Schofield, E. Blanco Vinuela, W. Booth, and M. O. Peljo, "Waste Heat Recovery for the LHC Coooling Towers: Control System Validation Using Digital Twins," presented at the Proceedings of the 17th International Conference on Accelerator and Large Experimental Physics Control Systems (ICALEPCS'19), New York, NY, USA, 2020/10, 2020, DOI:10.18429/JACoW-ICALEPCS2019-MOPHA131. [Online]. Available: https://jacow.org/icalepcs2019/papers/MOPHA131.pdf.

[44] B. Schofield, M. Peljo, W. Booth, and E. Blanco, "WASTE HEAT RECOVERY FOR THE LHC COOOLING TOWERS: CONTROL SYSTEM VALIDATION USING DIGITAL TWINS," 2020.

[45] A. Merino, A. R., A. L. F., and C. and Prada, "Modeling and simulation of a beet pulp dryer for a training simulator," *Drying Technology,* vol. 35, no. 14, pp. 1765-1780, 2017/10/03 2017, doi: 10.1080/07373937.2016.1275674.

[46] H. Li, K. M. Bin, C. I. Ju, G. Dianzhu, P. Jun, and Z. and Huang, "An intelligent digital twin model for the battery management systems of electric vehicles," *International Journal of Green Energy,* vol. 21, no. 3, pp. 461-475, 2024/02/19 2024, doi: 10.1080/15435075.2023.2199330.

[47] J. M. Kwon *et al.*, "Progress in Digital Twin Development of Virtual Tokamak Platform," *IEEE Transactions on Plasma Science,* vol. 52, no. 9, pp. 3910-3916, 2024, doi: 10.1109/TPS.2024.3390159.

[48] A. Mvimbi *et al.*, "Simulating the startup and backup operation of next-generation CO2 pumped-loop cooling systems," presented at the 16th Gustav Lorentzen Maryland, US, 2024. [Online]. Available: http://dx.doi.org/10.18462/iir.gl2024.1103.

[49] CERN, *Functional Analysis for DEMO Cooling System*, L. Davoine, D. Teixeira, V. Bhanot, Y. Herpin, B. Verlaat, and L. Zwalinski, eds., 2023. [Online]. Available: https://edms.cern.ch/ui/#!master/navigator/document?D:101312241:101312241:subDocs.

[50] L. Zwalinski *et al.*, "Progress Towards the Commissioning and Installation of the 2PACL CO2 Cooling Control Systems for Phase II Upgrade of the ATLAS and CMS Experiments," presented at the The International Conference on Accelerator and Large Experimental Physics Control Systems, 2023, 2023. [Online]. Available: http://dx.doi.org/10.18429/JACoW-ICALEPCS2023-TUPDP104.

[51] A. Reyes-Lúa, C. Zotică, K. Forsman, and S. Skogestad, "Systematic Design of Split Range Controllers," *IFAC-PapersOnLine,* vol. 52, no. 1, pp. 898-903, 2019/01/01/ 2019, doi: https://doi.org/10.1016/j.ifacol.2019.06.176.

[52] "Override and Split-Range Process Control," in *Troubleshooting Process Plant Control*, 2017, pp. 125-130.

[53] E. A. I. S.A., *EcosimPro2019 Version 6.0 Modelling and Simulation Software*, Madrid: Empresario Agrupados Internacional S.A., p. 1373.

[54] B. El Hefni and D. Bouskela, *Modeling and Simulation of Thermal Power Plants with ThermoSysPro: A Theoretical Introduction and a Practical Guide*. 2019.

[55] M. Wetter, W. Zuo, T. S. Nouidui, and X. Pang, "Modelica Buildings library," *Journal of Building Performance Simulation,* vol. 7, no. 4, pp. 253-270, 2014/07/04 2014, doi: https://www.doi.org/10.1080/19401493.2013.765506.
[56] W.-J. Zhang, C.-L. Zhang, and G.-L. Ding, "On three forms of momentum equation in transient modeling of residential refrigeration systems," *International Journal of Refrigeration,* vol. 32, no. 5, pp. 938-944, 2009/08/01/ 2009, doi: https://doi.org/10.1016/j.ijrefrig.2008.11.002.
[57] V. Bhanot, R. Dhumane, P. Petagna, A. Cioncolini, H. Iacovides, and V. Aute, "Development of a Numerical Tool for Dynamic Simulations of Two-Phase Cooling Systems," *International Journal of Simulation Modelling,* 2019, doi: http://dx.doi.org/10.2507/IJSIMM18(2)476.
[58] B. R. Munson, D. F. Young, and T. H. Okiishi, *Fundamentals of fluid mechanics*, 5th ed. Hoboken, NJ: J. Wiley & Sons (in English), 2006.
[59] CERN. Demo Partlist [Online] Available: https://edms.cern.ch/document/2607049/2
[60] L. R. Petzold, "A description of dassl: a differential/algebraic system solver," 1982.
[61] M. Bockholt, W. Tegethoff, N. Lemke, N. C. Strupp, and C. Richter, "Transient Modelling of a Controllable Low Pressure Accumulator in CO2 Refrigeration Cycles," 2008.
[62] M. Wetter, "Wetter, M.: Modelica-based Modeling and Simulation to Support Research and Development in Building Energy and Control Systems. Journal of Building Performance Simulation 2(2), 143-161," *Journal of Building Performance Simulation,* vol. 2, pp. 143-161, 06/01 2009, doi: https://www.doi.org/10.1080/19401490902818259.
[63] M. Vidyasagar, I. Society for, and M. Applied, *Nonlinear systems analysis*, 2nd ed. Philadelphia, Pa.: Society for Industrial and Applied Mathematics (SIAM, 3600 Market Street, Floor 6, Philadelphia, PA 19104), 2002. [Online]. Available: http://epubs.siam.org/ebooks/siam/classics_in_applied_mathematics/cl42.
[64] G. F. Franklin, J. D. Powell, and A. Emami-Naeini, *Feedback Control of Dynamic Systems*. Prentice Hall Press, 2014.
[65] K. Ogata, *Modern Control Engineering*. Prentice-Hall, 1970.
[66] M. Thorade and A. Saadat, "Partial derivatives of thermodynamic state properties for dynamic simulation," *Environmental Earth Sciences,* vol. 70, pp. 3497-3503, 2013.
[67] M. J. Moran, *Fundamentals of engineering thermodynamics*. Sixth edition. Hoboken, N.J. : Wiley, [2008] ©2008, 2008.
[68] K. H. Lundberg and Z. J. Malchano, "Three-dimensional visualization of Nichols, Hall, and robust-performance diagrams," *Proceedings of the 2004 American Control Conference,* vol. 2, pp. 1289-1294 vol.2, 2004.
[69] E. Boje, "Further results on Eitelberg's sampling rate design based on (1 — sT/2)," *International Journal of Control,* vol. 51, no. 5, pp. 1155-1158, 1990/01/01 1990, doi: 10.1080/00207179008934123.
[70] T. Andresen, "A Logarithmic-Amplitude Polar Diagram," *Modeling, Identification and Control,* vol. 22, 04/01 2001, doi: https://www.doi.org/10.4173/mic.2001.2.1.
[71] A. V. Oppenheim and Cram, "Discrete-time signal processing : Alan V. Oppenheim, 3rd edition," 2011.

9.Appendices

A1 Main Plant (3 Head) EcosimPro Model

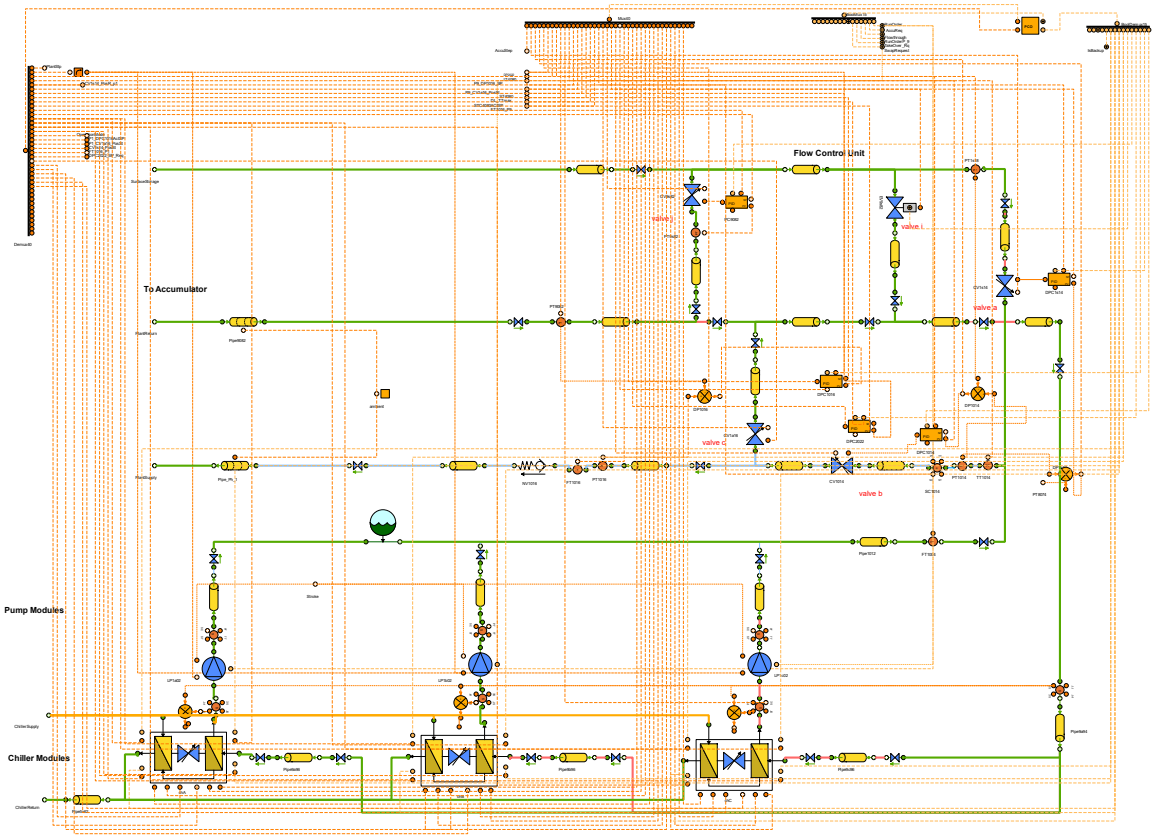

Figure 58: Main Plant [Created in EcosimPro]

A2 Backup Plant (1-Head) EcosimPro Model

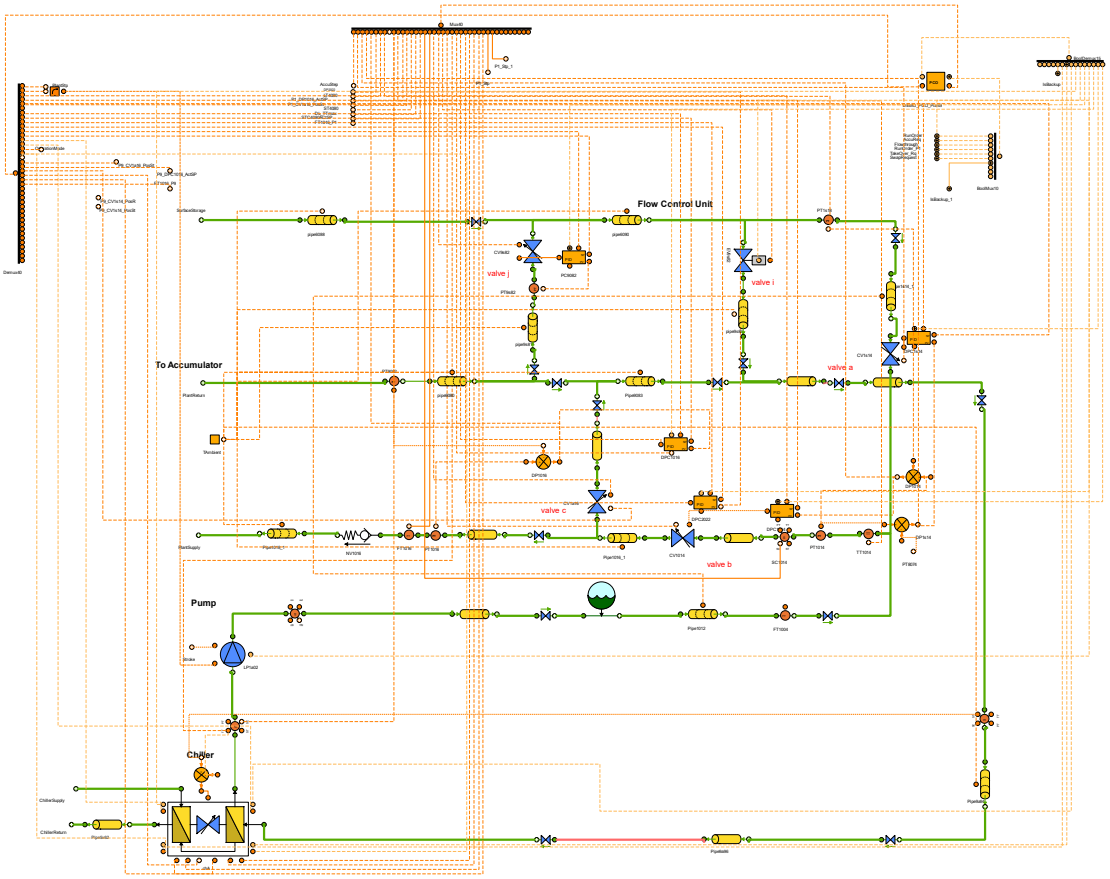

Figure 59: Backup Plant [Created in EcosimPro]

A3 Accumulator EcosimPro Model

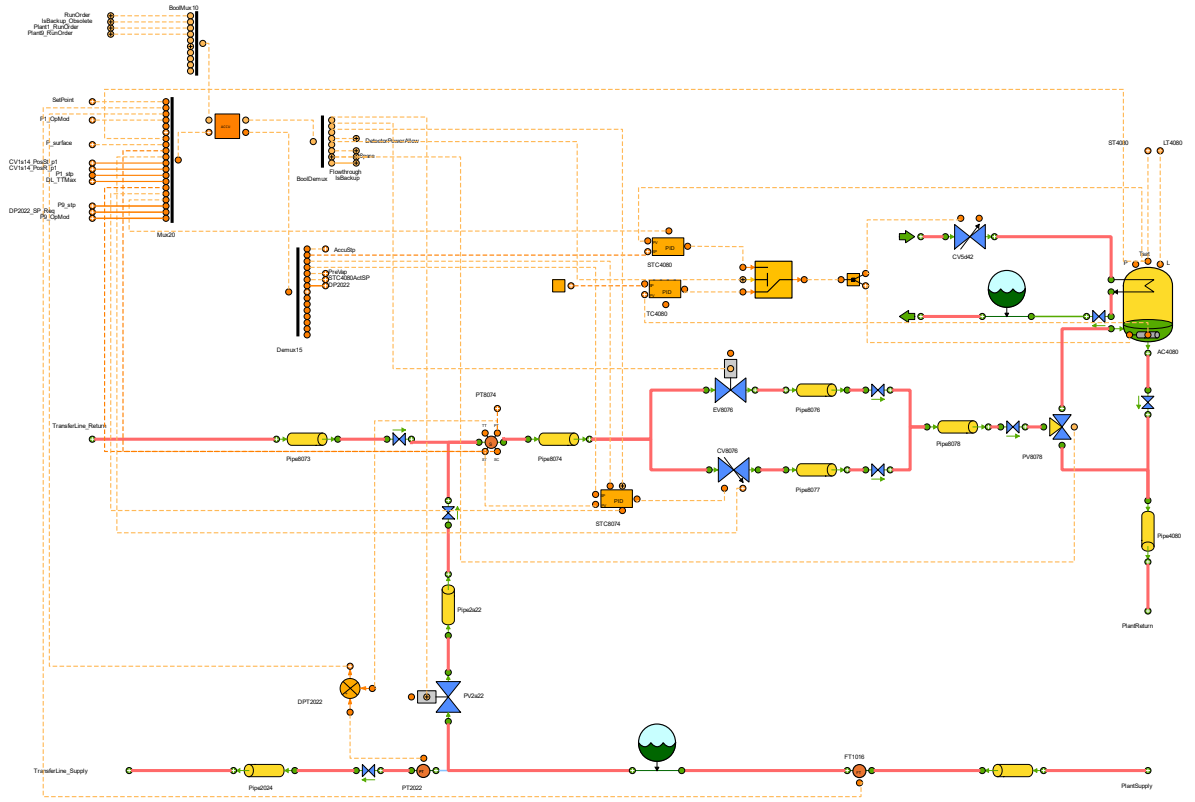

Figure 60: Accumulator [Created in EcosimPro]

B1 Actuator and Field Objects Nomenclature

Table 2: Actuator and Objects Naming Scheme

	Prefix Letters	Description
Actuator and Field Object names	CV	Transfer Line differential Pressure Control Valve
	EV	Electronic On/Off Valve
	PV	Pneumatic Valve
	LT	Level Transmitter
	PT	Pressure Transmitter
	ST	Saturation Temperature Transmitter
	TT	Temperature Transmitter
	LP	Pump
	FT	Flow Transmitter

	HX	Heat Exchanger
	NV	Non-return valve
	STC	Saturation Temperature Controller
	DTC	Differential Temperature Controller
	SHC	Superheat Controller
	DPC	Differential Pressure Controller

B2 Valve List

Table 3: List of Valves

Actuator/Object Schematic Label	P&ID Label	Description
Valve (c)	CV1a16	Transfer Line differential Pressure Control Valve
Valve (g)	CV8076	Back Pressure Regulator Valve
Valve (d)	PV2a22	Pneumatic Bypass Valve
Valve (h)	EV8076	Back Pressure Regulator Bypass Valve
Valve (l)	EV2b20	Pneumatic Valves for flow redirection
Valve (m)	EV8b78	Pneumatic Valves for flow redirection
Valve (b)	CV1014	Discharge Pressure Control Valve
Valve (j)	CV9s82	Accumulator Filling Valve
Valve (a)	CV1s18	Accumulator Emptying Valve
Valve (k)	PV8078	Pneumatic Three-way Valve for flow-through activation
Valve (i)	EV9s82	Pneumatic Valves
Valve (n)	CV2c24	Backup plant load-side pressure drop valve

C1 Startup Root Mean Square Errors (RMSE)

Mass Flow	RMSE (g/s)	Pressures	RMSE (bar)	Temperatures	RMSE (˚C)	Valve Positions	RMSE (%)
Detector Flow	57.5	Main Pump Inlet	0.5	Main Pump Inlet	6.3	dP Control	10.0
		Main Pump Outlet	2.4	Main Pump Outlet	11.3	BPR	5.8
		Detector	1.9	Detector Sat	1.3		
		Accumulator	0.4	Accumulator	0.8		
				Detector	4.3		

C2 Swap Root Mean Square Errors (RMSE)

Mass Flow	RMSE (g/s)	Pressures	RMSE (bar)	Differential Pressures	RMSE (bar)	Valve Positions	RMSE (%)
Main Plant Flow	96.2	Main Pump Inlet	0.6	Main Plant	6.6	Main Plant dP Control	30.5
Backup Plant Flow	150.5	Main Pump Outlet	8.6	Backup Plant	5.4	Backup dP Control	21.9
Detector	89.8	Backup Pump Inlet	24.0	Detector	5.0	Backup Plant dP Control	26.6
		Backup Pump Outlet	6.7			Backup Plant BPR	23.5
		Accumulator	0.4				
		Detector	0.4				

C3 Retakeover Changes Root Mean Square Errors (RMSE)

Mass Flow	RMSE (g/s)	Pressures	RMSE (bar)	Differential Pressures	RMSE (bar)	Valve Positions	RMSE (%)
Main Plant Flow	31.1	Main Pump Inlet	0.3	Main Plant	1.5	Main Plant dP Control	6.0
Backup Plant Flow	31.4	Main Pump Outlet	11.8	Backup Plant	1.4	Backup dP Control	7.0
Detector	0.3	Backup Pump Inlet	0.2	Detector	0.3	Backup Plant dP Control	59.2

		Backup Pump Outlet	0.8			Backup Plant BPR	8.3
		Accumulator	0.3				
		Detector	0.4				

C4 Load Changes Root Mean Square Errors (RMSE)

Mass Flow	**RMSE (g/s)**	**Pressures**	**RMSE (bar)**	**Temperatures**	**RMSE (˚C)**	**Valve Positions**	**RMSE (%)**
Detector	6.7	Main Pump Inlet	0.2	Main Pump Inlet	2.9	Main dP Control	0.8
		Main Pump Outlet	1.7	Detector Saturation	2.1	Accumulator Level	3.8
		Detector	0.5	Accumulator Saturation	0.6		